Complex dynamics of cognitive neural networks within normal and pathological brain states

Peter John Hellyer

2015

This thesis is submitted for the degree of Doctor of Philosophy

"Science, my boy, is made up of mistakes, but they are mistakes which it is useful to make, because they lead little by little to the truth."

-- Jules Verne

Acknowledgments

Looking back, I am left with the feeling that I am yet to substantially or appropriately thank those of whom I owe a debt of gratitude. I fear that committed to paper, the following words will lack the appropriate depth or veracity of my appreciation:

Rob, Richard and David. Thank you for giving me the opportunity to pursue this PhD. You provided me with so many opportunities that I never thought possible. Rob, your patience and support during my continual crises of confidence helped me formulate the ideas and hypotheses that made this work possible. Richard, I cannot express enough thanks for your kind and considered pastoral support, you have always provided a caring sounding board and have looked after me above and beyond the call of duty. Thank you all for your support.

My Family and Friends, without whom I would not. At times, it seemed unlikely that this document would ever see the light of day, but your untiring support has written this PhD ten times over. For your love, support and determination to let me follow my own path: Thank you.

I am indebted to the Medical Research Council and Imperial College London for funding and administrating my PhD. I am also grateful to all participants that took time out to take part in the studies presented here.

Finally, to all the members of the C^3NL, past and present that have put up with me; supported my often complex and indistinct work: Thank you. Your quiet support made this possible. I wish there was a better way to thank you all.

Statement of Publications

Portions of the data presented in results chapters 3 & 5 of this thesis have been previously published in the Annals of Neurology (Hellyer et al. 2013) and Journal of Neuroscience (Hellyer et al. 2014):

Hellyer P J, Leech R, Ham T E, Bonnelle V, Sharp D J. 2013 Individual prediction of white matter injury following traumatic brain injury. Annals of Neurology 73 (4), 489-499

Hellyer P J, Shanahan M, Scott G, Wise R J S, Sharp D J, Leech R. 2014 The Control of Global Brain Dynamics: Opposing Actions of Frontoparietal Control and Default Mode Networks on Attention. The Journal of Neuroscience 34 (2), 451-461

Chapters 4 and 6 are currently under revision at Neuroimage and Journal of Neuroscience respectively.

Copyright Statement

Statement of originality

Functional, structural and neuropsychological data from TBI patients presented in Chapter 3, and 6 were collected as part of a large MRC Funded project (Disconnection after traumatic brain injury: impairments of cognitive control and their impact on learning, PI: David Sharp). Recruitment, scanning and neuropsychological testing of TBI patients was performed jointly by: Prof. David Sharp; Dr. Timothy Ham; Dr. Sagar Jilka; Dr. Kirsi Kinnunen; Dr. Valerie Bonnelle and Susannah James.

Structural connectivity matrices presented in Chapters 4 and 5 were kindly provided by Prof. Patric Hagmann (Hagmann et al. 2008). Portions of the code for Kuramoto oscillator models explored in Chapters 4, 5 and 6 was developed under advice from Prof. Murray Shanahan.

During the course of my PhD I have been lucky to be afforded the opportunity of supervising several talented students on the *MRes Experimental Neuroscience* and *MRes Biomedical Imaging* courses at Imperial College London. Portions of the analysis presented in Chapters 4 and 6 were performed under my supervision by Mr. Frantisek Vasa.

All other work contained in this thesis is my own and conforms to the rules and guidelines set out for PhD theses by Imperial College London, the work of others is appropriately referenced.

Contents

Figure List

Table List

"A scholar's positive contribution is measured by the sum of the original data that he contributes. Hypotheses come and go but data remain"

-- Santiago Ramón y Cajal

Introduction 1

Preface

The classical view in systems neuroscience is that individual regions of the brain are specialised for the execution of specific tasks. This position is supported by a long history of lesion studies and more recently by a wealth of functional neuroimaging research, which has provided insights into how the anatomy of the brain relates to behaviour. However, in recent years this classical view has changed. Instead, new techniques have revealed intrinsic functional connectivity networks (ICNs) that reflect underlying patterns of structural connectivity, now considered to be the fundamental neural architecture supporting cognition and behaviour (Adams, 1982, Smith et al. 2009b, Honey et al. 2009). The activity of these ICNs is dependent on

intrinsic fluctuations in their activity and the behavioural context, which dynamically reconfigure over time (Fox et al. 2005, Ances et al. 2009). Therefore, investigation of brain networks needs to consider not only the structural connections that constrain functional interactions, but also dynamic changes in functional interactions.

An ongoing challenge, therefore, is to define a framework incorporating these neural dynamics that combines insights from structure, function and behaviour. Dynamical systems theory may provide a flexible framework that combines all of these levels. Current theory proposes that healthy neural dynamics operate in a multistable regime that promotes flexible information processing and behaviour (Kelso 2012, Tognoli and Kelso 2014, Shanahan 2012, 2010b, a, Friston 1997, Leech and Sharp 2014, Irner 2007). Large-scale multistable dynamics are likely constrained by underlying structural connections between brain regions. (Honey et al. 2009, Deco, Jirsa, McIntosh, Sporns, and Kötter 2009, Deco, Jirsa, and McIntosh 2011, Deco et al. 2008, Cabral et al. 2011, Cabral et al. 2012). However, it is unclear how such multistable dynamics may relate to behaviour, or how they are constrained by network structure. Moreover, whilst such dynamical accounts place considerable importance on the structural connectivity of the brain, it is unclear how the multistable dynamics are altered when pathological processes result in structural disconnections. In this thesis, I explore such dynamical accounts of the brain using a range of neuroimaging and computational approaches, and examine the implications of this level of description in one example of structural disconnection, namely the consequences of traumatic brain injury.

Networks in the brain

Structural connectivity of the brain

At the microscopic scale, the brain is made up of billions of individual neurons, each with a complex collection of interconnections, the whole forming a network of formidable complexity. The connectivity of these neural networks underlies the emergence of dynamic and coherent physiological activity (Mesulam 1998). Equally, changes to

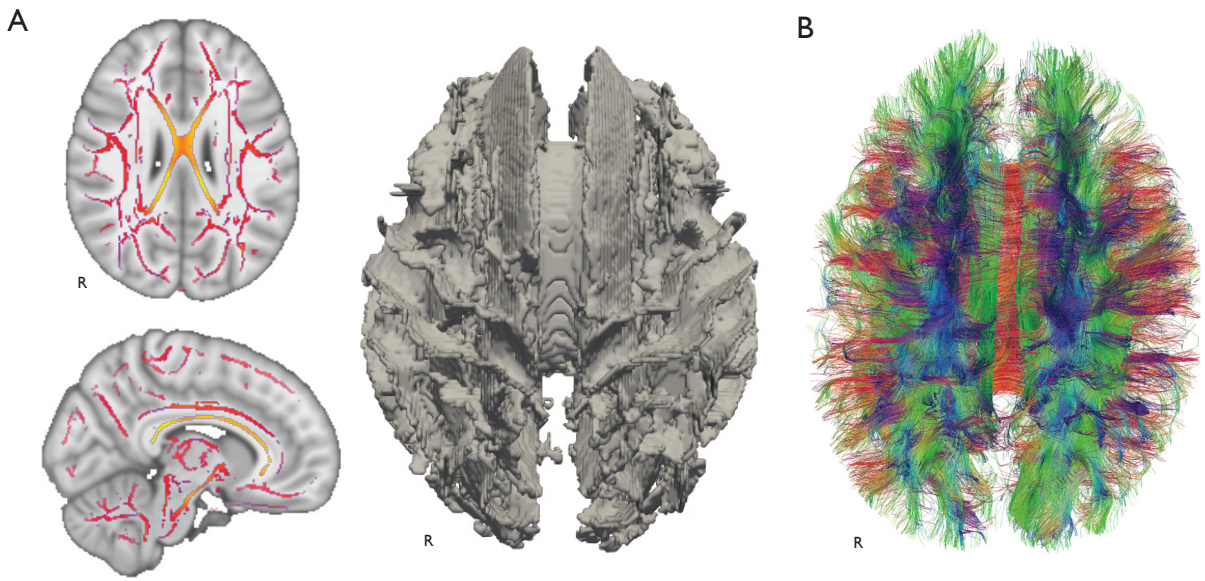

Figure 1.1 | Methods for estimating white matter structural connectivity using the Diffusion Tensor. A) Tract based spatial statistics, estimates white matter integrity at the centre of major white matter tracts, resulting in a 'white matter' skeleton of the brain. B) White matter tractography, attempts to 'reconstruct' white matter fibres within the brain by estimating their trajectory through the brain.

structural connectivity in the brain have been shown to relate strongly to a range of different neurological disorders, such as schizophrenia (Van Den Heuvel, Thornton, and Vink 2007, van den Heuvel and Fornito 2014, van den Heuvel et al. 2010, van den Heuvel et al. 2013, Cocchi, Zalesky, and Fontenelle 2012, Fornito, Zalesky, et al. 2012, Zalesky et al. 2012, Zalesky et al. 2011, Catani and Ffytche 2005) and traumatic brain injury (Sharp, Scott, and Leech 2014, Kinnunen et al. 2011, Bonnelle et al. 2012, Bonnelle et al. 2011, MacDonald et al. 2007).

The analysis of the 'connectome' in relation to behaviour emerges from the idea that behaviour is attributable not only to individual regions but also emerges from interactions between multiple regions, interactions that are necessarily constrained by the topological connectivity of the brain (Sporns 2011, Sporns, Tononi, and Kotter 2005, Bullmore and Sporns 2009, Honey et al. 2009). One recent advance in magnetic resonance imaging (MRI) - Diffusion Tensor Imaging (DTI) - provides the opportunity to examine the macroscopic connectivity in the human brain in vivo by assessing the diffusion of water along white matter tracts [Figure 1.1]. There have been two main

uses of DTI. The first has been to examine measures of white matter integrity in cross-section at each voxel within a representative white matter 'skeleton' applied to each subject (Smith et al. 2006) [Figure 1.1A]. A measure such as fractional anisotropy (FA) is considered to be good marker of structural integrity, where high FA is believed to indicate intact tissue structure, consistent with organized bundles of axons within the white matter, whereas low FA is suggestive of microstructural damage indicative of axonal injury (Rugg-Gunn et al. 2001, Arfanakis et al. 2002). The alternative approach has been to use tractography for the estimation of the trajectory and strength of white matter fiber pathways between predefined structural regions of interest [Figure 1.1B]. This approach can be built up to provide a graph of connections between brain regions, that can be understood using graph theoretic measures (Rubinov and Sporns 2010, Bassett and Bullmore 2006, Bullmore and Sporns 2009, Zalesky et al. 2012).

Graph theoretical approaches to measuring structural connectivity

According to graph theory, the strength of connectivity in the whole brain can be described by a graph composed of nodes (vertices) representing particular brain regions of interest [Figure 1.2], linked by edges representing the physical connections between these regions. Measures of connectivity within the 'graph' of the brain can then be expressed formally, using a range of mathematical descriptions such as community structure, local node connectivity or interconnections between different regions (Rubinov and Sporns 2010, Sporns 2003, Sporns 2006, Sporns and Kotter 2004) .

One important property of structural networks in the healthy human brain is the idea of 'small-worldness' – a topology maximising clustering within groups of nodes, with sparse inter-connectivity between clusters. Small world architectures appear to be ubiquitous in a range of structural brain networks (Sporns and Zwi 2004, Bassett and Bullmore 2006, Achard et al. 2006, Bassett et al. 2009, Humphries and Gurney 2008,

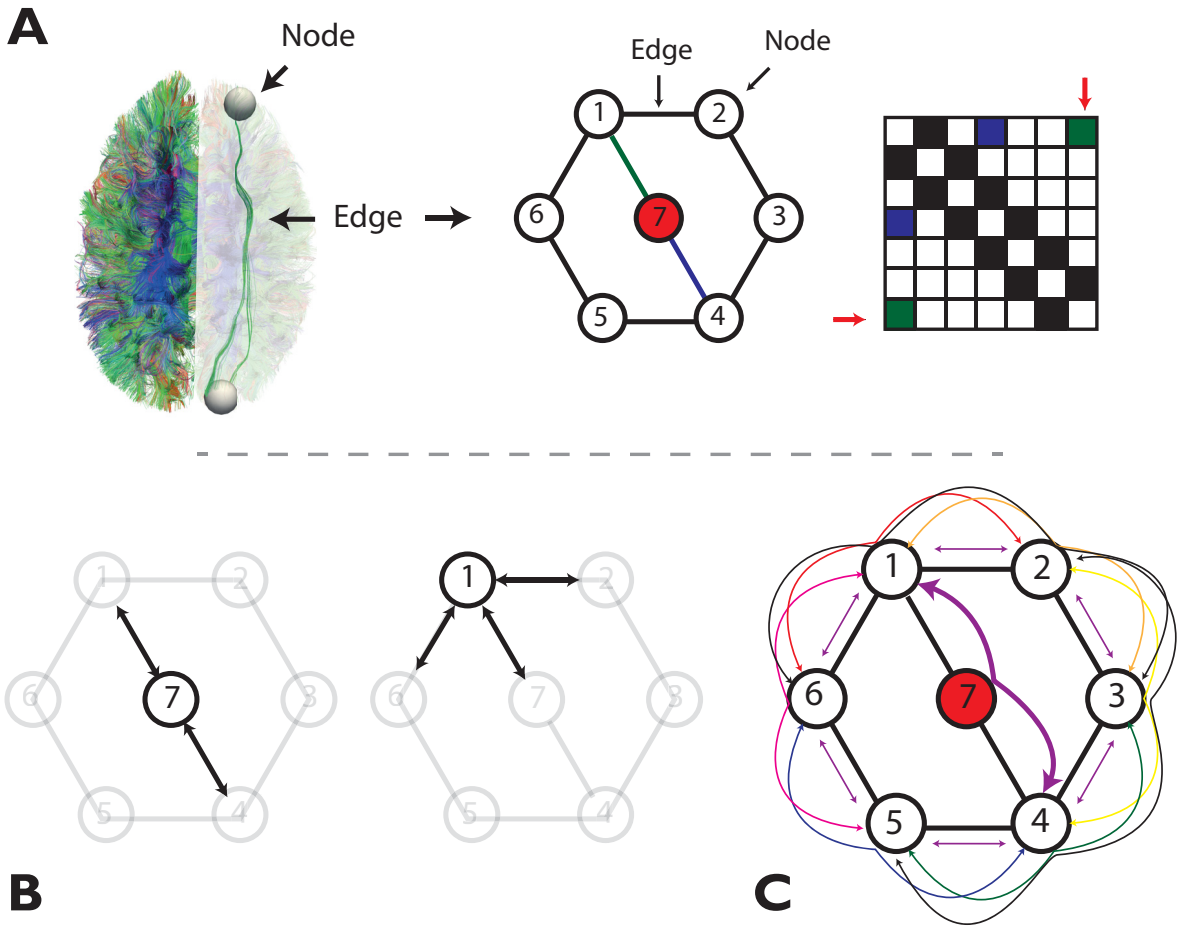

Figure 1.2 | Graph theoretical representations of structural brain networks. A Left) Structural connectivity of the brain can be represented as a graph, where the 'nodes' of the graph represent regions of the brain or functional ROIS. The weight of each 'Edge' can be estimated as the strength of empirical connectivity between a pair of nodes. A Right) an example network, of 7 nodes, represented as both a topological diagram, and a weighted graph. B) The degree of individual nodes within the network can be estimated by counting the number of connections made between it and each other node within the network. Node 7 for example has a degree of 2 whereas node 1 has a degree of 3. C) Another commonly used graph metric is 'Betweenness centrality' defined as the proportion of shortest paths between all other nodes within the network which pass through an individual node. In the example here, node 7 has a low betweenness centrality (1/15), as only one of the shortest paths between all other nodes within the network pass through node 7. The addition of extra connections between node 7 and other nodes within the network would increase the centrality of this node.

Sporns 2006, Watts and Strogatz 1998). Such a network configuration is thought to be economical, minimising wiring costs whilst supporting the emergence of local interconnected hubs. Such network configurations should allow high dynamic flexibility (Bullmore and Sporns 2009). In practice, this means that information may pass to any part of the network through a very small number of steps whilst still allowing complex functional interactions between diverse regions of the brain. Related to the existence of a small world architecture is the notion that the overall distribution of edge weights within the network has a heavy tail; that is, the network will contain a few densely distributed hub regions (Gong et al. 2009, Hagmann et al. 2008, van den Heuvel et al. 2012, van den Heuvel and Sporns 2013, 2011). These densely interconnected regions form a 'rich club' (van den Heuvel and Sporns 2011). The aggregation of hubs into a rich club suggests that highly connected brain regions do not operate as individual entities, but instead act as strongly interlinked collectives.

Intrinsic connectivity networks

One of the first approaches to examining functional activity in the brain was to correlate voxel-wise BOLD activity with a psychological regressor– identifying regions of the brain that were associated with the performance of a task. Whilst this has been a powerful framework for examining the activity of the brain, spontaneous fluctuations in BOLD activity are visible even in the absence of task, and across a wide range of different brain states (Smith et al. 2009} [Figure 1.3]. Initially using seed-based approaches, where activity in a discrete region of the brain is correlated with activity in every other voxel of the brain (Fox et al. 2005), it has become clear that these spontaneous fluctuations of activity are arranged in long range patterns of activity across the cortex. These are termed ICNs, and they can be readily resolved from resting state fMRI; that is, when data are acquired while the subjects are 'at rest' in the scanner, and are not exposed to any stimuli nor engaged in any explicit task. ICNs have proved to be highly conserved across subjects (Friston et al. 1993, Smith et al. 2009b, Fox and Raichle 2007, Fox et al. 2005, Raichle et al. 2001, Beckmann

et al. 2009, Beckmann et al. 2005). More recently, approaches such as independent component analysis (ICA) have revealed a range of relatively stable and robust ICNs evident in resting state data [Figure 1.4]. Functional networks often reflect underlying structural connectivity (Honey et al. 2009, Hagmann et al. 2008, Smith et al. 2009a), and the exact nature and functional properties of the ICNs is directly related to the complexity of structural connectivity in the brain. In particular, that small world and strong rich club structural configurations, lead to highly diverse range of functional ICN configurations (Senden et al. 2014, Senden, Goebel, and Deco 2012).

Measures of functional activity, such as pairwise correlation and ICA, assume, as a first approximation, that relationships between nodes are consistent across space or time. However, unlike structural connectivity, which at least over a short timescale is static, functional connectivity patterns are diverse and reconfigure dynamically over

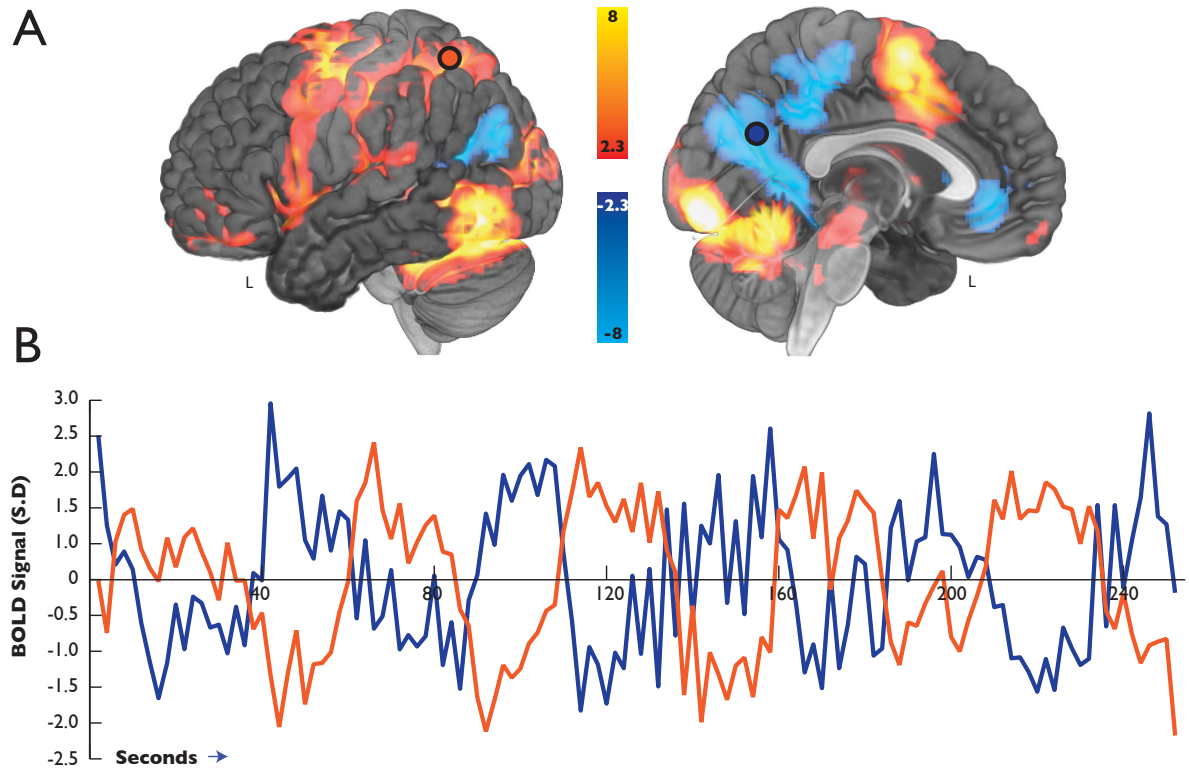

Figure 1.3 | Anti-correlated activity of task positive and default mode networks. A) Activation of task positive regions of the brain (RED) during blocks of the choice reaction time task (CRT). Task invoked activity is anticorrelated with activity within the default mode network (Blue), (n=20) B) activation time-courses extracted from a single subject from the precuneus (blue) and superior parietal lobe (orange), demonstrating clear anti-correlation between these two regions. Figure inspired by (Fox et al, 2005).

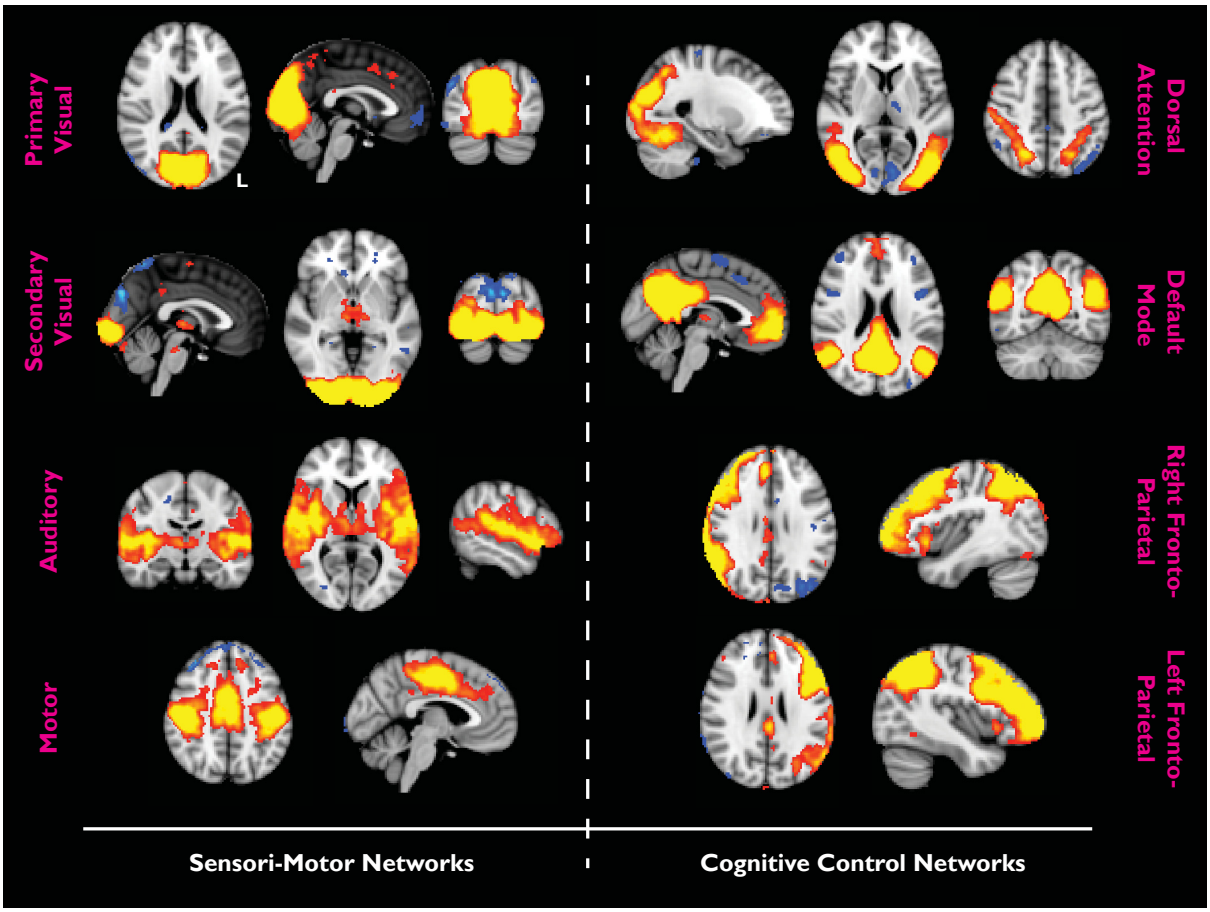

Figure 1.4 | Intrinsic functional connectivity networks (ICNS) in the brain.

Shown here are 8 of the most common intrinsic connectivity networks of the brain, defined using independent component analysis of resting state fMRI (Smith et al, 2009)

time, even when subjects are 'at rest' (Chang and Glover 2010, Zalesky et al. 2014, Hutchison, Womelsdorf, Allen, et al. 2013, Hutchison, Womelsdorf, Gati, et al. 2013, Allen et al. 2014, Handwerker et al. 2012, Monti et al. 2014). This is because functional interactions are the result not only of the structural connectivity of the brain, but also the interactions between recent connectivity and local dynamics. They are also altered by the behavioural context (Smith et al. 2009a); for example, attention to external stimuli increases activity in fronto-parietal control networks (Corbetta and Shulman 2002, Vincent et al. 2008, Spreng and Grady 2010, Spreng et al. 2010, Fornito, Harrison, et al. 2012), whilst at the same time activity within the so-called default mode network, which is most active during internally directed cognition, decreases [Figure 1.3]. This anti-correlated activity has now been observed in a number of studies (Singh

and Fawcett 2008, Fox et al. 2005, Smith et al. 2009a, Raichle et al. 2001, Buckner, Andrews-Hanna, and Schacter 2008, Seeley et al. 2007) .

More broadly, activity within a wide range of partially overlapping functional ICNs have been associated with a range of different cognitive tasks (Smith et al. 2009a). Moreover, resting state functional connectivity is disrupted in a range of different neurological and psychiatric disorders, such as autism (Deco, Jirsa, McIntosh, Sporns, and Kotter 2009, Kennedy and Courchesne 2008, Ing et al. 2010, Edison et al. 2008), schizophrenia (Liang et al. 2006, Bluhm et al. 2007, Zhou, Liang, Jiang, et al. 2007, Zhou, Liang, Tian, et al. 2007, Whitfield-Gabrieli et al. 2009), Alzheimer's disease (Greicius et al. 2009, Greicius et al. 2004, Sheline and Raichle 2013); and traumatic brain injury (TBI) (Sharp et al. 2011b, Sharp et al. 2010, Bonnelle et al. 2012, Bonnelle et al. 2011, Jilka et al. 2014, Ham et al. 2013). Therefore, demonstrating network disruption is a potential biomarker for a wide range of different brain disease states.

Network dysfunction following Traumatic Brain Injury

Traumatic Brain Injury (TBI) which has a characteristic behavioural phenotype, causality of changes to both cognition and functional connectivity can be inferred by measuring structural disconnection of the brain as the result of the trauma, using advanced MRI approaches such as DTI. Nevertheless, patterns of functional network disruption may be complex and counterintuitive. Thus, for example, functional connectivity in the default mode network increases as a result of structural disconnection following TBI (Sharp et al. 2011a).

TBI is one of the leading causes of death and disability in the under 40s (Bruns and Hauser 2003), with a corresponding socio-economic burden. TBI is apparent from a clinically evident alteration in brain function, such as coma or post-traumatic amnesia, and from radiological evidence of brain pathology, such as the presence of a haematoma visible on X-ray, CT scan or MRI, which may result from either a penetrating or non-penetrating injury (Menon et al. 2010). The generally accepted diagnostic criteria for the presence of TBI following trauma, even in the absence of a clear history of the incident, is typical changes on diagnostic images and/or characteristic neurological and neuropsychological signs (Carroll et al. 2004). A commonly used objective scale for the classification of the severity of TBI is the MAYO scale (Malec et al. 2007), which has three categories: (a) Moderate-Severe (definite brain injury); (b) Mild (probable brain injury), and (c) Symptomatic (possible brain injury) [Table 1.1].

Pathophysiology & Mechanisms

The pathological consequences of TBI is variable, and ranges from focal damage (contusion or frank haematoma) to widespread damage to the white matter, the latter is often not apparent on routine diagnostic imaging (Graham et al. 2000, Gentleman et al. 1995). The mechanisms of damage can be separated into two different phases:

Classification	Criteria (one or more apply)
Moderate – Severe (Definite TBI)	1. Death 2. LOC > 30 mins 3. PTA > 24 hrs 4. Worst GCS (0-24hrs post injury) < 13 5. Radiological evidence of: a. Intracerebral hematoma b. Subdural hematoma c. Cerebral contusion d. Hemorrhagic contusion e. Penetration of the dura f. Subarachnoid hemorrhage g. Brain Stem damage
Mild (Probable TBI)	1. LOC < 30 mins 2. PTA < 24 hrs 3. Skull fracture with intact dura
Symptomatic (Possible TBI)	1. Blurred vision 2. Mental state changes 3. Dazed 4. Dizziness 5. Focal neurological symptoms 6. Headache 7. Nausea

Table 1.1 | Mayo Classification of TBI. Post traumatic anterograde amnesia (PTA), Loss of Consciousness (LOC), Glasgow Coma Scale (GCS), Traumatic Brain Injury (TBI). Reproduced from (Malec et al. 2007).

primary (as a direct result of trauma) and secondary (long term reactive changes in the brain). Primary mechanisms of damage during TBI are typically caused by accelerative and compressive forces imparted to the brain through the skull, which even in a non-penetrating injury causes the brain to impact the inside of the skull, resulting in a characteristic contra-coup injury remote from the site of impact. Contra-coup injuries are most commonly observed in orbitofrontal, anterior temporal and occipital regions [Figure 1.5].

Rotational forces may also result in considerable damage. The brainstem, together with the cerebellum, are tethered firmly, but the cerebral hemispheres may rotate as the head rocks back and forth after the impact. These rotational movements of the cerebral hemispheres result in shearing injuries to the white matter, particularly around the midline, causing diffuse injury within white matter pathways crossing the corpus callosum and in ascending and descending pathways to the brainstem. In

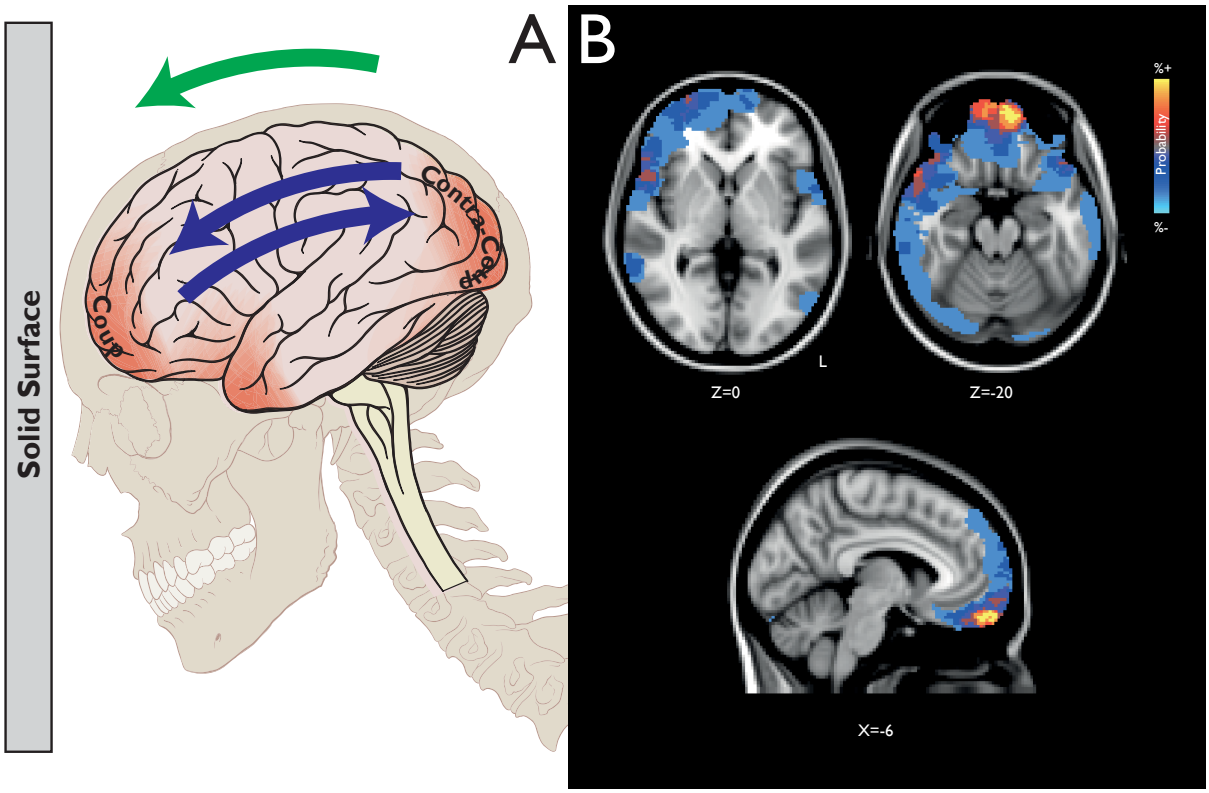

Figure 1.5 | Coup-Contracoup damage to the brain during blunt head trauma. A) Mechanism of damage during blunt head trauma to the frontal lobes, causing the brain to rock forwards and backwards inside the skull, leading to well defined patterns of damage (Image adapted from an image by P. J. Lynch, Yale - Creative Commons). A lesion overlay map for a group of 32 TBI patients (as presented in chapter 6) demonstrating a clear contra-coup pattern of cortical damage.

extreme cases there may be axonal shearing, evident on specific diagnostic MRI sequences that reveal microhaemorrhages as the result of microvascular disruption; a marker of the shearing forces to which the white matter tracts had been subjected [Figure 1.6]. Shearing forces to the corpus callosum are particularly pronounced when the rapid acceleration and deceleration imparted to the head cause the left and right hemispheres to move in opposite directions to one another (Adams et al. 1989). Delayed secondary complications following TBI include ischaemia, brain swelling (oedema) increasing intracranial pressure (Sharp, Scott, and Leech 2014), infection (common after penetrating injuries), and delayed neurodegeneration. Recent work also suggests that chronic inflammatory processes within the brain are pronounced even many years following the initial injury (Ramlackhansingh et al. 2011). Whether chronic inflammation contributes to delayed neurodegeneration is uncertain, but it may be a contributory factor.

Long-term cognitive consequences

The cognitive consequences of TBI are often long-term and disabling. Estimates of the prevalence of neuropsychiatric disorder and cognitive impairment suggest that ~50% of TBI patients demonstrate clinically relevant psychiatric disorders, most commonly anxiety, depression and aggression, whilst ~70% of patients have some degree of cognitive impairment (Vaishnavi, Rao, and Fann 2009). Cognitive deficits following TBI predominantly affect the domains of information processing speed, attention and executive function (Draper and Ponsford 2008, Levin 1995, Scheid et al. 2006). Efficient functioning of these cognitive domains is dependent on the coherent activity of widespread networks within the brain (Mesulam 1998), and are therefore vulnerable to structural network disconnections following TBI.

The deficits in sustained attention, memory and information processing speed are apparent clinically as increased distractibility and poor concentration (Kinnunen et al. 2011, Ponsford and Kinsella 1992, Levin and Kraus 1994, Levin 1995, Scheid et al. 2006, Draper and Ponsford 2008). On measures of sustained attention using the Sustained Attention to Response Task (SART), which involves withholding a key press to an infrequent no-go target embedded within a sequence of numbers, TBI patients make a greater number of errors, indicating a deficit in sustained attention (Dockree et al. 2004, Sharp et al. 2011a, Bonnelle et al. 2011, Bonnelle et al. 2012). Additionally, patients have problems with the other aspects of attention,such as dividing attention across multiple different tasks at the same time (Niemann, Ruff, and Kramer 1996); for example, when performing the relatively simple tasks of random number generation and the SART concurrently, patients consistently perform worse than healthy controls and report significantly increased mental effort (Azouvi et al. 2004, Jilka et al. 2014). This is more pronounced when the tasks requires controlled processing, with volitional allocation of resources, as opposed to when the tasks are carried out automatically

(Park, Moscovitch, and Robertson 1999, O'Keeffe F et al. 2007, Godefroy 2003).

Response speed is often thought to be an index of cognitive efficiency, being dependent on rapid reorganisation of cognitive resources to perform the task currently at hand. It can be measured using the time to initiate a response following presentation of a simple visual cue: the Choice Reaction Time task (CRT) (Brefel-Courbon et al. 2007). Reduced information processing speed is common following TBI (Mathias, Beall, and Bigler 2004, Mathias et al. 2004, Comerford et al. 2002), indicating reduced information processing efficiency. Additionally, many patients experience a variable degree of post-traumatic amnesia (Sharp, Scott, and Leech 2014). The memory impairments may be be short-lived, but in some patients they may extend for many years following the injury (Draper and Ponsford 2008, Mathias, Beall, and Bigler 2004).

Structural network dysfunction following TBI

The presence of contusions or haematomata is a poor indicator of prognosis following TBI, suggesting that cognitive change following TBI is less related to focal lesions. One possibility is that widespread damage to structural networks as the result of diffuse axonal injury is more important to understanding outcome. Assessing the extent of such network damage is an important clinical challenge, made difficult because diffuse damage to the microstructure of white matter is not apparent using conventional X-ray CT scanning or routine MRI sequences. The disruption of the microvasculature of the brain which leaves tell-tale small haemosiderin deposits termed 'microbleeds' (MBs), are visible using T2-weighted sequences, and these are associated with cognitive impairment (Scheid et al. 2003) [Figure 1.6]. However, it is clear that the presence of MB in the white matter offers only a 'tip of the iceberg' view of the microstructural damage to the white matter, with post-mortem studies indicating that diffuse post-traumatic axonal injury (TAI) may be widespread even when there are only a few or no

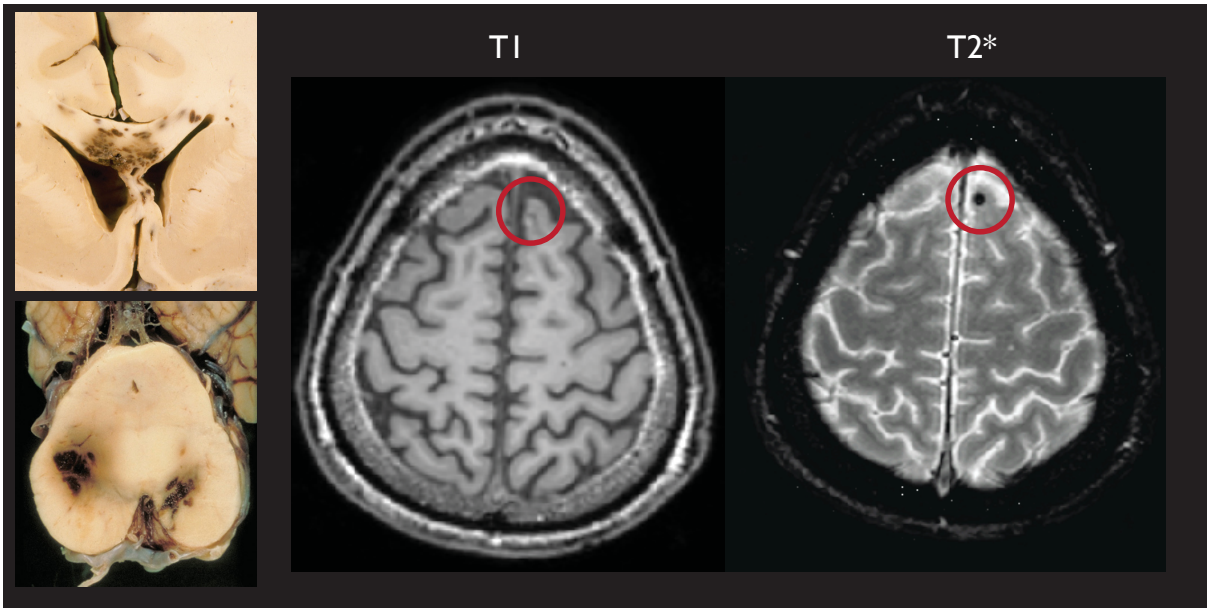

Figure 1.6 | White matter microbleeds following TBI. Histopathological sections of the brain following TBI, demonstrating widespread disruption of the vasculature within the white matter (Left Top, a corpus callosal section, Left Bottom, within the brainstem). These microbleeds are not visible on standard T1-weighted images, but appear as regions of signal dropout in susceptibility weighted T2* images (Right, T1 and T2* images from an exemplar patient with mild TBI). Histopathological images in Left panels © P. Agamanolis, Northeast Ohio Medical University, OH, USA

MBs evident on imaging (Gentleman et al. 1995).

In contrast to more standard MR imaging approaches, DTI measures have demonstrated widespread white matter disruption irrespective of the presence or absence of MBs. TBI causes a characteristic pattern of white matter damage, predominately affecting long distance white matter interhemispheric connections (Kinnunen et al. 2011, Smits et al. 2011, Sharp and Ham 2011). Using both post-mortem and DTI measures in animal models of TBI indicate that specific diffusion measures of white matter damage, namely radial and axial diffusivity, can distinguish between microstructural changes such as axonal and myelin sheath abnormalities (Song et al. 2003, Song et al. 2002, Sun et al. 2012, Beaulieu 2002, Assaf and Pasternak 2008). Further, the radial and axial diffusivity measures continue to change over time following the injury (MacDonald et al. 2007, Sharp and Ham 2011). DTI measures have also been shown to predict cognitive impairment, such as reduced information processing speed, working memory, task switching and performance on motor response tasks (Kinnunen et al.

2011, Jilka et al. 2014, Bonnelle et al. 2012, Sharp and Ham 2011, Ham et al. 2013).

In recent years, graph theoretical approaches have begun to be used to examine the effect of TBI on structural network dysfunction (Caeyenberghs et al. 2014). These approaches have demonstrated that although the structural networks in TBI patients retain broad similarities with undamaged networks, such as small world topology, there are longer average path lengths between nodes and hence decreased global efficiency. This finding indicates a pathological topology that results in weaker integration of neural information, particularly across remote brain regions.

These recent studies have shown that DTI is a sensitive way of quantifying white matter abnormality following TBI, and how specific patterns of damage relate to cognitive decline (Kinnunen et al. 2011, Smits et al. 2011, Messe et al. 2011) . However, it is not clear how best to apply this technique to individual patients - either to diagnose the presence of axonal injury following a TBI, or predict likely long term functional ouctome. Machine learning is increasingly used to assist complex diagnostic decisions, by integrating multiple pieces of information in the diagnostic process. By this method, a 'classifier' is trained on data that have been diagnostically labelled, and this is then applied to undiagnosed data. In this way, the generalisation of a classifier to novel patient data can be assessed and an individual prediction made (Sajda 2006). Using structural network measurements (from DTI) combined with a machine classifier is a potentially useful approach to provide individual, rather than group, diagnostic information, and so has the potential to bridge between basic research and clinical application.

Functional network dysfunction and its relationship to structural disconnection

Functional connectivity assessed with fMRI demonstrates significant abnormalities following TBI, including a mixture of both hypo- and hyper-connectivity. For example,

DMN connectivity may be reduced acutely following injury (Hillary et al. 2011), but is increased in the chronic phase (Sharp et al. 2011a). Changes to network functional connectivity following TBI also include increased connectivity between the DMN and the left prefrontal cortex (LPFC) (Mayer et al. 2011), decreased connectivity between motor cortex and the striatum, and increased connectivity within fronto-parietal cognitive control networks (Shumskaya et al. 2012). The specific example of blast injury resulting in head trauma leads to reduced inter-hemispheric synchrony within the frontal lobes (Sponheim et al. 2011).

Interestingly, structural disconnection in the brain following TBI – in particular, between the right anterior insula and dorsal anterior cingulate cortex (often referred to as the salience network or SN), is closely linked to alterations in the DMN. In healthy control subjects, the DMN is strongly deactivated during sustained attention tasks, whilst the SN is active during sustained attention tasks such as the Stop Signal Task. During response inhibition, functional connectivity between nodes within the SN and the DMN transiently increases, demonstrating that the SN responds to salient external stimuli. These interactions break down in patients following TBI. In those who perform poorly on the SST, the DMN does not deactivate normally when SN activity increases (Bonnelle et al. 2012), with altered functional connectivity at the time of response inhibition (Jilka et al. 2014). The level of this dysfunction is directly predicted by reduced structural disconnection between the cortical components of the SN (Bonnelle et al. 2012, Jilka et al. 2014). These functional imaging measures also predict the rapidity and accuracy of task switching in response to a cue (Jilka et al. 2014). Taken together, these results are consistent with a model of cognitive control in which efficient and rapid information flow between networks is important for effective cognitive function, and is dependent on the structural integrity of certain key white matter tracts

An integrated approach: using dynamics to link between structure, function and behaviour

Although, links between structural disconnection, altered functional connectivity and behavioural impairment have been found in many studies, the relationships between the three domains are generally descriptive, and no satisfactory mechanisms which link across thes three interconneted levels of description have been proposed. The challenge is to understand how network dynamics, and in particular how spontaneous neural dynamics, expressed in terms of functional network activity constrained by complex structural connectivity, relates to behaviour (Sharp, Scott, and Leech 2014). One approach is to consider the brain as a complex dynamical system (Shanahan 2012, Chialvo 2010, Beggs and Plenz 2003, Beggs 2008, Kitzbichler et al. 2009), supported by theoretical evidence provided by computational approaches to neuroscience. Computational models provide detailed descriptions of how local activity can interact with macroscopic patterns of structural connectivity to generate dynamic changes in activity within networks over time (Deco, Jirsa, McIntosh, Sporns, and Kotter 2009, Deco, Jirsa, and McIntosh 2011, Deco et al. 2008, Cabral et al. 2011, Cabral et al. 2012). These models have been increasingly used to try to understand intrinsic connectivity networks, and in particular the relationship between functional and structural connectivity in brain networks. Multiple studies have based models on the graph of structural connectivity, defined by tractography, to specify the strength and time delay of coupling between nodes that represent individual regions of the cortex or subcortical nuclei. Such models are able to reproduce patterns of functional connectivity with an impressive degree of accuracy, and have been used to examine the effect of delay, topology, noise and the emergence of slow temporal interactions as the result of coupling fast local neural dynamics (Honey et al. 2009, Deco, Jirsa, and McIntosh 2011, Deco et al. 2008, Deco, Jirsa, and McIntosh 2013, Cabral et al. 2011, Cabral et al. 2012, Deco et al. 2014, Deco et al. 2013, Deco, Senden, and Jirsa 2012). Increasingly, these computational approaches have been applied to neurological and

psychiatric disorders to model the effect of cortical disconnection on resting state functional activity (Cabral et al. 2013, Cabral et al. 2012).

In this thesis, I explore how neural dynamics provides a framework to potentially link across the three domains of strucutre, function and behaviour. In particular, metastable neural dynamics have considerable potential for providing both a conceptual and computational framework to mechanistically link structure to behaviour. Metastability, which is here defined as the tendency of a dynamic system to move endogenously between transient attractor-like states, is an important property of such systems (Friston 1997, Tsuda 2001, Kelso 2012, Shanahan 2010b), and "reconciles the well-known tendencies of specialized brain regions to express their autonomy (segregation) and the tendencies for those regions to work together in synergy (integration)" (Tognoli and Kelso 2014). Theoretical studies suggest that the neural dynamics of the healthy brain operate in a multistable regime, in which neural ensembles are able to coordinate rapidly, flexibly engaging and disengaging without becoming locked in fixed relations (Bressler and Kelso 2001, Kelso 2012, Tognoli and Kelso 2014, Shanahan 2010b). Metastability, is very tightly linked with the concept of 'Multistability'. Where metastability descibes, the tendancy of an isolated complex system to engage over time in transient ' medium-high energy saddle states' which restrict the thermodynamic tendancy for the system to reach the most stable low-energy state within a finite energy landscape; Multistability, refers to a similar affinity of a complex system to transit spontaneously between multiple saddle states, of differing energy levels within an indefinate energy landscape. To avoid confusion and for precision of the measures defined later, I refer predominantly to 'multi' rather than 'meta' stability for measures in this context. According to one hypothesis, increased multistability in the brain allows more flexible dynamic interactions between regions, whereas reductions in multistability may accompany persistent, more stable states (Shanahan 2010a). The level of multistability in a system also likely depends on the network topology. Equally, multistable functional dynamics have a strong intuitive link

to cognitive processes such as flexibility, exploration and integration of information, and is useful for explaining certain high-level cognitive skills. Such an approach would likely provide a strong theoretical framework for the development of clinically relivant biomarkers for cognitive dysfunction.

Thesis overview

The core aims of this thesis are to use insights from dynamical systems theory to explore the effect of: a) cognitive state; and b) structural disconnection on complex measures of neural dynamics, such as multistability and synchrony. DAI following TBI was used to explore the relationship between acquired structural disconnection, multistable neural dynamics and behaviour. The thesis is devided into the following sections:

Methods for Structural and Functional Magnetic Resonance Imaging

In chapter 2 I describe important general concepts in the use of MRI to study both the function and structure of the brain, in terms of their relevance of the results presented in subsequent chapters.

Individual Prediction of White Matter Injury and Cognitive Outcome following Traumatic Brain Injury

In chapter 3 I describe the use of a range of approaches to demonstrate that structural disconnection, measured using both standard diffusion techniques and graph theoretical approaches, differentiate TBI patients from healthy controls, whilst also providing a predictive framework for cognitive dysfunction following TBI. Thereby, I demonstrate the importance of structural disconnection when attempting to understand the behavioural consequences TBI.

A computational model of the neural dynamics in the resting brain

In chapter 4 I introduce and validate, using several different measures of resting state functional connectivity, a computational model based on the macroscopic white

matter structural connectivity of the brain, to explore how white matter structure relates to neural dynamics, including multistability, in the 'resting' brain.

The Control of Global Brain Dynamics: Opposing Actions of Fronto-Parietal Control and Default Mode Networks on Attention

In chapter 5 I expand the dynamical systems model demonstated in the previous chapter by using the computational models combined with empirical fMRI data to explore the relationship between brain network dynamics, including multistability and cognitive state. Specifically, I investigate how state dependent measures of global multistability may be tuned by the interaction of higher order cognitive control networks.

The Human Connectome Confers Cognitive Flexibility through Metastable Neural Dynamics

In chapter 6 I further explore the dynamical systems account described in the previous chapters to explore the extent to which changes to network structure, can bring about cognative dysfunction through alterations in multistability. Speciically, I combine the results from TBI patients presented in earlier chapters and relate multistability to altered cognitive function and structural connectivity following TBI, thus forming a framework by which measrues of functional dynamics, relate to both cognition and strucure.

Methods for structural and functional Magnetic Resonance Imaging

2

Principles of Magnetic Resonance Imaging

MRI is an imaging technique that produces images of biological tissue by exploiting the properties of hydrogen protons abundant within biological tissue, when placed inside a strong magnetic field.

Magnetization

At rest, the rotation of hydrogen protons around their axis induces a small polar magnetic charge known as the magnetic moment. In biological tissues, the magnetic moment of each proton is not usually aligned along any particular axis and thus the 'net moment' (represented in 3 dimensions in Figure 2.1A) is very small. When the

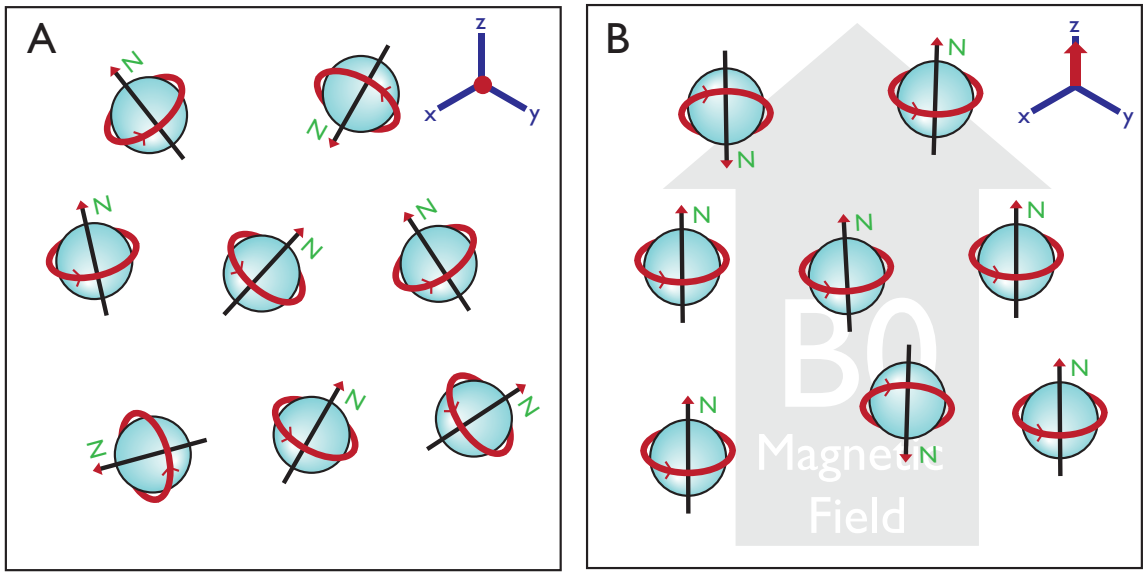

Figure 2.1 | Magnetisation of Hydrogen ions in the presence of the B0 field A) In the absence of a strong magnetic field, the orientation of free hydrogen ions, is randomly distributed. B) The application of a strong magnetic field (B0) such as in the MRI scanner causes hydrogen ions to align with the field, providing a net vector of magnetisation along the axis of the applied magnetic field. The net moment of the overall field of protons is displayed in three dimensions in the top right.

tissue is subject to a large magnetic field, such as when the body is placed into the bore of the MRI machine (B0 Magnetic field), the magnetic moments of each proton align along the axis of the magnetic field, inducing a net magnetic polarity along the magnetic field [Figure 2.1B]. Protons may align with the magnetic field in a parallel (i.e. their magnetic moment follows the magnetic field, a low energy state), or anti-parallel (high energy state) to the magnetic field. Protons tend to prefer low energy states, so the overall number of protons in the low energy state exceeds those in the high-energy state (the size of this difference scales with the magnet field strength). The imbalance in the parallel and anti-parallel proton configurations induces a net magnetic field along the axis of the magnetic field, which is fundamental to generating an image. When held in a magnetic field, the axis of rotation of individual hydrogen protons continues to oscillate slightly at a frequency (known as the Larmor Frequency) [Figure 2.2A], which is proportional to the strength of the magnetic field. This is known as precession. Two key principles of magnetic resonance, 'excitation' and 'relaxation', exploits these properties of protons in order to construct images of the brain.

Excitation

When protons are bombarded with energy, their conformation within the magnetic field changes, pushing their state away from the parallel 'low-energy' configuration towards the anti-parallel 'high-energy' state. In MRI, energy is applied to protons using radio frequency energy (RF). If the frequency of this energy is equal to the Larmor frequency, the rotational pole of the proton is 'flipped' towards the high-energy state, in a process known as 'excitation'. With enough strength, RF energy is able to "excite" protons into a high-energy state such that the net magnetisation in a group of hydrogen protons flips 90° to the X-Y plane, perpendicular to the axis of the magnetic field. [Figure 2.2B top]. A second phenomenon that occurs when a group of protons are 'excited' is that the angle of precession aligns, such that the protons begin to precess 'in phase' with one another [Figure 2.2B bottom].

Relaxation

Protons in a high-energy state are thermodynamically unstable. Immediately following

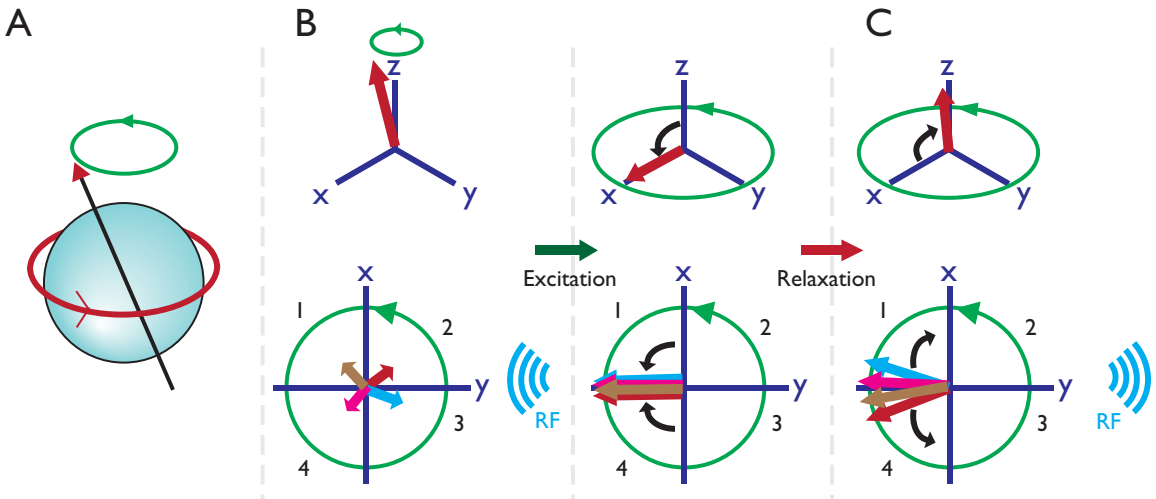

Figure 2.2 | RF excitation and relaxation of free hydrogen ions. A) The magnetic moment of each hydrogen ion processes around the net magnetization vector of the B0 field with a momentum known as the Larmor frequency (green). B) Application of radiofrequency energy, causes the magnetic moment to be 'flipped' by 90° The angle of procession also aligns, so each moment is 'in phase' C) In the flipped state, the magnetic moment is unstable, and rapidly begins to return to the resting state.

excitation, hydrogen protons will begin to return to their more stable low-energy states, releasing excess energy as RF energy in a process known as 'relaxation'. It is this release of RF energy that is detected by the scanner, and from which an image can be generated. The release of RF energy by excited protons is the result of two independent processes: the gradual return of the magnetic phase vector to the z-axis (T1 Relaxation; Figure 2.2C top); and the gradual de-phasing of proton spins (T2 relaxation; Figure 2.2C bottom). T1 and T2 relaxation are independent processes that take effect over different timescales, dependent on the magnetic field strength. T1 relaxation is typically several seconds, whereas T2 relaxation is typically a few hundred miliseconds. Importantly, the rate of T1 and T2 relaxation is dependent on the local properties of protons within tissues, where protons are bound differently. Differences in the rate of T1 and T2 relaxation in different tissue classes gives rise to contrast within the image [Figure 2.3].

The MRI Scanner

Gradient Coils

If an RF pulse was applied to the brain within the MRI scanner without any additional techniques, then all protons within the brain would be equally excited and the signal received by the MRI scanner would be comprised of a mixture of relaxation from a range of different locations - essensially the entire brain. In order to reconstruct an image with fine spatial definition, the scanner uses a series of magnetic 'tagging' approaches in order to localise signal to a specific region of the scanner. This is typically done using a collection of magnetic coils called 'gradient coils' [Figure 2.4A]. Gradient coils induce additional magnetic fields inside the static B0 field. During a typical acquisition protocol, these coils work together to generate the Slice, Phase and Frequency Gradients [Figure 2.4B].

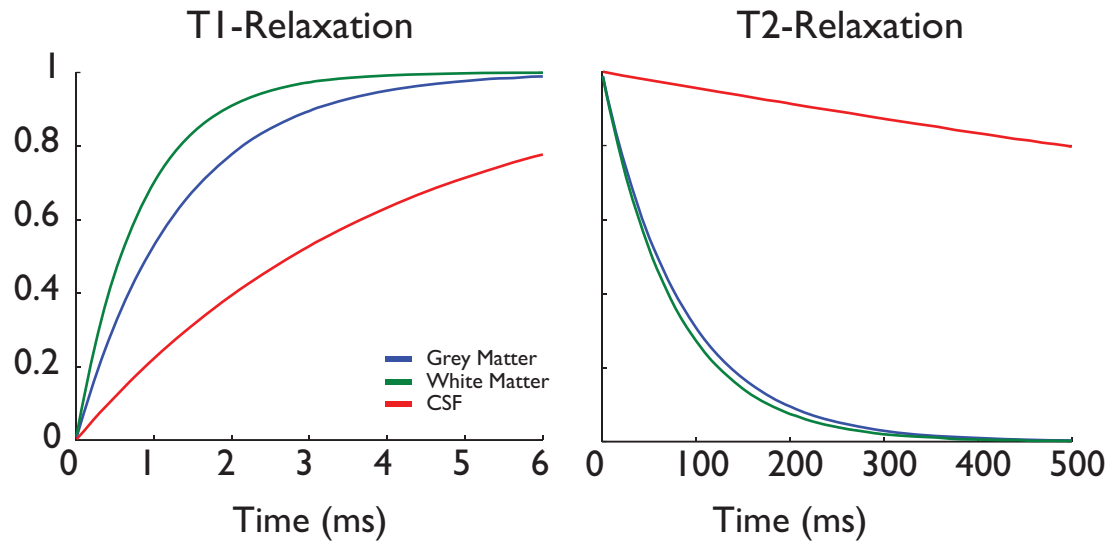

Figure 2.3 | T1 and T2 relaxation rates for different tissue classes. T1 and T2 relaxation rates are dependent on the proton density of different tissue classes. T1 relaxation occurs very rapidly (1-6ms) and T2 relaxation is slower (100-500ms) Green – White matter, Blue – Grey matter, Red – CSF.

Slice Gradient [Figure 2.4B Top]

Images are usually acquired one slice at a time, and one line of voxels within that slice at a time. The Slice Gradient can be used to determine a plane (slice) through the brain from which a whole-brain image is to be constructed, by generating a small gradient in the magnetic field along the Slice 'encoding' direction. The introduction of a small magnetic field minutely alters the Larmor frequency of protons. Thus, when RF energy of a highly specific frequency is introduced into the tissue, only a small slice of the tissue is excited, and thus any RF signal detected will be from a known slice of the tissue. The width and location of this slice may be altered by changing the bandwidth and frequency of the excitation RF pulse

Phase Encoding Gradient [Figure 2.4 Middle]

Once a specific slice has been excited the slice gradient is switched off, and the phase and frequency gradients are used to 'encode' signal within individual regions or 'voxels' of the selected slice. The transient phase encoding gradient (which is at a 90^{O} angle to the Slice and Frequency encoding gradients), introduces a small magnetic gradient across the excited slice of brain that once again briefly modulates

the Larmor frequency of the slice excited protons. This effectively means that the phase synchronisation induced by the initial RF excitation is slightly modulated, and a gradient of net magnetic phase is induced along the phase encoding direction within the tissue. As RF energy is released from the slice, an individual 'line' within that slice can then be recognised by the phase of RF energy detected.

Frequency Encoding (Readout) Gradient [Figure 2.4 bottom]

Finally, the frequency-encoding gradient (which is at a 90^{O} angle to the Phase and Slice encoding gradients) is switched on, which induces a magnetic field along the frequency direction. Like the phase encoding step, this will change the Larmor frequency of hydrogen protons within the selected slice, such that there is now a gradient of frequencies along the Frequency encoding gradient. The frequency-encoding gradient is often described as the 'readout' gradient, as it is during the frequency-encoding gradient that the signal is read by the RF Receive coils. Combined with slice selection and phase encoding gradients, the readout gradient allows

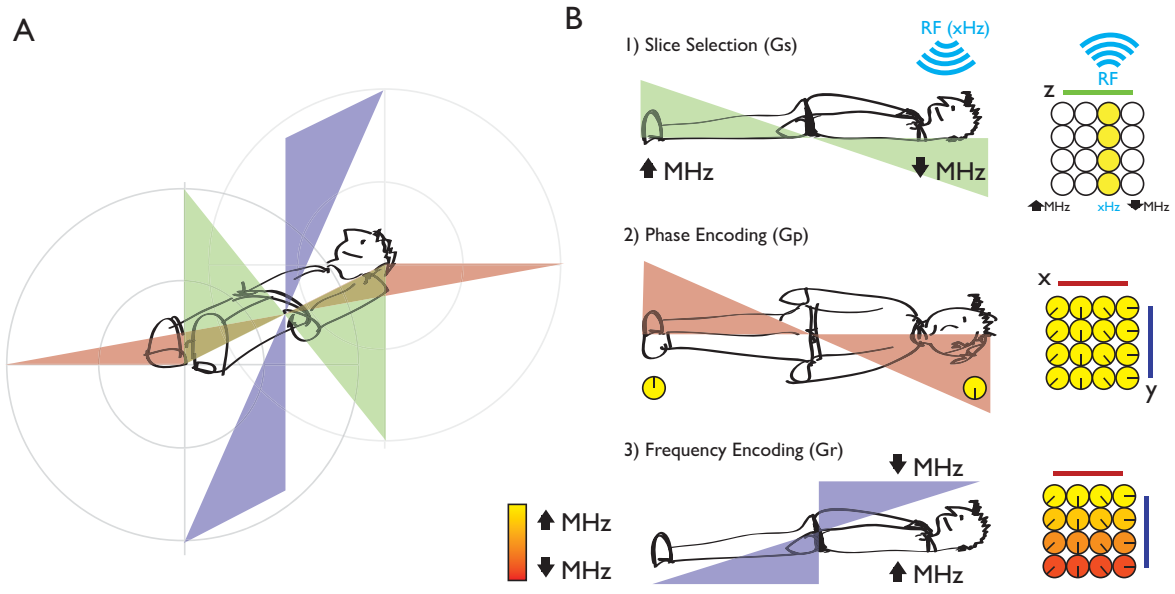

Figure 2.4 | Main imaging gradients of the MRI scanner Signal within specific regions of the brain can be identified through the use of three separate 'encoding gradients' which are perpendicular each other. A) A schematic of the main magnetic field (BO), with the Slice Selection (Green), Phase Encoding (Red) and Frequency Encoding (Blue) gradients superimposed. B) A schematic representation of slice selection and RF encoding imposed by each gradient.

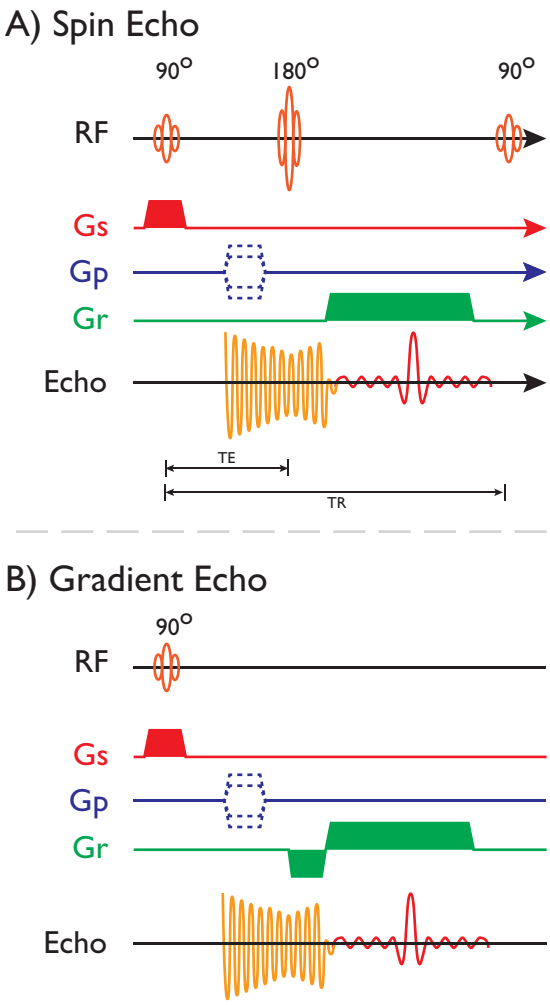

Figure 2.5 | Pulse sequences for MR acquisition Schematic representations of key pulse sequences for MR acquisitions. A) Spin Echo sequence, where T2 relaxation is recovered by the application of a 180O RF pulse following the phase encoding step. B) Gradient Echo sequence, recovery of the T2 echo can be achieved using a fast switching frequency encoding gradient, rather than an additional RF pulse, providing subtly different effects, such as retained sensitivity to T2* relaxation.

localisation of RF along a specific line, as each voxel will return a slightly different frequency of RF energy.

Sequences.

In order to detect RF energy released from tissue during relaxation, receive coils, which are essentially tightly wound coils of wire, are used. As RF energy passes through the receive coils, electric current is induced within the coil. However, the magnetic field within the scanner also induces an electric current within these coils unless they are perpendicular to the primary B0 Field. This has the effect that the signal received is dependent on the T2 relaxation time. T2 relaxation time is very fast compared to T1 relaxation [Figure 2.3]. In practice, factors such as local inhomogeneity of the B0 field caused by paramagnetic interactions within tissue causes T2 relaxation time to be considerably shorter still. These effects are known as T2* decay effects. Such rapid relaxation is a problem, as it only allows a very short time for switching gradients and acquisition of the signal. For this reason, complex 'sequences' of excitation have been developed in order to not only overcome this limitation by re-building the T2 echo, but also exploit the differences in T1 and T2 relaxation to provide different 'contrasts' that are useful for examining different types of tissue.

Spin Echo [Figure 2.5A]

Spin-echo imaging sequences allow the T2 signal to be rebuilt from the de-phased signal by the introduction of a 180^{O} 're-focusing' pulse some time after the initial 90^{O} flip pulse. Effectively, this second pulse 'reverses' the direction of the magnetisation vector fanning out in the X-Y plane to be reversed [Figure 2.2C], such that the T2 signal gradually builds back up, causing an 'echo' of the original T2 relaxation independent of T2* related effects.

Gradient Echo [Figure 2.5B]

It is also possible to achieve the same echo effect using a rapid switching of the

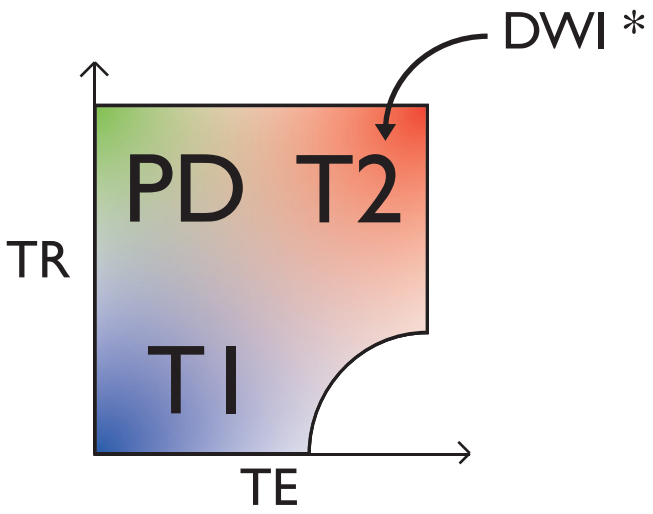

Figure 2.6 | TR and TE determine overall image contrast An overview of the relationship between repeat time (TR) and echo time (TE), and the relative contribution of T1 and T2 relaxation with the image contrast. Diffusion lighted Images (DWI) are usually T2 weighted, but with additional gradient requirements.

gradient coils as opposed to an additional 180^{O} RF Pulse. Unlike spin-echo sequences, because the rephrasing is achieved using switching magnetic fields, the resulting sequence retains strong T2* sensitivity. This can be considered advantageous, as T2* relaxation has some favourable properties, which are useful to study functional activity in the brain. Specifically, the localised anatomical effects that lead to T2* effects are particularly sensitive to the presence of oxygenated and deoxygenated Haemoglobin (see 'Principles of Blood Oxygen Level Dependent (BOLD) fMRI').

Echo Planar Imaging (EPI)

Traditional MRI imaging techniques are relatively slow to collect an entire image of the brain, as the image is collected one line at a time following each RF pulse. EPI sequences are faster as they collect multiple echoes from each RF pulse, by continuing to switch the readout gradient as in-gradient echo sequences. By using additional short 'blips' of the phase encoding gradient to 'undo' the phase encoding step, the readout line gradually changes for subsequent echoes following the RF pulse. EPI is sensitive to the T2* relaxation rate, but can be acquired at high speed (~3 Seconds) for the entire volume of the brain. Full brain 'volumes' can then be repeatedly acquired

to examine changes across time. This makes EPI sequences useful for acquiring data for applications that require rapid acquisition, such as during fMRI experiments, and that are sensitive to T2* relaxation as a proxy of blood flow. The trade-off of the faster time to collect a single image of the brain is that the spatial resolution of the image is considerably lower (typically 3x3x3 mm). EPI images are also more sensitive to artifacts and distortion. As a result, EPI images are often registered to higher resolution images during the analysis pipeline.

Contrast [Figure 2.6]

As different tissues have different properties in terms of proton density and binding, alteration of different properties of the aquisition can be used to select an approprate "contrast" to view specific strucutres or biological properties of tissues. This can be useful to examine different pathologies, or different types of tissue such as grey or white matter. There are two key parameters of the acquisition protocol that are important in determining contrast. The first is the Repetition time (TR), which is the length of time between repeats of the 90^{O} excitation pulse. The second is Echo Time (TE), which describes the length of time between the 90^{O} pulse and the acquisition of signal. In spin-echo sequences the 180^{O} pulse is positioned at half of the TE, whereas in gradient echo imaging the reversed frequency-encoding gradient is half of the TE [Figure 2.5]. T1 and T2 relaxation times, as well as proton density, vary across tissues [Figure 2.3], therefore it is clear that by modulating the TE and TR different tissue contrasts can be achieved in the resulting image, as the readout will capture a different phase in the T1 and T2 relaxation curves. The echo-time and repetition-time may be much shorter than either T1 or T2 relaxation. Therefore, by changing the TE and the TR, signal (S) is captured with specific contrasts, which are dominated by either T1 or

T2 relaxation according to the following equations (Mori and Zhang 2006):

$$S_0 = PD\left(1 - e^{-\frac{TR}{T1}}\right)e^{-\frac{TE}{T2}}$$

$$S = S_0 e^{-bD} \qquad \text{(Equation 2.1)}$$

Where PD is the local proton density, T1 and T2 are the relaxation time constants for a particular tissue compartment, and b and D are the gradient strength and the coefficient of local diffusion of protons (mm^2/s), respectively.

T1-weighted images

If we keep the TE short, the contrast in the resulting image is largely unrelated to T2 relaxation as there has not been enough time for it to occur. If the TR is also relatively short, then T1 relaxation has not completed by the start of the next RF 'excitation', and therefore the effective magnetisation vector for the next echo is smaller for some tissues than others. Therefore, the contrast in the image at the TE will be strongly affected by the T1 relaxation process. These images are known as T1-weighted images, usually used to construct structural images of the brain as they have good contrast between the grey matter, white matter and CSF compartments of the brain.

T2-weighted images

T2-weighted images are acquired when the TE and TR are relatively long. The long TR contributes very little to the image contrast, as T1 relaxation has largely completed by the start of the next RF pulse. However, there is some redundant signal in the T2 relaxation at a short echo time, meaning that contrast is largely affected by T2 relaxation. T2 weighted images that are associated with a gradient echo sequence are further sensitive to T2* relaxation – this additional property is important in the acquisition of blood oxygen dependent (BOLD) imaging used in functional MRI (see 'Principles of Blood Oxygen Level Dependent (BOLD) fMRI').

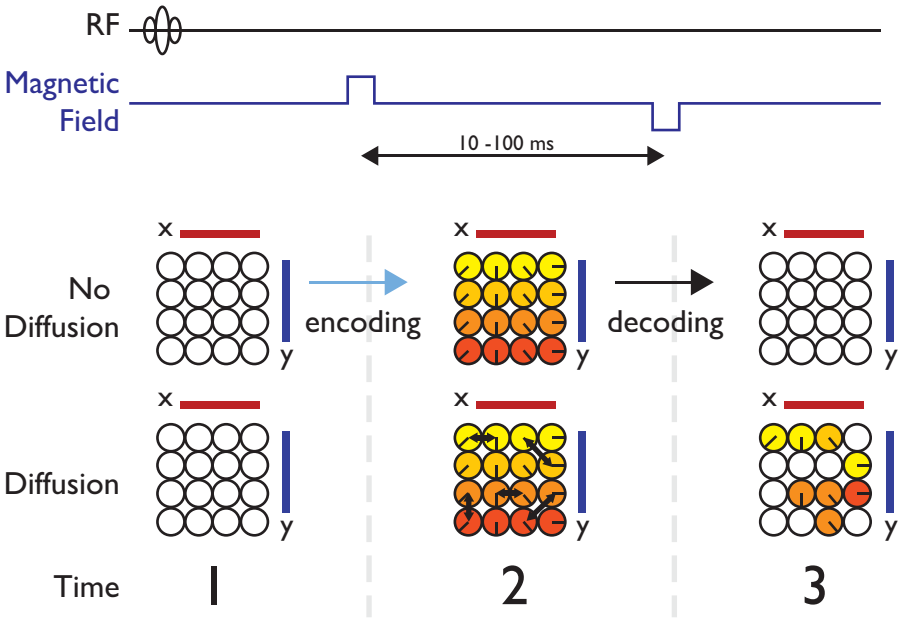

Figure 2.7 | Pulse sequence for diffusion weighted imaging. An overview of the theory of diffusion weighted acquisitions. Following the usual gradient echo excitation package, an additional rapidly switching of a highly directional magnetic field is used. The first pulses 'encode' slices as usual, however, the second pulse is designed to 'undo' this encoding. If water diffuses along the axis of the magnetic gradient, the decoding gradients fail to fully decode the selected slice and thus returned RF energy would be badly matched to expectations, leading to signal dropout in the image which relates to diffusion of water.

Diffusion weighed images.

Diffusion weighted images (DWI) are sensitive to the diffusion of water along a specific vector in addition to standard T2 or T1 relaxation. Determining the diffusion coefficient along a particular vector within a voxel may be desirable, as it provides information about the microstructure of the brain. [Equation 2.1] demonstrates that the effect of diffusion on signal contrast increases exponentially, depending on the strength of the encoding gradients. For most applications, where the strength of the encoding gradient strengths are very small (b~0), the effect of diffusion on the signal is very small. Like T2-weighted images, DWI has a long TR and TE. However, unlike conventional T2-weighted sequences, DWI readout occurs following an additional pair of strong (b~1000) opposing magnetic readout gradients oriented around the desired diffusion vector, approximately 10-100ms apart [Figure 2.7]. The first gradients have the effect of 'phasing' hydrogen protons within the tissue, such that there is an order in proton spin phases along the axis of the imposed magnetic gradient. The

second 'dephasing' gradient is designed to 'cancel' the effect of the first phasing gradient. If there is no diffusion of water along the axis of the gradient between the 'phasing' and 'dephasing' fields [Figure 2.7 Top], rephasing will be complete, and no signal dropout occurs compared to standard diffusion-free T2 imaging. However, if a significant amount of diffusion along the gradient occurs [Figure 2.7 bottom], the rephrasing gradient will incorrectly rephase protons, leading to signal dropout compared to a standard T2 image. This information can be used to reconstruct the assumed diffusion coefficient (ADC) along the gradient vector by comparing the diffusion weighted image (b~1000) with a standard T2-weighted image (b~0), by re-arranging the [Equation 2.1]:

$$B_0 = S_0 e^{-b_0 ADC}$$

$$S_1 = S_0 e^{-b_1 ADC}$$

$$\therefore \frac{S_1}{B_0} = e^{-(b_1 - b_0) ADC} \qquad \text{(Equation 2.2)}$$

$$\therefore ADC = -ln(\frac{S_2}{S_1})/(b_1 - b_0)$$

Multiple DWI collected using different gradient strengths and vectors may be used to infer the white matter structure of the brain (See 'Diffusion Tensor Imaging').

Functional MRI (fMRI)

Principles of Blood Oxygen Level Dependent (BOLD) fMRI

Neural activity within a particular region of the brain requires additional energy above the baseline level, and so at the site of neural activity the metabolism of oxygen and glucose is increased in order to meet the increased energy demands. In order to meet the increased energy demand, there is an increase in cerebral blood flow. This increase in blood flow peaks at around 5s after the onset of a local net increase

of neural activity, followed by a short 'undershoot' as blood flow returns to baseline ~25s after a transient increase in activity [Figure 2.8]. This evoked signal is known as the canonical haemodynamic response function (HRF). The flow of blood in the brain is detected using T2* imaging, by exploiting the differing paramagnetic properties of oxygenated (HbO2) and deoxygenated-Haemoglobin (Hb). In areas of high-energy demand, the proportion of HbO2 to Hb is relatively reduced due to increased metabolic demand. As HbO2 and Hb have differing magnetic effects, this change is detectable as a local inhomogeneity within the B0 magnetic field (BOLD signal), decreasing the T2* relaxation time (see 'Sequences, Contrast' above). Compared to baseline, images under task conditions therefore allow the visualisation of areas of the brain that increase activity in response to a stimulus, task or response (Friston 1997, Savoy 2001).

Analysis of fMRI data

Typically a functional imaging session consists of acquiring a high-resolution structural image (T1-weighted) and a number of functional images (T2*-weighted

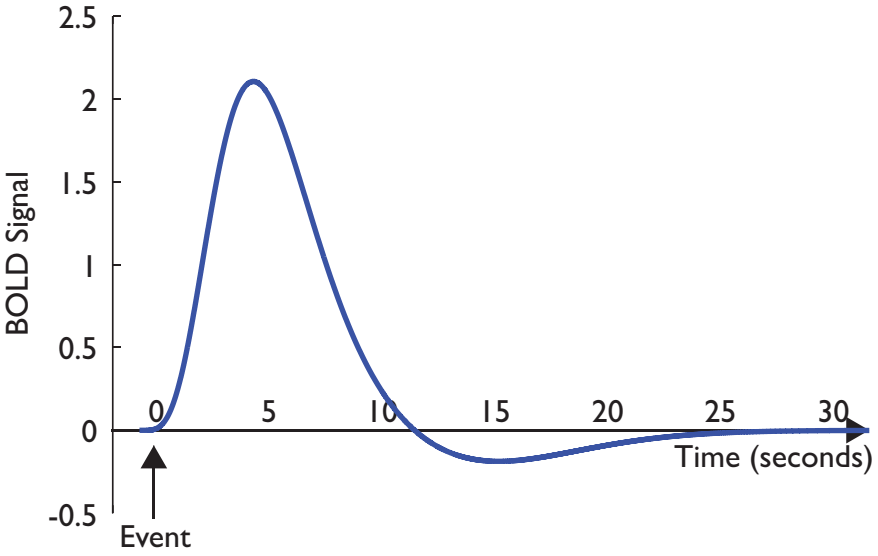

Figure 2.8 | Canonical HRF Response Following an neural event, the BOLD signal slowly builds over the course of ~ 5 seconds, as local blood flow increases due to increased local metabolic demand. BOLD signal then rapidly decreases over the course of the next ~20 seconds.

EPI acquisitions). In order to compare functional data across different subjects and functional imaging sessions, as well as correcting for motion and scanner related artefacts within the data. T1-weighted and EPI images from the scanner are initially subjected to a number of standard preprocessing steps, to minimise certain artefacts. Functional and structural data analysed within this thesis were preprocessed using tools within the FMRIB Software Library (FSL) (Smith et al. 2004, Woolrich et al. 2009) and Freesurfer (Dale 1999, Desikan et al. 2006, Fischl and Dale 2000, Fischl et al. 2002, Fischl, Salat, et al. 2004, Fischl, Tootell, and Dale 1999, Fischl, van der Kouwe, Destrieux, Halgren, Ségonne, et al. 2004) (see individual results chapters for detailed methodology for individual studies).

Preprocessing

Brain extraction

Brain Extraction is used to remove non-brain issue from the structural image (T1) of the brain, which aids image co-registration (see 'Registration' below). Brain extraction is performed using the FSL Brain Extraction Tool (BET). This tool works by identifying the centre of the brain, and expanding a spherical surface out from this location in order to find an optimal separation between neural tissue, skull and non-brain tissue. (Smith 2002)

Temporal filtering

Alongside signal within the EPI sequence that is due to the T2* susceptibility induced by the BOLD response, other sources of noise are present in the data, which are attributable to additional factors (For example, minor instabilities in the scanning hardware due to heating of the gradient coils) These sources of noise likely induce a very slow 'baseline drift' in the data, significantly slower than the BOLD signal, which acts over the course of around 5-20s (see 'Principles of Blood Oxygen Level Dependent (BOLD) fMRI'). These small distortions in the data are corrected using a

high-pass fourier filtering approach, with a cut-off frequency in the order of 0.01-0.02 Hz.

Motion correction

In addition to correcting for baseline drifts in functional data, the movement of the subject within the bore of the scanner introduces distortion within the EPI image over time. Motion-correction approaches ensure that the anatomical location of individual regions of the brain is consistent across the duration of the scan, by registering each volume within a functional dataset to a common 'example' image. This is carried out by calculating the affine transform of each volume to the example. In addition to realighing each image, this transform can be used to calculate the motion of the brain within the scanner across the entire duration of the scan, which results in the generation of timecourses representing 6 parameters of movement along and about each axis in 3D. Although subjects with excessive motion within the bore of the scanner are eliminated for further analysis, and minor misalignments corrected, motion also induces additional unwanted signal into the data. This is because movement of the brain following the RF excitation pulse will lead to an incorrect assumption of the spin-history of localised regions of the brain during the readout, resulting in small but significant levels of artefactual signal. Approaches for correcting such signals are a topic of on-going debate within the research community (Power et al. 2014, Power, Schlaggar, and Petersen 2015). In particular, the use of global signal regression to correct for motion-induced artefacts is contentious (Fox et al. 2009). A compromise is to use the General Linear model to regress a volterra expansion of the motion parameters (Friston 1997), alongside the mean signal within a non-cortical area such as the white matter (WM) or cerebrospinal-fluid (CSF) that is distant the functional signal within gray matter.

Spatial smoothing

Further high-frequency spatial noise may be introduced into functional data as a

result of local field inhomogeneity and radio frequency noise within the scanner. As the BOLD signal is coupled to the HRF, the spatial order of biologically plausible activity ought to smooth across several millimeters (typically covering several voxels at once). In order to improve the signal-to-noise ratio of EPI volumes, data are spatially convolved with a gaussian kernel with a full-width half maximum size of between 5-8 mm (the approximate diameter of active clusters of voxels).

Registration

In order to compare functional data across multiple subjects, or across a series of functional EPI 'runs', the images must be coregistered to a common image. This ensures that individual regions of the brain in each functional image 'line up' across the group. Typically the registration protocol is to: a) co-register the EPI data to the structural T1; and b) 'normalise' by further registering the T1 image to a common T1 atlas brain. A commonly used T1 atlas is the Montreal Neurological Institute 152 (MNI-152), generated from 152 healthy control subjects (Grabner et al. 2006). Many different registration protocols exist, but three are in common use and are described below.

Linear Registration

Linear registration calculates a 'rigid body' transformation between two individual images. It achieves this by stochastically tuning a 'transformation matrix' that describes the scaling, translation, skew and rotation of the 'movable image' to a template. A cost function based on mutual information is used to tune the linear transformation matrix, by fitting the transformed movable image to the reference image. Linear registration is often employed to co-register the structural T1 image to the EPI data. The poor spatial resolution of EPI and the additional distortion due to T2* effects is a challenge to registration techniques. However, the topologies of the EPI and T1 images are similar, which enhances the success of EPI to T1 co-registration.

Non-Linear Registration

The demands of registration between the T1 structural space of the brain and an arbitrary atlas template are significantly greater than for the registration of EPI to a T1-weighted image, as there is a significant variability in brain shape, size and structure between individuals. In practice, linear registration provides a reasonable estimation of the registration between T1 and atlas space. However, individual differences can be better accounted for by further fine-tuning the registration between the T1-weighted image and atlas space by calculating local deformations in the transformed image compared to the atlas brain (Andersson, Jenkinson, and Smith 2007). The 'warp field' is then tuned to further enhance the fit between the transformed T1-weighted image and the atlas brain.

Boundary Based Approaches

In practice, both linear and non-linear approaches to registration yield fairly impressive co-registration results. Linear registration can be further improved by using a modified 'boundary based' cost function (BBR) to enhance model fit. This approach utilises the significant difference in the signal intensity (due to differences in the T1 and T2 relaxation rate) between grey matter and white matter to optimise the cost function during registration (Greve and Fischl 2009). BBR uses a structural 'segmentation' of the structural T1-weighted image, which models the location of the white/grey matter boundary as a surface of polygons. Linear registration methods are used to align this surface with the EPI, and samples of difference between the intensity either side of this boundary are used to calculate the cost function for registration. Good registration is achieved when there is a large intensity difference of the correct sign between either side of the surface. There are several approaches to generating structural segmentations, such as Freesurfer (Dale 1999, Desikan et al. 2006, Fischl and Dale 2000, Fischl et al. 2002, Fischl, Salat, et al. 2004, Fischl, Tootell, and Dale 1999, Fischl, van der Kouwe, Destrieux, Halgren, Segonne, et al. 2004) and FSL's FAST (Zhang,

Brady, and Smith 2001). Segmentation can be further used to generate atlas-defined regions of interest (ROI), and it provides useful information about the structure of the cortex, such as its thickness, volume and surface area.

Analysis using the General Linear Model (GLM)

In the GLM approach, the BOLD Signal (Y) within each individual voxel is assumed to be a linear combination of signals of interest (X_i), termed explanatory variables (EVs), and a noise variable (ε):

$$Y = \beta_0 + X_1\beta_1 + X_2\beta_2 + X_3\beta_3 + \cdots + \varepsilon$$

According to this equation, for each individual voxel of an EPI time-series image, we can use least-squares regression to determine a weight (β_i) of each individual EV in Y. In the case of functional imaging data, explanatory variables may be the time-course of some psychological variable defined by the experimental design (e.g. a visual stimulus on screen), or some nuisance variable that is assumed to form a constituent part of , such as movement (Beckmann, Jenkinson, and Smith 2003, Friston 1997). Evaluated across the entirety of the brain, a statistical map for each EV is generated, using either parametric approaches or more flexible but computationally intense non-parametric approaches based on randomisation (Winkler et al. 2014, Nichols and Holmes 2002). This map can be examined in isolation, where the denominator is the remaining term, or a contrast with another parameter estimate (COPE); for example, a task-dependent state EV with baseline state EV. This provides a t-score between the two behavioural states at each voxel, which can be interpreted as a 'activation' or 'deactivation' for a specific region in the brain.

A mass univariate analysis such as this has a multiple comparison correction problem, as each of > 500,000 voxels are effectively independent t-tests. Using a conservative multiple-comparison approach such as Bonferonni at this level, would offer little

chance of observing any signal at a level of significance. Therefore, alternative cluster-based approaches for multiple comparison correction are used instead (Worsley et al. 1992). These approaches make use of 'random field theory' for inference, as the signal from an active brain region will spread over a number of neighbouring voxels. For any particular FWHM smoothing kernel it is possible to estimate the size of clusters which should survive 'by chance'. Clusters with a size above this threshold, which can be estimated using a standard distribution, can be considered to be significantly active.

Data-driven functional connectivity analysis

The need to define psychological regressors a priori is a significant limitation to examining neural activity over time, especially when considering resting state data acquired without an explicit experimental task. Furthermore, as discussed above, mass-univariate approaches have significant inference problems in terms of multiple comparison correction. Independent component analysis is a data compression technique that has the power to overcome these limitations, by representing complex datasets such as 4D EPI data as a collection of independent spatial functional connectivity maps and associated time courses, which together retain a meaningful amount of the variance of the original dataset (Beckmann et al. 2009, Beckmann et al. 2005). Importantly, these spatial maps and timecourses can be estimated without prior knowledge of en experimental design or timecourse.

Principles of ICA for fMRI

In the ICA approach, the BOLD signal across the entire brain, rather than each individual voxel, is considered simultaneously. Data from a 4D EPI acquisition is represented as a matrix (Y) of voxels by time (t), which can be constructed by a linear mixture of a group of individual 'source' maps (S) represented as an matrix of m voxels by n estimated sources, mixed across time according to a t x n 'mixing matrix' (A) (McKeown, Jung, et al. 1998, McKeown, Makeig, et al. 1998, McKeown and Sejnowski

1998):

$$Y = AS$$

There are multiple approaches to the source estimation for ICA approaches. Most commonly, A and S are estimated simultaneously, such that S is a matrix optimised to contain statistically independent spatial maps of size m in each row, with an internally consistent temporal dynamic represented in each of the associated columns of the 'mixing' matrix (A). This means that each map within S represents a collection of voxels, within which all voxels are temporally 'related' within the dataset, generating functional connectivity networks. The level of compression employed by the ICA algorithm can be determined by altering the number of columns in S during estimation. A common implementation of ICA for fMRI datasets used in this work is implemented as MELODIC in the FSL software library (Smith et al. 2004, Woolrich et al. 2009).

Diffusion Tensor Imaging (DTI)

Principles of the diffusion tensor

In Equation 2.2, the diffusion coefficient (ADC) along a specific 'vector' may be determined using T2-weighted images taken at a range of different diffusion coefficients or 'weights'. In order to fully estimate diffusion would require the acquisition of images at many thousands of different gradient vectors, which would be impractical. Instead, a popular approach to estimation of voxel-wise diffusion is to use a small selection of vectors about a sphere and fit a 'diffusion tensor' to the resulting dataset (Basser, Mattiello, and LeBihan 1994). In the tensor model, diffusion along each of >6 (commonly ~64) 'diffusion vectors' is fitted to an ellipsoid in three dimensions [Figure 2.9]. The properties of the fitted 3D ellipsoid can be fully described by 6 parameters - the three dimensions of the ellipsoid (eigenvalues; v1, v2 & v3) and vectors representing the orientation of fibres (eigenvectors; λ1, λ2 & λ3). [Figure 2.10] demonstrates the field of primary eigenvector and eigenvalues

across a region of the brain. In the CSF, eigenvalues are large, the result of isotropic diffusion caused by a lack of microstructure to constrain diffusion. Water movement in grey matter is constrained, but eigenvalues are relatively equal, suggesting that whilst water is constrained, there is no net direction of water diffusion within the voxels. In contrast, within white matter diffusion is constrained along the direction of tracts. The directionality of diffusion defined by the eigenvectors can be used to 'reconstruct' pathways of white matter fibres within the brain, a technique known as tractography.

Eigenvalues and eigenvectors can also be used to generate metrics that describe the shape and amount of diffusion within an individual voxel. Fractional Anisotropy (FA) describes the overall constraint of water within a voxel (Basser et al. 2000, Basser and Pierpaoli 1998, 1996):

$$FA = \sqrt{1/2}\,\frac{\sqrt{((\lambda_1, - \lambda_2)^2 + (\lambda_2 - \lambda_3)^2 + (\lambda_3 - \lambda_1)^2)}}{\sqrt{{\lambda_1}^2 + {\lambda_2}^2 + {\lambda_3}^2}}$$

When FA is near to 0, then diffusion is isotropic. Values closer to 1 suggest that diffusion is highly constrained (anisotropic).

Mean Diffusivity (D^M), describes the overall assumed diffusion coefficient within a voxel. When D^M is low, there is very little movement of water within the voxel. High

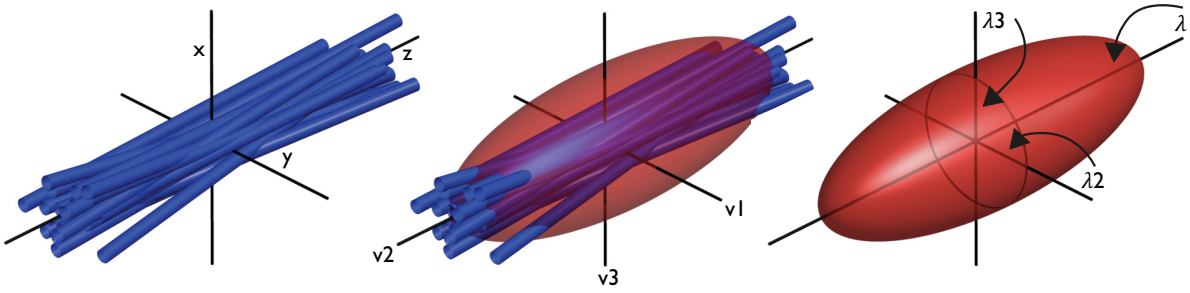

Figure 2.9 | Introduction to the diffusion tensor Diffusion of water in each voxel, is modelled using the diffusion weighted signal along each of the measured diffusion gradients, fitted to an ellipsoid. The tensor ellipsoid can be described using 6 parameters, v1-3 which describe the mean signal in each direction, and λ1-3 which describe the assumed angle of diffusion in each direction

D^M suggests high diffusivity of water.

$$D^M = \frac{1}{3}(\lambda_1 + \lambda_2 + \lambda_3)$$

Finally, it is common for diffusion in axial (D^{AX}) and radial (D^{RAD}) directions to be measured. D^{RAD} is thought to be a quantity that represents the degree of restriction due to membranes and may be a marker of axonal demyelination (Song et al. 2003, Song et al. 2002).

$$D^{RAD} = \frac{1}{2}(\lambda_1 + \lambda_3)$$

$$D^{AX} = \lambda_1$$

DTI data analysis

Pre-processing

Pre-processing of raw EPI diffusion weighted data often follows similar protocols to that used for functional MRI (see 'Analysis of fMRI data' above). Initially, each volume of a DWI sequence is re-orientated and corrected for small spatial distortions introduced by eddy currents induced at high magnetic field gradients (Mohammadi et al. 2012, Haselgrove and Moore 1996, Jezzard and Balaban 1995, Jezzard, Barnett, and Pierpaoli 1998), using an affine (linear, see above) registration to the associated b=0 image. To reduce the complexity of tensor calculation, the b0 image is also brain extracted (see 'Brain Extraction' above), reducing the tensor-field calculation to a field of view encompassing only neural tissue. Voxel-wise diffusion tensor fitting is then performed, using a least-squares approach to the tensor model. For DTI data presented in this thesis, analysis was performed using FMRIB's Diffusion Toolbox (FDT

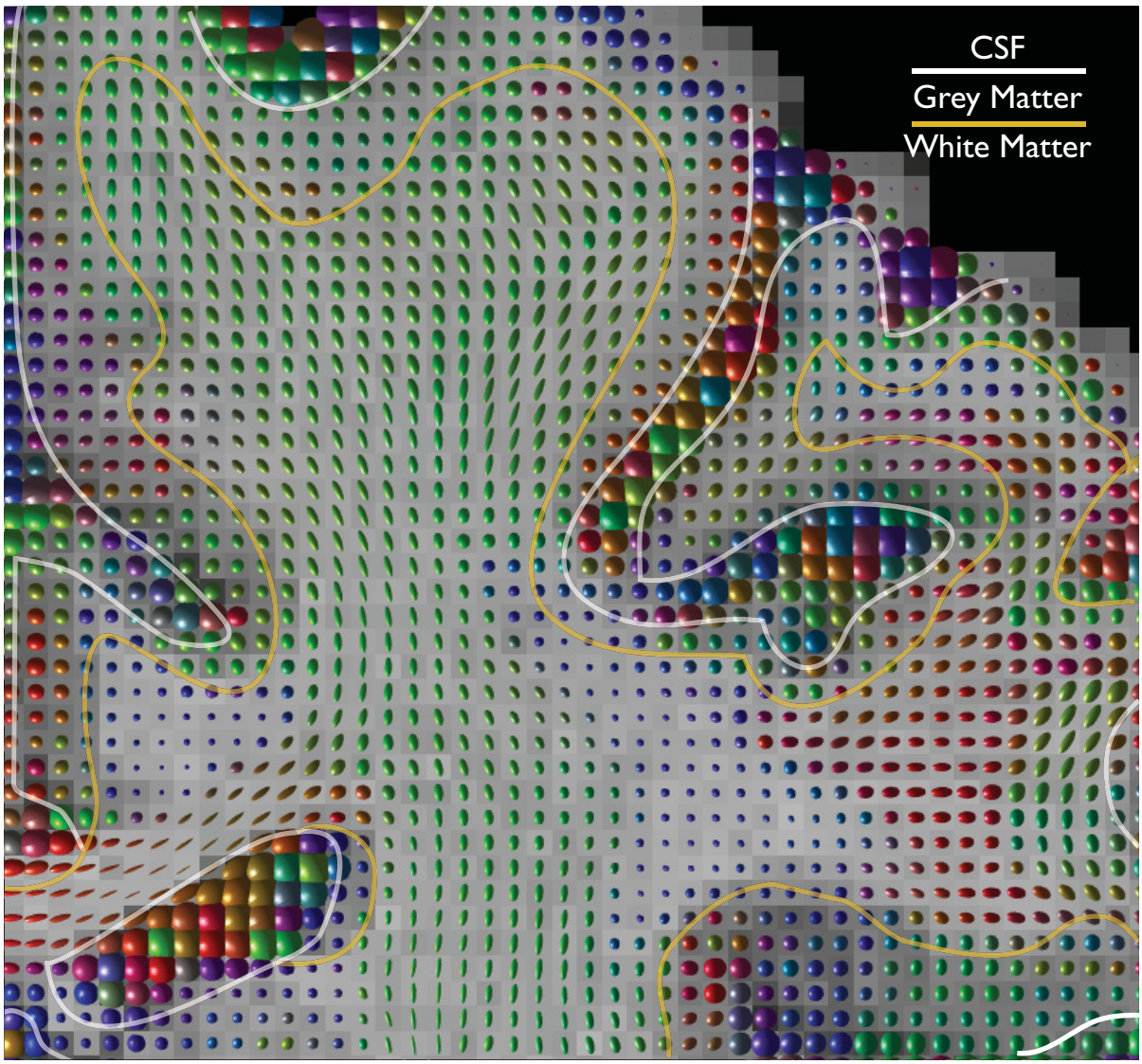

Figure 2.10 | Voxelwise estimation of diffusion tensor Here, the diffusion tensor has been estimated and visualised at each voxel of a 25 year old healthy male. Within the white matter, diffusion is often highly structured and restricted along a specific vector. Within the grey matter compartment, water is still largely restricted, but along no specific vector. Within CSF, water is free to diffuse freely.

v2.0) (Behrens, Johansen-Berg, et al. 2003, Behrens, Woolrich, et al. 2003b).

Analysis

Voxel-Based approaches (TBSS).

A popular approach to examining the relationship between white matter structure revealed by DTI data is to treat the metrics of white matter structure in each voxel across a group of subjects as the response variable in a general linear model. Similar to longitudinal analysis of fMRI data, the signal in each voxel across the group is considered as a linear combination of a range of explanatory variables and an additional noise factor (see 'Analysis using the General Linear Model (GLM)' above). Using such an approach allows the data-driven identification of regions of white matter associated with specific EVs that correspond to categorical factors such as the precedence of pathology relative to a control group, or continuous variables such as age. However, in order for the analysis to be conducted across a group, images for individual subjects must be normalized against an atlas template (see 'Registration' above). For DTI data this becomes a significant confound, as normal variation in tract structure and extent introduced by differences in volume and shape of the brain between subjects, introduces a 'partial voluming' effect to the data. Partial voluming is particularly pronounced when comparing brains with pathology, especially when atrophy is present. Tract-based spatial statistics (TBSS) is an approach to reducing the complexitiy of the white matter structure to smaller regions of the brain 'tracts', where the presence of white matter alone is consistent across groups (Smith et al. 2006), thereby reducing inter-subject variability. TBSS works by using non-linear registration (see 'Registration' above) of FA maps in a group of subjects to a common template (often MNI-152), creating a group mean FA map. The FA map is 'thinned' to create a skeleton-which represents the approximate centre of white matter tracts with the smallest inter-subject variability across the group. This reduces the effect of brain size and shape on the results of voxel-wise analysis of diffusion data.

Tractography

White matter comprises the axonal projections of neurons that connect grey matter regions along with supporting cells. Tractography of DTI data assumes that neighbouring voxels form into contiguous 'fibres' passing between voxels, which represent the connectivity structure of the white matter. Two main approaches to tractography are in common use. In deterministic tractograpy, 'streamlines' representing an individual putative tract are estimated using the properties of the diffusion ellipsoid. Most commonly starting at a seed voxel (which is either determined using a specific region of interest, or is placed at the grey-matter/white-matter boundary across the entire cortex), the path of this streamline is constructed step-by-step. Starting at the seed, the primary diffusion vector is followed for a pre-determined distance. The orientation for the next step in the tracking algorithm is then used to continue the streamline. This process is repeated until: the streamline converges with a pre-defined 'termination' region; the length of the streamline is sufficiently long; the curvature of the streamline exceeds a pre-set threshold; or the FA at an ensuing step is too low. This results in a map defining the probable connection between regions of interest. Deterministic approaches are limited, however, as they rely on the primary diffusion direction within each voxel - the appropriate direction of each step is far from being as certain as the tensor model may suggest. Indeed, in the case of some voxels there may be no predominant direction of diffusion. This is especially true in regions of low anisotropy that may occur in regions of the brain where fibre bundles cross. Probabilistic approaches model the uncertainty of fibre orientation direction at each voxel and represent each direction as a probability density function. In probabilistic tractography the vector of each step in the tracking algorithm is determined not by the principle eigenvector, but by this probability function (Behrens, Johansen-Berg, et al. 2003, Behrens, Woolrich, et al. 2003a), effectively meaning that where fibres cross it is likely that the fibre tracking algorithm will follow either of the appropriate fibre directions. Consequently, the spatial extent of repeated estimations of streamlines

between specific voxels, compared to deterministic approaches have some degree of uncertainty. It is commonplace therefore for streamlines from individual voxels to be repeated multiple times, generating an overall probability distribution map for the spatial extent of the fibre, which may then be thresholded and used as a ROI for further analysis.

Individual prediction of white matter injury and cognitive outcome following traumatic brain injury (TBI)

3

Introduction

Traumatic brain injury (TBI) often results in traumatic axonal injury (TAI). This can be investigated using diffusion tensor imaging (DTI)(MacDonald, Dikranian, Bayly, et al. 2007). Previous studies show that DTI can provide important clinical information in TBI patients, which cannot be obtained using conventional imaging techniques (MacDonald, Dikranian, Bayly, et al. 2007, Sidaros et al. 2008, Kinnunen et al. 2011). However, the best way to use DTI diagnostically is uncertain. The challenge is threefold: (i) to identify the presence of TAI in an individual; (ii) to determine the clinical significance of TAI; and (iii) to predict how it relates to specific behavioral problems and clinical outcome. These goals are challenging as TBI causes a complex

and variable pattern of white matter damage.

Tiny hemorrhages within the white matter (microbleeds) are a pathological marker of TAI and can be identified using gradient echo and susceptibility weighted imaging (Scheid et al. 2006, Beauchamp et al. 2011, Chastain et al. 2009). However, these techniques do not provide a quantitative assessment of white matter integrity, and patients without microbleeds can still show evidence of TAI.(Kinnunen et al. 2011) In contrast, DTI provides quantitative information about white matter damage. (Kinnunen et al. 2011, MacDonald, Dikranian, Bayly, et al. 2007, Sidaros et al. 2008) DTI measures the direction of water diffusion within white matter tracts and allows estimation of the structural integrity of the tract.(Beaulieu 2002, Basser and Pierpaoli 1996) The measures are abnormal shortly after TBI, change dynamically as white matter recovers and may be used to predict clinical outcome.(Sidaros et al. 2008, MacDonald, Dikranian, Bayly, et al. 2007) Although damage to the white matter can be diffuse, the pattern is related to the specific cognitive deficit. For example, DTI abnormality within the fornix is correlated with memory impairment, whereas abnormality within the cingulum bundle is associated with impairment of sustained attention.(Kinnunen et al. 2011, Bonnelle et al. 2011, Sharp et al. 2011)

Previously a type of DTI analysis, tract based spatial statistics (TBSS), to study TAI in groups of TBI patients (Kinnunen et al. 2011). This technique provides a sensitive way of investigating whether TAI is present across different white matter tracts, although it has not been clear how best to apply this technique to individual patients. Here we show how machine learning can be used alongside TBSS to provide diagnostic information about TAI in individual patients. Machine learning is increasingly used to assist complex diagnostic decisions, by integrating multiple pieces of information in the diagnostic process (Sajda 2006). A classifier is trained on data that is already diagnostically labeled, before being applied to undiagnosed data. In this way, generalizability of a classifier to novel patient data can be assessed and an individual prediction made. In this study, various types of pattern classifier were trained using

DTI data from patients with microbleed evidence of TAI. Patients without microbleed evidence of TAI were then classified. The clinical relevance of this 'diagnosis' was validated with reference to the patient's neuropsychological profile. I also show how multivariate techniques can be used to provide predictions of cognitive function in individuals. I went on to compare multivariate and comparable univariate approaches, to test whether the more complex machine learning approach provides additional benefits. The work provides a proof of principle that machine learning techniques can be used with DTI data to provide diagnostic information about clinically significant TAI.

Materials and Methods

Participants

Seventy TBI patients (51 males, mean age ± SD: 35.28 ± 11.5 years) were recruited in the post-acute/chronic phase > two months post-injury (mean 34.2 months). All subjects had attained at least a secondary school level of education. Exclusion criteria were as follows: a history of psychiatric or neurological illness prior to the head injury; a history of previous significant TBI; pregnancy or breast feeding; current or previous drug or alcohol abuse; contraindication to MRI. Of these 70 TBI subjects, a road traffic accident was responsible for TBI in 27 cases, assaults in 18 cases, trips falls or domestic accidents in 16 cases, sports related injuries in 4 cases, one case was the result of syncope, and in 4 cases the cause was uncertain. The severity of TBI was assessed using the Mayo Classification System (Malec et al. 2007). Fifty-one patients were classified as moderate-or-severe and 19 patients as mild. A group of 25 healthy controls (12 males, 33.4 ± 10.2 years) were recruited alongside the clinical group. (For full demographics and clinical details of the patients, see [Appendix 3.1]. A group of 25 healthy controls (12 males, 33.4 ± 10.2 years) were recruited alongside the clinical group. Patients were referred to their local TBI service because of persistent neurological problems. At the time of scanning, 13 of the 70 patients were prescribed potentially psychoactive medications (e.g., anti-depressants, analgesics). All participants gave written informed consent with ethical approval from the Hammersmith, Queen Charlotte's and Chelsea Research Ethics Committee.

Neuropsychological assessment

Sixty-five of the patients (28 males, mean age ± SD: 38.48 ± 12.1 years) completed a standardized neuropsychological test battery. Our analysis focused on three cognitive measures shown to be sensitive to impairments following TBI (Kinnunen et al. 2011): Associative memory (AM), using the immediate recall measure of the People Test

from the Doors and People Test(Baddeley, Emslie, and Nimmo-Smith 1994); Executive function (EF), using the Trail Making Test alternating switch-cost index(Reitan 1958) and Information processing speed (IPS), using median reaction time for accurate responses on a visual choice reaction task.

Standard structural and diffusion tensor MRI analysis

Standard protocols were used for the acquisition of high resolution T1, gradient-echo (T2*) and DTI. MRI Data was obtained in a Phillips Intera 3.0 Tesla MRI scanner, using an 8-array head coil, and sensitivity encoding (SENSE) with an under sampling factor of 2. For each participant, diffusion-weighted volumes with gradients applied in 16 non-collinear directions were collected in each of four DTI runs, resulting in a total of 64 directions. The following parameters were used: 73 contiguous slices, slice thickness=2mm, field of view 224mm, matrix 128×128 (voxel size=1.75×1.75×2mm), b value=1000 and four images with no diffusion weighting (b=0s/mm2). Additionally, each patient underwent standard high-resolution T1 and gradient-echo (T2*) imaging, which were examined by a neurologist to classify the presence of microbleeds in the patient group. 25 patients had white matter microbleeds (MB+ve group, 19 males, mean age ± SD: 37.36 ± 1.6 years). The remaining 45 patients had no microbleeds (MB-ve group, 32 males, mean age ± SD: 34.1 ± 11.37 years). In the absence of pathological confirmation of TAI, we reasoned that presence of microbleeds suggests a high-likelihood of underlying TAI.

For analysis, diffusion weighted images were registered to the b = 0 image by affine transformations to minimize distortion due to motion and eddy currents and then brain-extracted using Brain Extraction Tool from the FMRIB Software Library image processing toolbox (Smith 2002, Smith et al. 2004, Woolrich et al. 2009). Fractional anisotropy, mode anisotropy and mean diffusivity maps were generated using the Diffusion Toolbox, as well as images for each of the eigenvalues (λ1, λ2 and λ3) representing the magnitude of diffusion in the three principal directions.(Ennis

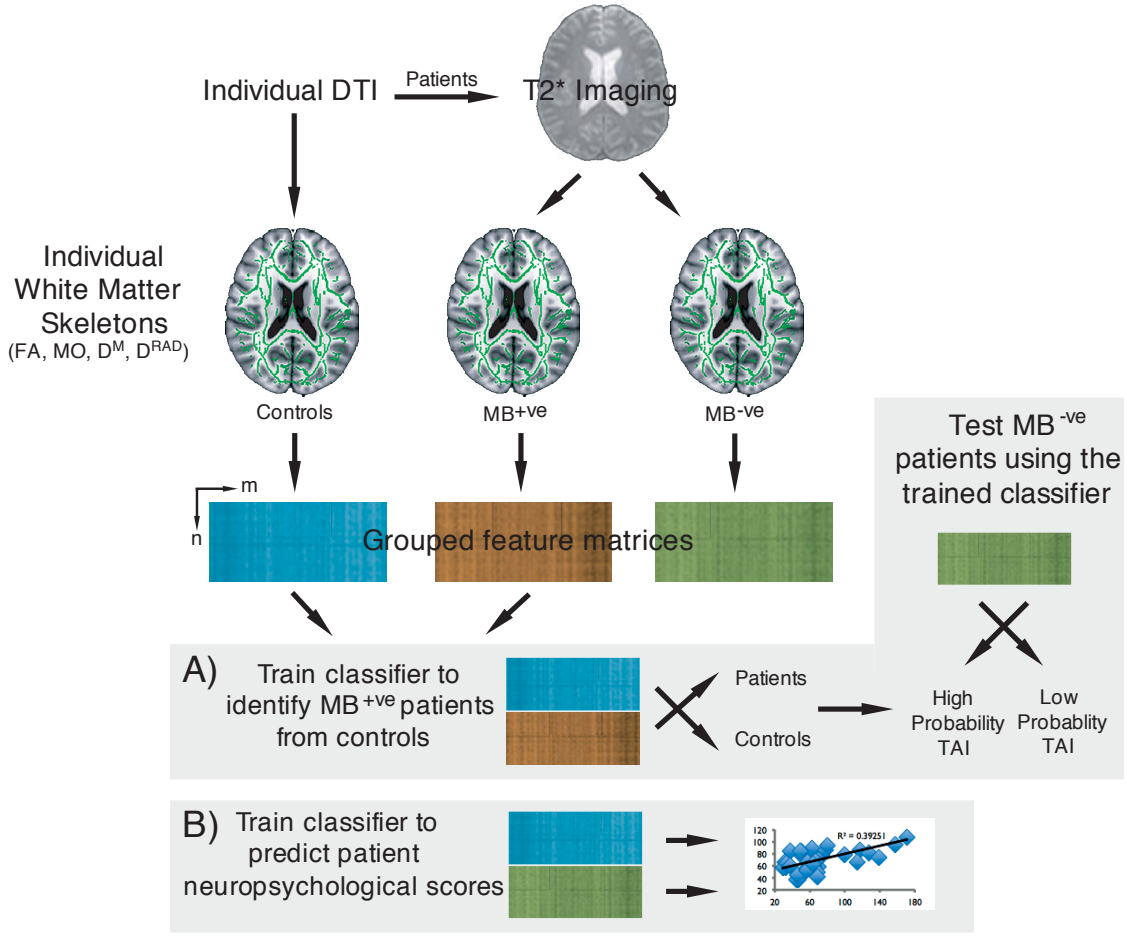

Figure 3.1 | Methods Overview. TBI patients underwent assessment using T2* (Gradient echo) imaging to determine the presence of microbleeds, a surrogate marker of traumatic axonal injury (TAI). A) Microbleed positive patients (MB+ve) and age matched controls were used to train a support vector machine classifier to detect the presence of TAI using diffusion tensor imaging (DTI) data. This classifier was then applied to microbleed negative patients (MB-ve) to generate predictions of high and low likelihood of TAI. B) All TBI patients with complete neuropsychological assessments were used to train a support vector machine regression model to predict scores on indices of information processing speed, executive function and associative memory.

and Kindlmann 2005, Behrens et al. 2003) Radial (D^{RAD}) diffusivity images were then derived from the eigenvalues ($D^{RAD}=\lambda 2+\lambda 3/2$). Further processing of these images was performed using the pre-processing stages of Tract-Based Spatial Statistics (Smith et al. 2006). First, FA images were created by fitting a tensor model to the raw diffusion data using the FMRIB Diffusion Toolbox, and then brain-extracted using the FMRIB brain extraction tool (Smith 2002). All subjects' FA data were then aligned into a common space using the FMRIB nonlinear registration tool, which uses a b-spline representation of the registration warp field (Andersson, Jenkinson, and Smith 2007, Rueckert et al. 1999). Next, the mean FA image was created and thinned

to create a mean FA skeleton that represents the centers of all tracts common to the group. Each subject's aligned FA data was then projected onto this skeleton and the resulting data fed into multivariate pattern analysis. FA describes the restriction of water movement within each voxel. Low FA and high DM and D^{RAD} suggest greater freedom of water diffusivity, which is likely to be associated with greater white matter damage (Basser and Pierpaoli 1998, Rugg-Gunn et al. 2001). MO describes the geometric properties of anisotropy, for example the extent to which free movement of water is planar (negative values) or linear (positive values). This measure may be of interest particularly around crossing white matter fibers (Ennis and Kindlmann 2005). Non-parametric permutation-based statistics were employed to explore differences in FA between patients and controls, using FMRIB's randomize with 5,000 unique permutations (Smith 2002). Multiple comparison correction was performed using threshold-free cluster enhancement and thresholded at $p<0.05$ for presentation.

Multivariate analysis using Support Vector Machines (SVMs) [Figure 3.1]

Support vector machines (SVMs) applied to MRI data represent a supervised classification technique that maps individual examples of a dataset to a specific point in n-dimensional space, where n is equal to the number of voxels within the MR image, and the absolute value within each voxel defines the position of the example along each dimension. Therefore, each training sample occupies a unique position within n-dimensional space (Cortes 1995). The SVM employs a maximum margin classification algorithm designed to derive the optimal separation between two classes of data by identification of the "hyper plane" which crosses n–dimensional space to separate the training dataset into two pre-defined labels, with error minimized to a pre-defined cost parameter (c). Each sample within the training dataset is refered to as a vector. The support vectors are defined as the samples that are critical to the positioning of the hyper plane inside n-dimensional feature space. Parameter values for SVMs in both the classification and regression problems were computed using a

simple grid-search parameter selection technique, which tested all possible values of c to minimize error and provide the best prediction accuracy possible (Cortes 1995).

Support vector classification

I used an SVM trained on voxelwise measures of structural integrity within the white matter skeletons of patients with microbleed evidence of TAI and a group of matched controls. Once trained, the classification of unseen data, i.e. patients with no surrogate markers of DAI, can be estimated by projecting the new data into hyperspace. The classification is then performed by relating the position of the new data to the DAIvsControl hyper plane. In this way we classified microbleed negative TBI patients previously unseen by the classifier into two groups; patients who had white matter more typical of TAI (defined in the MB+ve) and those that did not. [Figure 3.1A]. Support vector classification was performed using the probabilistic formulation described by Platt implemented by the libSVM classification library (Platt 1999, Chang and Lin 2011).

Support vector regression

Support vector machines can also be used as a regression tool to estimate the value of specific continuous labels such as neuropsychological test scores (Vapnik 2000). I used this method to predict associative memory (AM), examined using the Immediate recall measure of the People Test from the Doors and People Test; executive function (EF), examined using the Trail Making Test alternating switch-cost index and information processing speed (RT), examined from the median reaction time to a simple computerized visual choice reaction task (Baddeley, Emslie, and Nimmo-Smith 1994, Reitan 1958) Support vector regression as described by Vapnik was performed using libSVM classification library (Vapnik 2000).

Analysis of white matter integrity using regions of interest

I compared the multivariate classification approaches with simpler univariate and multivariate approaches using a logistic regression model trained with either: a) global mean diffusion estimates, b) mean values from individual tracts, or c) a multivariate logistic regression model, where mean values for tracts were first selected because they were shown to produce a statistically robust classification using uniariate logistic regression of each tract individually [Figure 3.3]. I also used a univariate approach (linear regression) to assess whether individual white matter tracts could predict the three neuropsychological variables. In all cases the procedure was identical to the multivariate case except with region of interest DTI measurement rather than voxelwise input.

Discriminant weights of white matter tracts

The linear kernel used by the SVMs trained in this study allow direct extraction of the 'weight vector', which has the same number of dimensions as the input feature vector (in this case, the number of voxels in the white matter skeleton) and can be thought of as a visual representation of the separating hyperplane. In terms of the present analysis, this describes the relative importance of each individual voxel in the white matter skeleton for prediction in each classification problem. The weight vector was thresholded >30% of the maximum discrimination weight as has been described in previous studies in order to eliminate noise components within the weight vector and highlight the most discriminating regions of the white matter skeleton (Mourao-Miranda et al. 2005, Ecker, Marquand, et al. 2010, Ecker, Rocha-Rego, et al. 2010). For analysis using TBSS skeletons, The weight vector was then subsampled using the JHU tractography atlas (Mori and van Zijl 2007). This allowed the contribution of specific white matter tracts to be calculated.

Cross-validation and permutation testing

The performance of each classifier was determined by using K-means cross validation. This method allows for robust cross validation by dividing samples into K sets and repeatedly generating classifiers using K-1 sets, which are tested against the remaining sample of K. Prediction error of the model is obtained by combination of K estimates of prediction error, for our analysis, K was defined as the number of training samples in each individual classifier in order to maximize cross-validation using the available training dataset (Efron 1993). Finally, each classifier was permuted 500 times without replacement, each time randomly assigning group labels to each feature vector, the number of permuted classifiers, which showed accuracy greater than the correct label assignment divided by 500 provided a probability value for the performance of each classifier differing from chance (Good 2005).

Results

Evidence of traumatic axonal injury in the patient group

Microbleeds are a marker of underlying TAI. Therefore, we expected the voxelwise analysis of FA in TBI patients to show evidence of abnormal DTI. Previous work has shown that FA is reduced in groups of patients with microbleeds (Kinnunen et al. 2011) and, as expected, our TBI group showed widespread significant reductions in FA across most of the white matter. In keeping with previous work, peaks of statistical difference between the groups were seen in the corticospinal tracts, forceps major, left Inferior fronto-occipital fasciculus, uncinate fasciculus, anterior thalamic radiation, and cingulum bundle [Appendix 3.3]. These results suggest that structural damage to white matter connections partially disconnects brain networks, in particular affecting long-range connections.

Training the classifier to identify traumatic axonal injury (TAI)

Using the multivariate approach, high accuracy (>80%) was achieved for classifiers trained on FA, MO, D^{M}, and D^{RAD} [Table 3.1A]. The most accurate classifier (94%, $p<0.002$) used FA [Figure 3.2A]. The presence of focal contusions is potentially a confounding factor; however, similar performance was achieved when only MB+ve patients without cortical contusions were used [Appendix 3.2], suggesting cortical contusion was not a major determinant of prediction accuracy.

Identifying diagnostically important white matter damage.

I next calculated the contribution of distinct white matter tracts to each multivariate classification. Measures of FA and MO were generally lower in patients than controls, whereas D^{M} and D^{RAD} were higher in patients [Figure 3.2B]. Our results suggest that the pattern of changes accompanying white matter injury after TBI is complex. For example, an increase in D^{M} and D^{RAD} within parts of the cingulum and some thalamic

N=50		Performance	Sensitivity	Specificity	P
A) SVM – Support Vector Machine	**FA**	94.0%	92.3%	95.8%	<0.002
	MO	82.0%	80.7%	83.3%	<0.002
	D^M	84.0%	79.3%	90.5%	<0.002
	D^{RAD}	82.0%	78.6%	86.4%	<0.002
B) LR – Multivariate Logistic Regression	**FA**	86.0%	84.0%	88.0%	<0.002
	MO	66.0%	60.0%	76.0%	<0.002
	D^M	68.0%	68.0%	64.0%	<0.002
	D^{RAD}	66.0%	64.0%	68.0%	<0.002

Table 3.1 | Detecting the presence of traumatic axonal injury (TAI) following traumatic brain injury. Classifiers were trained to separate MB+ve Patients and age matched controls using measures of fractional anisotropy (FA), mode anisotropy (MO), mean diffusivity (D^M) and radial diffusivity (D^{RAD}). Significance of classifiers is determined by permutation testing (See supplementary methods). SVM – Support Vector Machine trained on full voxelwise measures of diffusion. LR –Multivariate logistic regression trained using recursive feature selection of mean diffusion within white matter ROIS (See materials and methods)

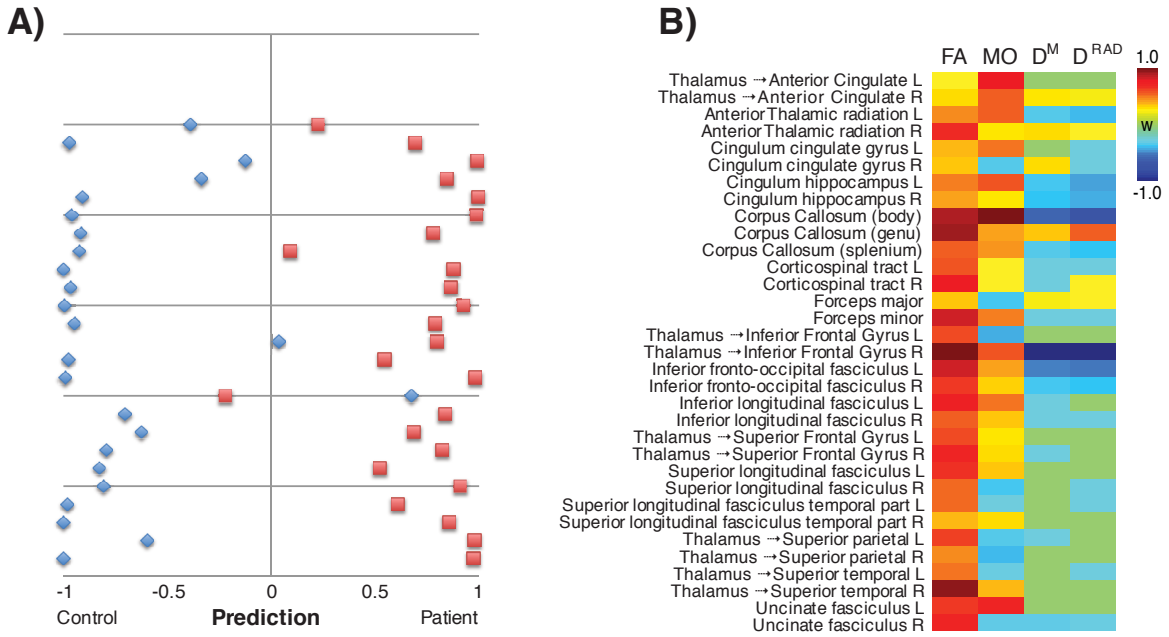

Figure 3.2 | Detecting the presence of traumatic axonal injury (TAI) using support vector machines. Classifiers were trained to identify patients with clear indication of TAI (MB+ve) from controls using four different diffusion metrics; fractional anisotropy (FA), mode anisotropy (MO), mean diffusivity (D^M) and radial diffusivity (D^{RAD}). A) The best diagnostic performance, (92% sensitivity, 96% specificity) was achieved using classifiers trained with DRAD (Blue=Controls, Red=Patients). B) Normalized contribution of specific white matter tracts to the classification. Hotter colors (closer to 1) demonstrate tracts where higher diffusion measures predict controls; Cooler colors (closer to -1) demonstrate tracts where higher diffusion measures predict patients. Left (L) and right (R).

N=26	Likely TAI	Unlikely TAI
FA	46.2%	53.8%
MO	61.5%	38.5%
D^M	69.2%	30.8%
D^{RAD}	65.4%	34.6%

Table 3.2 | Classification of traumatic axonal injury (TAI) in microbleed negative (MB-ve) patients. Classifiers trained on MB+ve patients were applied to the MB-ve contusion free patients. The output of this classifier separates the MB-ve group into two groups of likely or unlikely TAI. Fractional anisotropy (FA), mode anisotropy (MO), mean diffusivity (D^M) and radial diffusivity (D^{RAD})

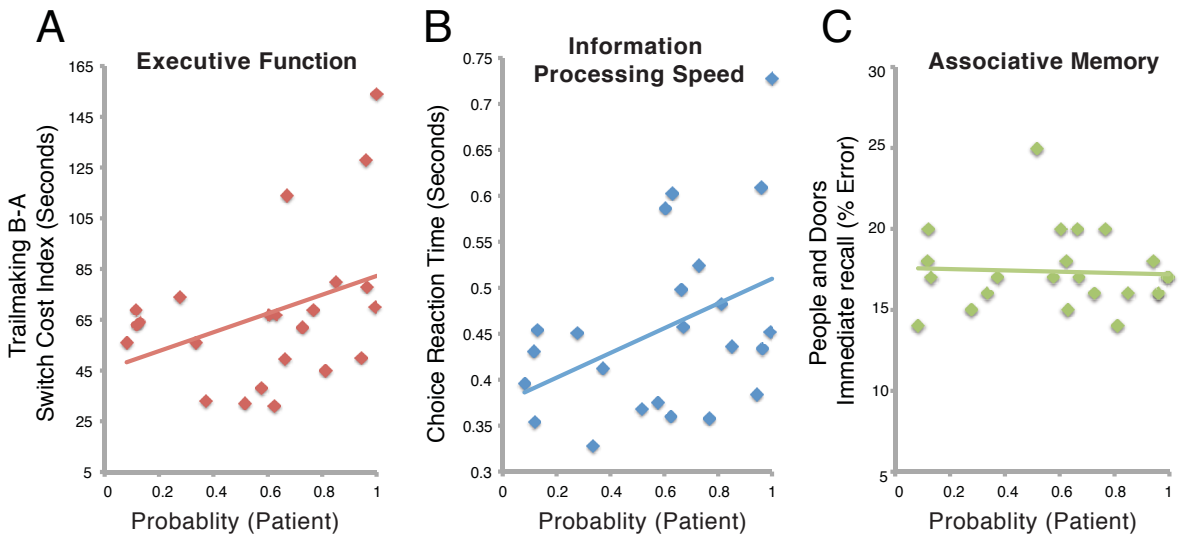

Figure 3.3 | The relationship between the probability of traumatic axonal injury in the microbleed negative group and cognitive function. Correlation plots showing the probability of being classified as having a high likelihood of TAI in the MB-ve group, based on classifiers trained with measures of Radial Diffusivity (D^{RAD}), and indices of A) executive function measured by the trailmaking B-A Switch cost index, B) Information processing speed, measured by reaction time on the Choice Reaction Time task and reaction time and C) associative memory, measured by immediate recall error of the People and Doors Task.

projections were particularly important in distinguishing between patients and controls. Multivariate approaches integrate this complexity into a single diagnostic decision.

Identifying likely traumatic axonal injury (TAI) in a group of patients without evidence of white matter injury on conventional imaging

Classifiers trained on data from the MB+ve patients were applied to microbleed negative patients (MB-ve). This group presents a diagnostic challenge, as they have no clear evidence of TAI on conventional imaging, yet frequently have persistent neurological complaints. Classifiers identified between 46.2-65.4 % of patients as having likely TAI [Table 3.2], with similar results demonstrated when classifiers trained on contusion free MB+ve patients were used [Appendix 3.3].

To investigate the clinical significance of these classifications, we tested how classification of MB-ve patients related to cognitive function [Figure 3.3]. For D^{RAD} classifiers, the trail-making switch cost (a measure of executive function - EF) was positively correlated with the likelihood of TAI ($r=0.377$, $p<0.05$). Using FA, D^{M} and D^{RAD} classifiers, a greater likelihood of TAI was positively correlated with median choice reaction time (a measure of information processing speed – IPS), ($r=0.352$, 0.372 and 0.415 respectively. $p<0.05$). Performance on the Doors and People test, a measure of associative memory (AM) was not significantly correlated with prediction confidence for any of the classifiers [Appendix 3.4]. However, post-hoc correlations, suggest that whist measures of AM, are indepdendent of both EF, and IPS ($r=0.01$ ns and $r=0.15$ ns, respectively), measures of IPS and EF, are strongly correlated ($r=0.65$, $p<0.001$), suggesting that a common psychological mechanism between IPS and EF (see discussion).

Comparing voxel-wise classification with univariate and other

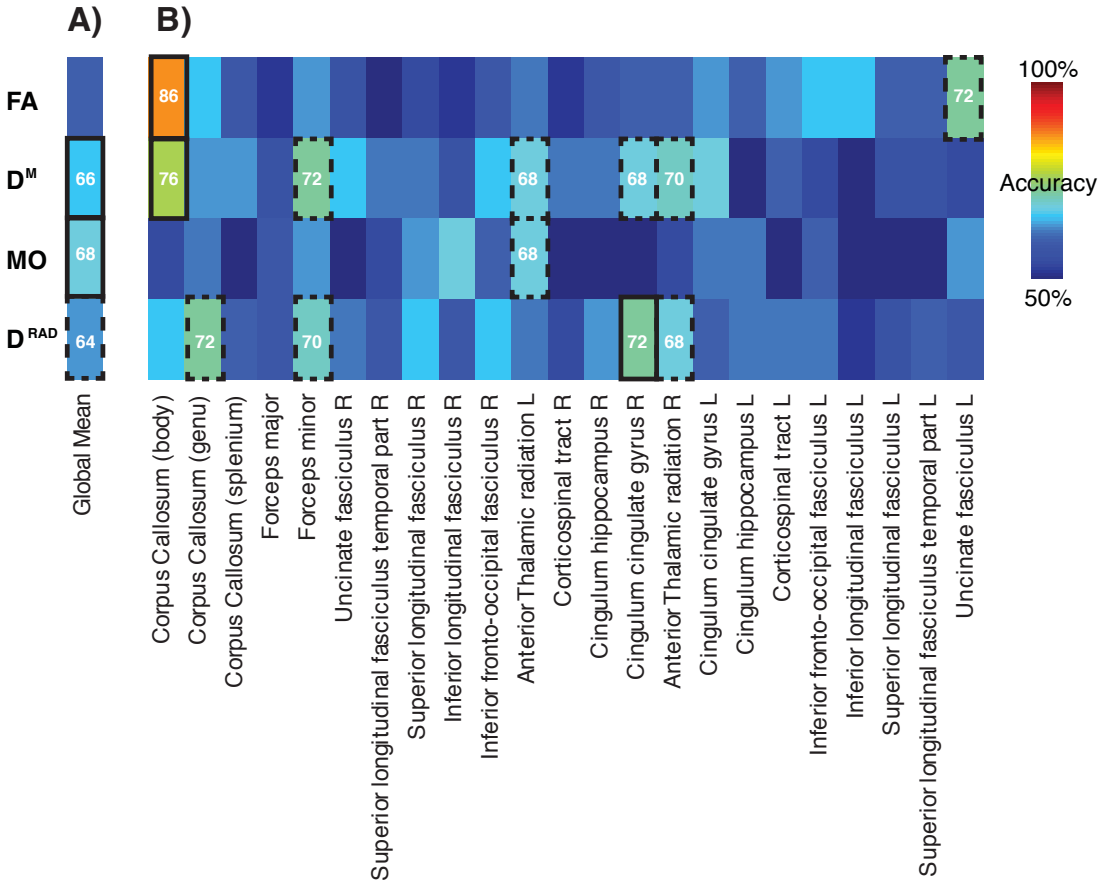

Figure 3.4 | Detecting the presence of traumatic axonal injury (TAI) using logistic regression. Classifiers were trained to identify patients with clear indication of TAI (MB+ve) from controls using mean fractional anisotropy (FA), mode anisotropy (MO), mean diffusivity (D^M) and radial diffusivity (D^{RAD}) within a range of ROIs selected using the JHU tractography atlas, as well as using mean values from the whole skeleton. Hotter colors demonstrate higher accuracy, cooler colors demonstrate performance closer to chance. Bold outlines $p<0.01$, Dashed outlines $p<0.05$ bonferroni corrected.

multivariate approaches

To compare the voxel-wise multivariate approach to simpler multivariate and univariate approaches we trained logistic regression classifiers to distinguish between MB+ve patients and controls. A single mean value for each diffusion metric was calculated from the white matter skeleton, providing an average of white matter integrity in each patient [Figure 3.4A]. With this approach the most accurate classifier used global mean MO (68% $p<0.01$); D^M and D^{RAD} performed at a rate of 66% ($p<0.01$) and 64% ($p<0.05$) respectively. Classifiers trained on global mean FA performed at a rate of 60%, and were close to significant according to permutation testing ($p=0.051$). Classifiers

Test n=35	Diffusion Estimate	r	p
IPS - Median CRT Response time	**FA**	0.395*	<0.05
	MO	0.346*	<0.05
	D^{MEAN}	0.515**	<0.01
	D^{RAD}	0.530**	<0.01
EF - Trail making B	**FA**	0.374*	<0.05
	MO	0.417*	<0.05
	D^{MEAN}	0.560***	<0.001
	D^{RAD}	0.627***	<0.001

Table 3.3 | Predicting cognitive function following traumatic brain injury using support vector regression. Support vector regression was used to predict information processing speed (IPS), executive function (EF) and associative memory (AM). Fractional anisotropy (FA), mode anisotropy (MO), mean diffusivity (D^{M}) and radial diffusivity (D^{RAD}) in 35 patients without cortical contusions. (Pearson's product-moment correlation coefficient (1-tailed), *p<0.05 3SF, ** p<0.01 3SF, ** p<0.001 3SF), results < 0.01 pass Bonferroni correction for multiple comparisions.

trained on certain specific tracts performed better e.g. (86% p<0.01) using mean FA within the body of the corpus callosum [Figure 3.4B]. However, univariate classification accuracy was generally low (mean performance 59.90%) and this technique involves the assessment of multiple tracts separately. In addition, a multivariate logistic regression approach was used that included those regions that performed well at univariate classification. The logistic regression classifiers performed between 8-16% worse than the equivalent support vector machine classifiers [Table 3.1B].

Predicting cognitive function following traumatic brain injury

To test whether multivariate analysis of DTI data could directly predict cognitive function in individual patients [Table 3.3], we trained four different support vector

machines for regression using FA, MO, D^{M} and D^{RAD} to predict neuropsychological test scores. In addition, we repeated the analysis on a subgroup of 35 patients free of focal contusion (25 males, mean age ± SD: 34.1 ± 10.65 years). Correlation coefficients were calculated between the actual neuropsychological test scores and the value predicted by SVM using a leave-one-out approach. This allowed us to assess whether our models generalized to the prediction of performance in new patients.

Executive function (EF)

White matter structure could be used to significantly predict individual patients' executive function. [Table 3.3]. The relationship between actual and predicted score was strongest for D^{RAD} (r=0.627 p<0.01, bonferroni corrected.) [Figure 3.5A], but was present for all four measures. Important contributions to the prediction were assessed using the SVM weight vector, were made by white matter structure within the corpus callosum; cingulum bundle; the left corticospinal tract; right superior longitudinal

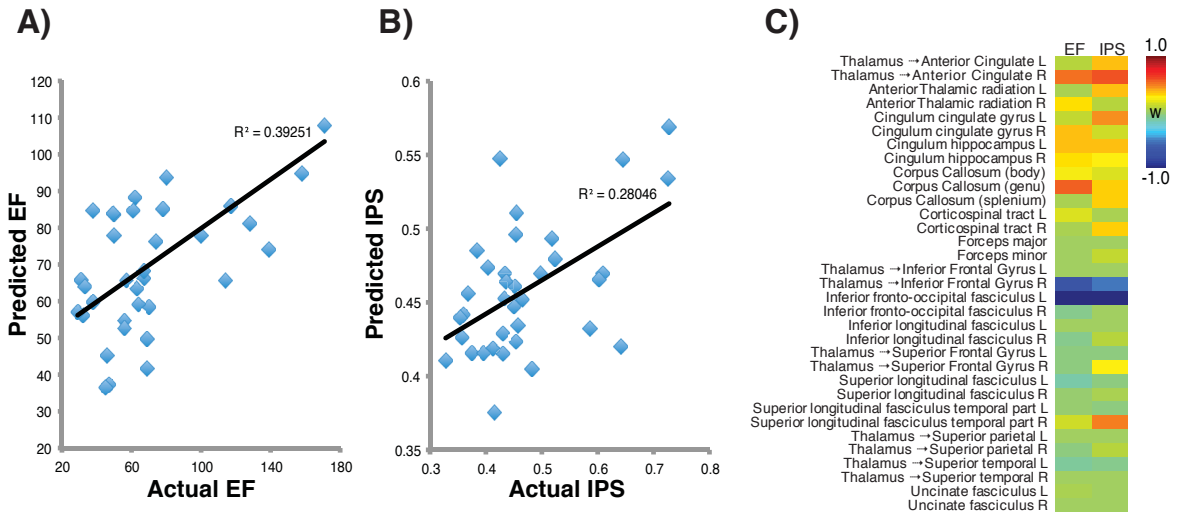

Figure 3.5 | Predicting cognitive function using support vector regression.

Support vector regression machines were trained to predict reaction time (IPS), executive function (EF) and associative memory (AM). Significant positive correlations between the true neuropsychological index value, and the predicted value found SVM regression of IPS and EF for all diffusion metrics. The best levels of prediction for RT (A) and EF (B) were detected using estimates of D^{RAD}. C) The contribution of specific white matter tracts to the classifier prediction. Hotter colors demonstrate greater relative importance of D^{RAD} measures in specific tracts when predicting neuropsychological outcome. Left (L) and right (R). Correlations signifcant p<0.01 (Bonferroni corrected)

fasciculus; right inferior-fronto-occipital fasciculus and right lateralized thalamic projections to the inferior frontal gyrus [Figure 3.5C, 1st Column]. Qualitatively similar results were obtained when only patients without cortical contusions were included, demonstrating that prediction of executive function based only on white matter structure, is robust to the presence of cortical contusions [Appendix 3.5].

For EF, the multivariate approach outperformed univariate linear regression models when tested in the contusion free TBI patients. The best accuracy (bonforoni corrected) using mean global diffusion metrics was achieved using mean MO ($r=0.53$, $p<0.01$) [Figure 3.6A, Left]. Using individual tracts the best performance used mean D^M within the left cinglulum bundle ($r=0.57$, $p<0.01$, correcting for multiple comparisons) [Figure 3.6A, Right]. Good performance was also observed in the body of the corpus callosum ($r=0.54$, $p<0.01$) and the left anterior thalamic radiation ($r=0.57$, $p<0.01$).

Information processing speed

Similarly we found that measures of white matter structure could be used to predict individual patients' information processing speed using the multivariate approach [Table 3.3] (bonferroni corrected) The relationship was strongest for D^{RAD} ($r=0.530$, $p<0.01$) but was present for all measures. Particularly important contributions to the predictions were made by white matter within the cingulum bundle; corticospinal tracts; the corpus callosum; the left inferior fronto-occipital fasciculus and the right superior-longitudinal fasciculi [Figure 3.5C 2nd Column]. When all patients were included in the analysis, including those with cortical contusions, the correlation remained significant between predicted and actual values based on FA and D^{RAD} [Appendix 3.5].

In contrast to our other analyses, the univariate approach to predicting information processing performed similarly to the multivariate one. The best accuracy using mean global diffusion metrics was for MO ($r=0.55$, $p<0.01$) [Figure 3.6A, Left]. Analysis using

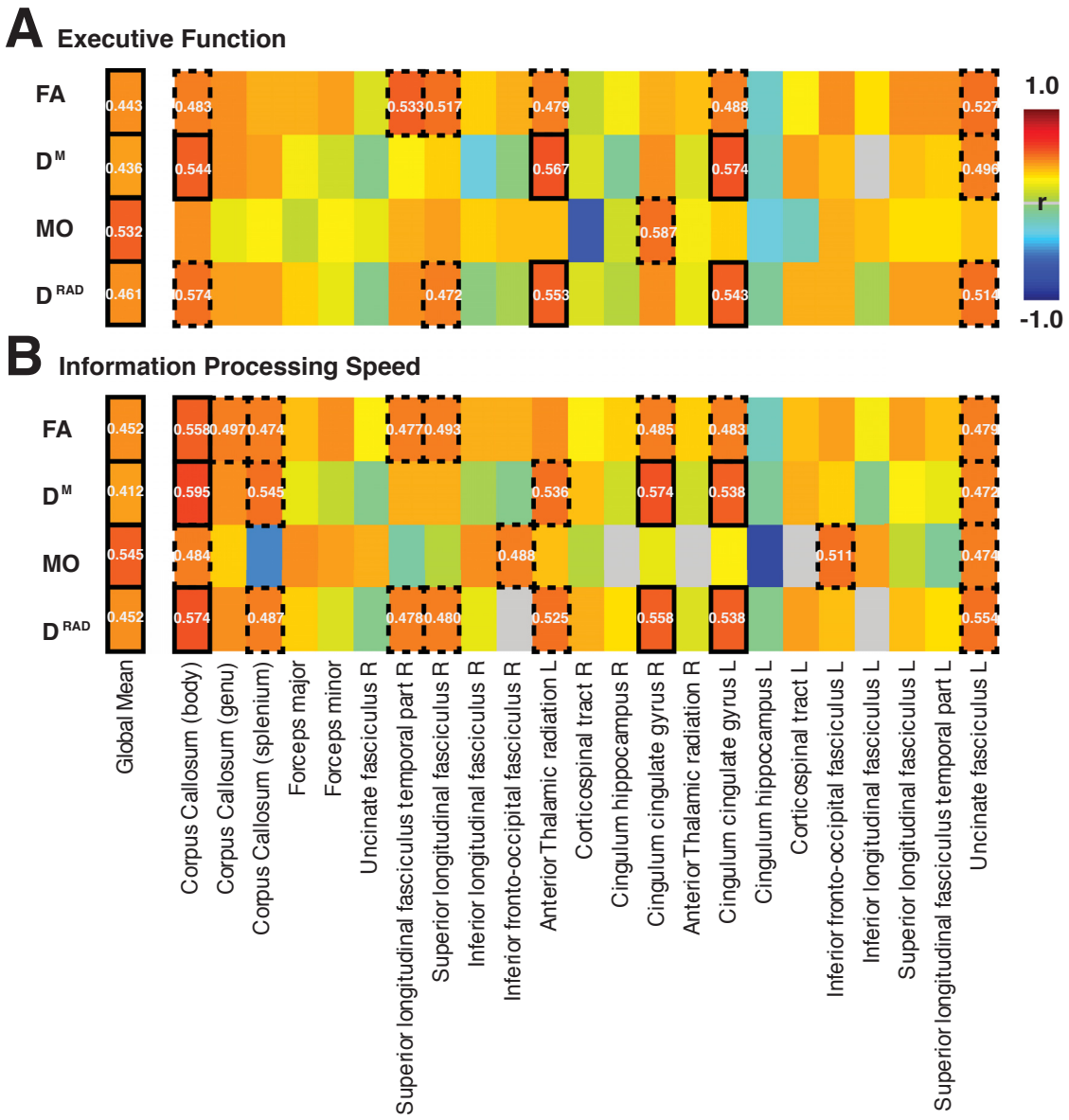

Figure 3.6 | Predicting cognitive function using linear regression.

Linear models were fit to A) Information processing speed and B) executive function and mean fractional anisotropy (FA), mode anisotropy (MO), mean diffusivity (D^M) and radial diffusivity (D^{RAD}) within a range of ROIs selected using the JHU tractography atlas, as well as the means from the skeleton (left of figure). Pearson's product-moment correlation coefficient (1-tailed), bold outlines $p<0.01$, dashed outlines $p<0.05$ bonferroni corrected.

smaller ROIs defined by individual JHU tracts was also performed [Figure 3.6A, Right]. The best performing predictive model used values for mean D^M within the Left and Right portion of the cingulum bundle (r=0.57, 0.53 p<0.01), respectively.

Associative memory (AM)

Both multivariate and univariate linear regression models failed to accurately predict associative memory performance as measured by immediate recall on the people task using any of the estimates of white matter integrity.

Discussion

Traumatic brain injury (TBI) often results in significant and persistent cognitive impairment (Whitnall et al. 2006, Scheid et al. 2006). The pathophysiological basis for this is often uncertain. Focal injuries are usually easily identified using conventional CT and MR imaging. However, these injuries often do not well explain clinical outcome (Bigler 2001, Levine et al. 2005, Niogi, Mukherjee, Ghajar, Johnson, Kolster, Lee, et al. 2008, Lee et al. 2008). In contrast, traumatic axonal injury (TAI) appears to be a key determinant of clinical outcome, which can be missed by conventional imaging (Adams 1982, Medana and Esiri 2003). Animal studies show that TAI can be widespread even when conventional MRI appears normal (MacDonald, Dikranian, Bayly, et al. 2007, MacDonald, Dikranian, Song, et al. 2007, Li et al. 2011). Here, we demonstrate how machine learning can be used to augment diagnosis of TAI in individual patients. First, we show how a support vector machine classifier can be trained to identify complex patterns of white matter damage produced by TBI in a group with evidence of TAI from conventional MRI imaging. Secondly, I show how this trained classifier can be used to identify patients with a high likelihood of TAI in a group without evidence of TAI from conventional imaging. Finally, we demonstrate that support vector machines can be used to predict cognitive impairment in individual patients, based only on the pattern of white matter damage.

Currently the most widely used approach to diagnosing TAI is to identify the presence of microbleeds on gradient echo or susceptibility weighted magnetic resonance imaging (Scheid et al. 2006). In areas where TAI has produced petechial microhaemorrhage, this technique is highly sensitive. However, TAI is not necessarily accompanied by petechial hemorrhage, and identifying microbleeds does not provide a quantitative assessment of damage. DTI gives important additional diagnostic information, by providing a quantitative measure of white matter structural integrity that is sensitive

to non-hemorrhagic TAI (MacDonald, Dikranian, Bayly, et al. 2007).

Much previous work has investigated white matter abnormalities in pre-specified regions of interest (Kraus et al. 2007, Niogi, Mukherjee, Ghajar, Johnson, Kolster, Sarkar, et al. 2008, Niogi, Mukherjee, Ghajar, Johnson, Kolster, Lee, et al. 2008, Kennedy et al. 2009). This approach is sensitive at detecting abnormalities within the regions assessed, but is limited to small regions of the total white matter and it is unclear a priori which regions should be assessede.g. (Niogi, Mukherjee, Ghajar, Johnson, Kolster, Sarkar, et al. 2008). An alternative is to adopt a 'whole brain' approach, where all voxels within white matter tracts are simultaneously assessed. Most studies of this type employ univariate statistics (i.e. each point in an image is analyzed separately) and report the results from groups of subjects (Kinnunen et al. 2011). When the goal is diagnostic, this univariate approach fails to integrate information from different spatial locations to detect complex discriminating patterns of white-matter damage in the individual. The machine learning approach we report provides a sensitive way of incorporating information from all major white matter tracts into a single diagnostic decision and can be used to predict the likelihood of TAI in individual patients.

I go on to demonstrate using multivariate techniques that the pattern of white matter damage in an individual can be used to make predictions about executive function and information processing abilities after TBI in individual patients. Relationships between DTI and both information processing speed and executive function were strongest when based on measures of radial diffusivity, which is thought to be a surrogate marker for axonal demyelination (Klawiter et al. 2011, Song et al. 2003, Song et al. 2002). Given that conduction speed is proportional to the degree of myelination, this relationship between D^{RAD} and information processing speed may reflect changes in myelination associated with TAI (Waxman 1980). One limitation of these predicitons is that measures of Information processing speed and executive function measured by performance on the choice reaction time task and trail making test are strongly correlated, this suggests that there may well be a common psychological mechanism

underpinning performance of each of these tests, limiting the value of their prediction in isoation. One approach which is beyond the scope of the current work to adress this problem, would be to embrace the multivariate nature of neuopsychlogical batteries and rather than focus on the results of a few isolated tests (albeit, tests that are consistently used within the TBI literature (Kinnunen 2011)), focus on composite and orthogonal measures of psychological 'factors' which could be exposed in these rich datasets using approaches such as principal component analysis or multidimensional scaling.

The voxel-wise multivariate approach outperformed both univariate and mulitvariate methods based on DTI measures averaged across regions of interest. Superior prediction of executive function performance was also achieved using the voxel-based approach. In contrast, the univariate and multivariate approaches were equivalently successful in predicting information processing speed, even when the average mean diffusivity from the whole white matter skeleton was used. This might be because information processing speed after TBI reflects functional integration across large numbers of white matter tract, and this global feature is adequately captured by an average measure of white matter damage across the whole brain. At the other extreme, certain cognitive functions appear to depend on the integrity of a small number of tracts. Previously work has shown a clear relationship between integrity of the fornix and associative memory function after TBI (Kinnunen et al. 2011). Interestingly, the multivariate model was unable to predict associative memory function, perhaps because the contribution of the very small but critical white matter tracts is small using this approach. The failure of the univariate approach in predicting associative memory may be because a fornix region of interest was not used. The relationship between fornix integrity and memory function previously observed (Kinnunen et al. 2011) was present in a healthy control group, as well as the TBI patients. Although we don't address the issue here, it is likely that our multivariate techniques could be applied to the prediction of cognitive performance in the healthy population, and future work

should investigate this.

There are however several potential limitations to our approach. Firstly, the registration of individual images into standard space must be accurate or partial volume effects can lead to highly abnormal DTI metrics. The pre-processing that we employ (TBSS) was developed specifically to minimize the impact of these problems in disease states (Smith et al. 2006).The white matter is 'skeletonized' and only the central points of tracts studied, greatly reducing the risk of partial volume effects. The accuracy of registration was carefully checked in all cases; therefore this is unlikely to a major cause of error in our analyses. Secondly, It is important to note that a small proportion of the patient population described by this study, were taking potentially psychoactive drugs at the time of scanning for a variety of reasons (e.g., chronic pain). This is commonly found following TBI, so the patients were a representative population. However, these drugs may affect the neuropsychological measures such as reaction time and so could be contributing noise unconnected to the DTI measurements, which if anything would make classification harder. Finally, there is a strong correlation between the different DTI measures, particularly MO and FA. Therefore, the high classification performance may reflect underlying variance shared across the different diffusion measures. In addition, DTI changes are dynamic after TBI and so our results are likely to be specific to the chronic phase (>2 months) post injury. Further work is required to apply the machine learning approach we employ to the acute and sub-acute period after injury. Finally, our analysis is cross-sectional, and therefore does not directly support the use of DTI to predict clinical outcome over time. Longitudinal prediction is an important clinical application and previous univariate work with groups of patients demonstrates that DTI provides additional information about outcome e.g. (Sidaros et al. 2008). Machine-learning approaches are likely to be a more sensitive way of improving the predictive value of DTI, particularly when making individual predictions. Future work with larger patient groups could incorporate this type of technique, and should explicitly model a large number of clinical variables that are known to be important

in explaining outcome, such as acute imaging changes, clinical measures of injury severity and measures of gray matter atrophy.

In conclusion, we provide evidence that using DTI with machine learning approaches has the potential to augment diagnosis of traumatic axonal injury in individual patients following TBI, and we demonstrate relationships between white matter damage and predictions about individual patients' cognitive impairment.

A computational model of the neural dynamics in the resting brain

4

Introduction

A key goal for cognitive neuroscience is to explain the relationship between structural connectivity and the dynamical functional activity (FC) of the brain. Functional activity is organised into intrinsic connectivity networks, which overlie regions of strong structural connectivity (Honey et al. 2009, Honey, Thivierge, and Sporns 2010, Hagmann et al. 2008, Sporns 2013, van den Heuvel and Sporns 2013). Advances in modern MRI have made the possibility of generating large-scale connectivity datasets possible. The ensemble of structural or functional brain connections can be described as a complex network, the "connectome" (Cammoun et al. 2011, Cocchi, Zalesky, and Fontenelle 2012, Fornito et al. 2012, Sporns 2013, 2011, Sporns, Tononi, and Kotter 2005, van

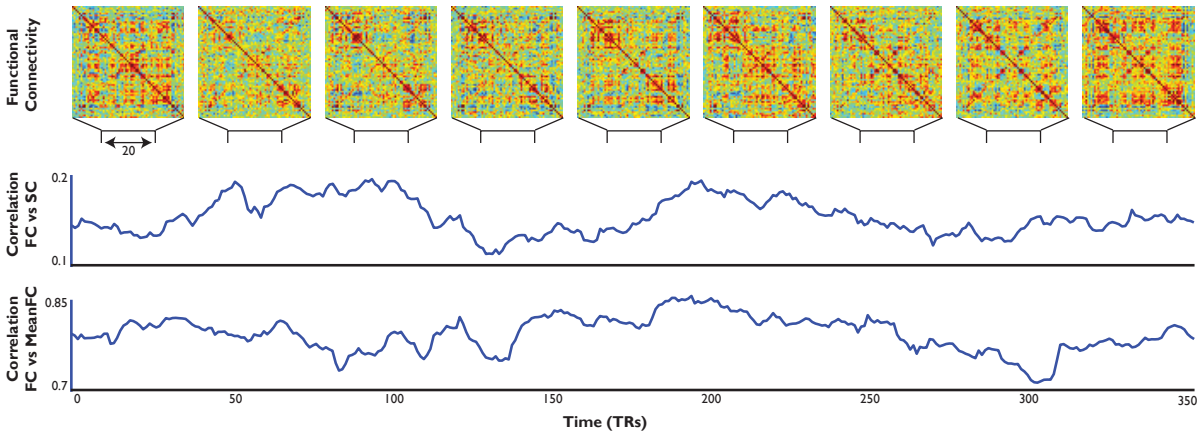

Figure 4.1 | Functional Connectivity Evolves dynamically over time. Functional connectivity of a single healthy control subject, calculated over a 20s sliding time window (Top). Compared to both static measures of Functional connectivity evaluated over the entire time-course (MeanFC), and static measures of structural connectivity (SC), dynamic measures of functional connectivity vary dramatically over time.

den Heuvel and Sporns 2011).

However, whilst structural connectivity is somewhat predictive of FC, strong correlations between regions that have no direct anatomical connectivity – often with path-length distances of 3 or greater can show strong functional connectivity (Honey et al. 2009, Honey, Thivierge, and Sporns 2010). It is also clear that whilst structural connectivity is static over short time scales (i.e., the duration of an FMRI scan), functional connectivity even at rest changes dynamically (in the order of seconds to minutes) (Hutchison, Womelsdorf, Allen, et al. 2013, Hutchison, Womelsdorf, Gati, et al. 2013, Allen et al. 2014, Handwerker et al. 2012, Zalesky et al. 2014, Smith et al. 2012) [Figure 4.1]. The emergence of such dynamic activity from a static network is an example of 'functional multiplicity' where a single network interacts in a dynamic regime that produces a wide variety of different functional interactions – moreover, measures of structural connectivity relate better to FC when FC is averaged across a large timescale or filtered to a relatively low frequency (Honey et al. 2009, Honey, Thivierge, and Sporns 2010). In light of these observations, it is clear that understanding the organisation of resting state networks, depends not only on accurately measuring structural connectivity of the brain, but also on the time-evolving interactions between individual regions of the brain – the dynamics which enable more complex states to emerge over short

timescales. (Deco, Jirsa, and McIntosh 2011, Deco and Corbetta 2011, Deco et al. 2009). Thus the development of theoretical models which relate local cortical dynamics with underlying structure are of fundamental importance in studying the relationship between macroscopic functional connectivity, structure and behaviour.

The development of macroscopic computational models provides an ideal framework for examining the dynamic features of the brain that enable complex functional interactions to emerge from the structural connectome [Figure 4.2]. Simulated time-courses from such models can be compared to those of empirical functional data by passing the model output through a haemodynamic model (Friston et al. 2000), or quantitatively analysed using tools from dynamical systems theory (Shanahan 2010b, a, Chialvo 2010, Chialvo 2004). Such models are designed to explore the dynamics over and above structure that occur in the brain (Cabral, Hughes, et al. 2011, Cabral, Kringelbach, and Deco 2014, Deco and Corbetta 2011, Deco, Jirsa, and McIntosh

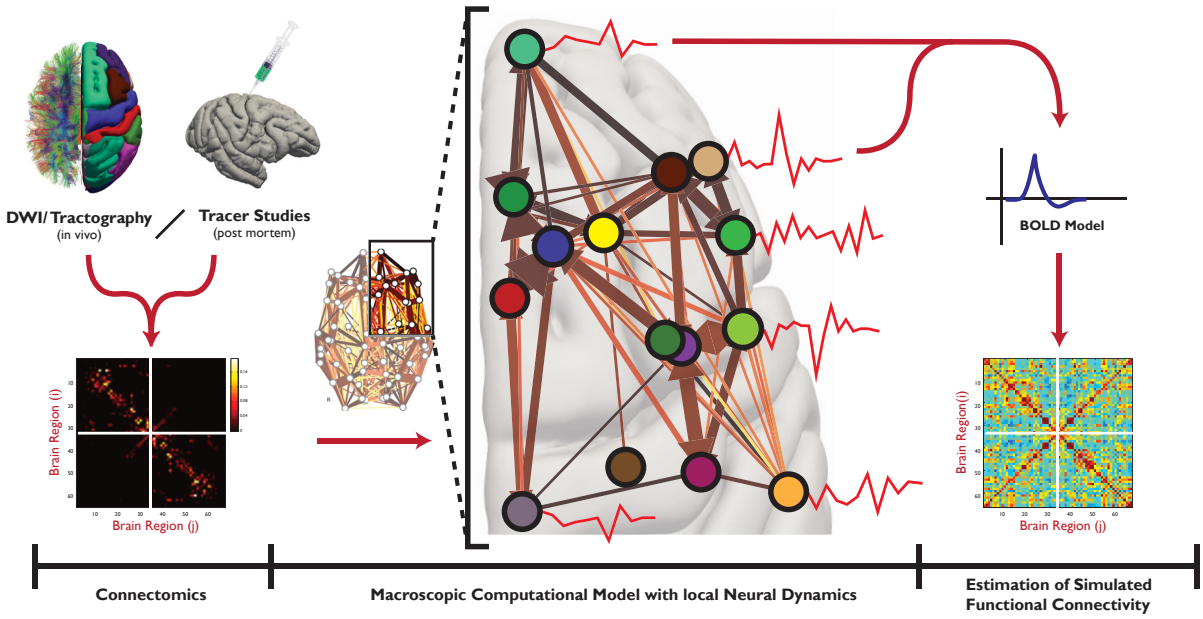

Figure 4.2 | Computational approaches to examining macroscopic neural dynamics. To examine the importance of local dynamics on shaping macroscopic measures of functional connectivity through structure of the brain, Strucutral connectivity (derived from DWI or tracer studies, Left) are projected into a computational model, which defines how long distance structural connections interact with local activity in each individual region to produce neural activity (Centre). These simulated dynamics are often compared to empirical fMRI by passing simulated time-courses though a haemodynamic model and calculating measures of functional connectivity which can then be directly compared with similar empirical datasets (Right).

2011, Messe et al. 2014). Such models exist at a range of different levels of spatial and temporal complexity: e.g. modelling connectivity between groups of specific neuronal subtypes (Deco et al. 2014, Deco and Corbetta 2011), using models of individual neurons or else mean field approximations of pools of large numbers of neurons, incorporating neuromodulators such as NMDA, AMPA and GABA (Deco et al. 2014, Deco et al. 2008), as well as exploring a range of different model parameters such as intrinsic noise, and conduction delays. A key observation that cuts across all of these models at all levels of description is that these models are validated by the overlap with resting state activity in a regime balanced between highly ordered and highly disordered activity (Alexander 2005).

Recent work has explored measures of the dynamics of computational models. One approach has focused particularly on two measures of dynamical flexibility: synchrony and Multistability (Wildie and Shanahan 2012, Shanahan 2010b, a, Tognoli and Kelso 2014, Kelso 2012, Bressler and Kelso 2001). Multistability in neural activity is not a new concept (Friston 1997) and refers to the evolution of spontaneous dynamics within the brain where the functional state of the system can endogenously move between transient 'attractor-like' states in order to reconcile "the well-known tendencies of specialized brain regions to express their autonomy (segregation) and the tendencies for those regions to work together as a synergy (integration)". As such, the level of Multistability in the system may be important for efficient integration in the brain (Tognoli and Kelso 2014, Shanahan 2010a). Computational modelling has suggested that Multistability is a property of the neural dynamics of the brain at rest (Deco et al. 2009, Cabral, Hugues, et al. 2011). Theoretical accounts suggest that increased Multistability in the brain allows more flexible dynamic interactions between regions, whereas reductions in Multistability may accompany more persistent and stable states (Shanahan 2010a).

A computational model that provides the appropriate level of abstraction to examine Multistability within complex systems is the Kuramoto Model of coupled phase

oscillators (Kuramoto 1984). Within this system each node represents an oscillator with a single intrinsic operating frequency [Figure 4.3]. The dynamics of the overall system of oscillators is then defined by the weak delayed coupling enforced between pairs of oscillators within the system, providing two free parameters in the model – the strength of connections between nodes and the scale of interaction delay between regions, potentially providing a broad range of different dynamical repertoires to emerge. Dynamic stability of the whole Kuramoto system or a subset of the nodes can then be examined using a well-defined order parameter (Shanahan 2010b). The Kuramoto order parameter represents both the overall phase of a group of oscillators, and moreover how 'phase locked' they at any point in time. The variability (standard deviation) of this measure of phase locking over time has been proposed as a description of how Multistable the system is. The mean (across time) of this phase locking is a measure of how synchronous the system is. If the system visits a wide range of different sub-states over time, Multistability will be high, and associated with a modest level of synchrony. Both highly disordered and stable states would be associated with lower Multistability and low or high synchrony respectively (Wildie and Shanahan 2012, Shanahan 2010b).

The Kuramoto model has recently been used to examine the relationship between structural connectivity and resting state dynamics in the framework of the brain, coupling within the model was defined using the strength of connectivity between 66 brain regions defined by DSI tractography (Hagmann et al. 2008). The size of the delay interactions (representing neural transmission delay), was then defined using the length of tracts between each region. In this model, Multistable dynamics were associated with the emergence of functional connectivity patterns evocative of the resting state (Cabral, Hugues, et al. 2011). One potential limiation of using a fast model of neural dynamics such as the Kuramoto model for comparisons between macroscopic measures of functional connectivity measured in the brain using techniques such as functional MRI, is that the kuramoto model operates at a timescale

significantly smaller than that of the empirical measures.

In this chapter, I introduce the Kuramoto model in detail and show how it can be used for exploring brain dynamics based on the structural connectivity of the brain (Hagmann et al. 2008). I will present a number of simulations where the model is 'tuned' by evaluating the dynamical regimes under which this model best simulates

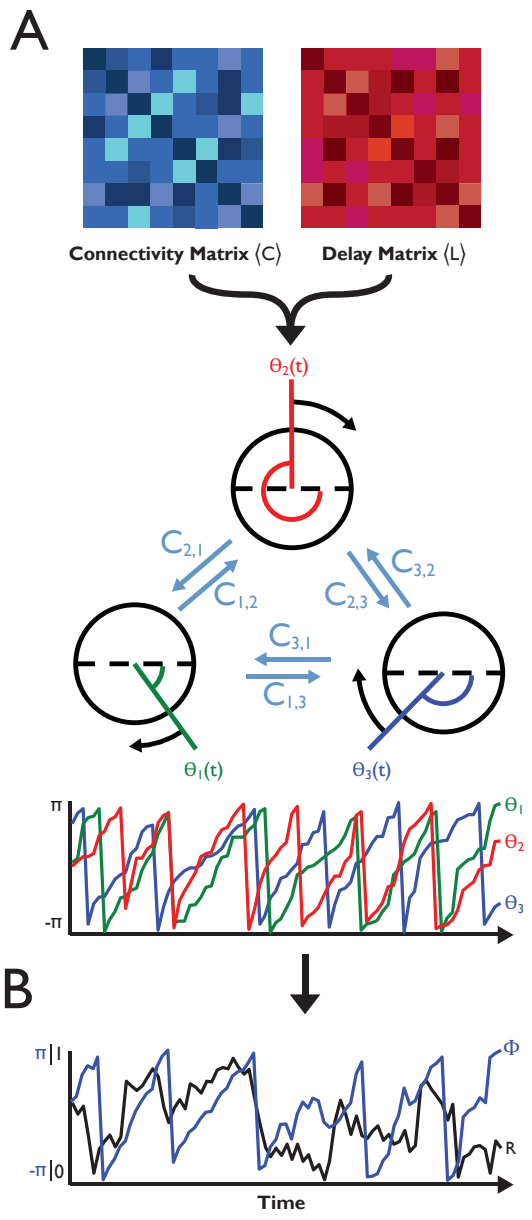

Figure 4.3 | Simulating neural activity and Multistable dynamics using the Kuramoto oscillator model. A) The Kuramoto oscillator model is built of a community of phase oscillators (nodes). The activity (or phase) of each oscillator over time is affected by the phase of each other oscillator in the model according to the weights by which they are interconnected <C>. In the connections between oscillators may be delayed in time according to a matrix of lengths <L>, which allow the model to include realistic conduction delays. <C> and <L> are provided as priors to the model and in terms of the brain represent estimates of white matter connectivity between nodes, and their lengths respectively. B) Measurements of 'phase locking' between nodes within the model can be measured using the order parameter of the simulated phase histories. The angle of this parameter (Φ) defines the overall phase vector of the community measured whilst the magnitude (R), describes the overall level of phase locking or synchrony, displayed by the community over time.

empirical resting-state cortical dynamics along two parameter dimensions (the coupling strength and delay of connections). This results in a validated model that is subsequently used in the following two chapters to explore dynamics and how they relate to some aspects of cognition and brain injury.

Methods

The Kuramoto oscillator model

Empirical Structural Connectivity

The computational simulation is based on connectivity matrices describing the strength <C> and length <D> of white matter connections between 66 cortical regions defined using tractography of diffusion spectrum imaging. These matrices, initially described by Hagmann and colleagues (Hagmann et al. 2008), have subsequently been used in Kuramoto simulations to demonstrate emergent properties of structural connectivity (Cabral, Hugues, et al. 2011). See (Hagmann et al. 2008) for a more detailed description of the methodology used to define these structural connectivity matrices.

Simulation of network activity [Figure 4.3A]

The activity of each of the 66 brain regions (which we define here as nodes) is represented in our model as the phase of a single phase oscillator over time (Breakspear, Heitmann, and Daffertshofer 2010, Acebrón et al. 2005, Cumin and Unsworth 2007, Shanahan 2010b, Cabral, Hugues, et al. 2011, Kuramoto 1984). Each node is connected to all other nodes within the system according to the empirical connectivity (see above). Phase at each node over time , is described by the dynamical Kuramoto oscillator equation (Kuramoto 1984, Acebrón et al. 2005):

$$\frac{d\theta_i}{dt} = \omega_i + \frac{1}{N+1}\sum_{j=1}^{N}(A_{i,j}(t)\cdot(k\,C_{i,j}))\sin(\theta_{(j)}(t-(\tau\,D_{i,j}))-\theta_i(t)) \quad N = 66$$

The natural frequency (w) defines the phase change of an un-coupled node per time-step. The connectivity matrix <C> is determined by the empirical strength of white matter connections. The distance matrix <D>, determined by the empirical length of

connections between regions, imposes time delays on phase interactions between nodes. This is analogous to simulation of a delay caused by neural conduction between regions of the brain. In addition to the constraints imposed by the connectivity matrix, an additional time-dependent constraint between nodes may be imposed by modulation of the activity matrix <A>(t). Finally, two scaling factors were defined: k, scaling the connectivity and τ, scaling the delay matrices respectively. The behavior of the Kuramoto model with respect to global Multistability and synchrony as these two parameters are altered has been explored previously (Cabral, Hugues, et al. 2011, Shanahan 2010b). Using a grid-search approach, we set the values of these parameters

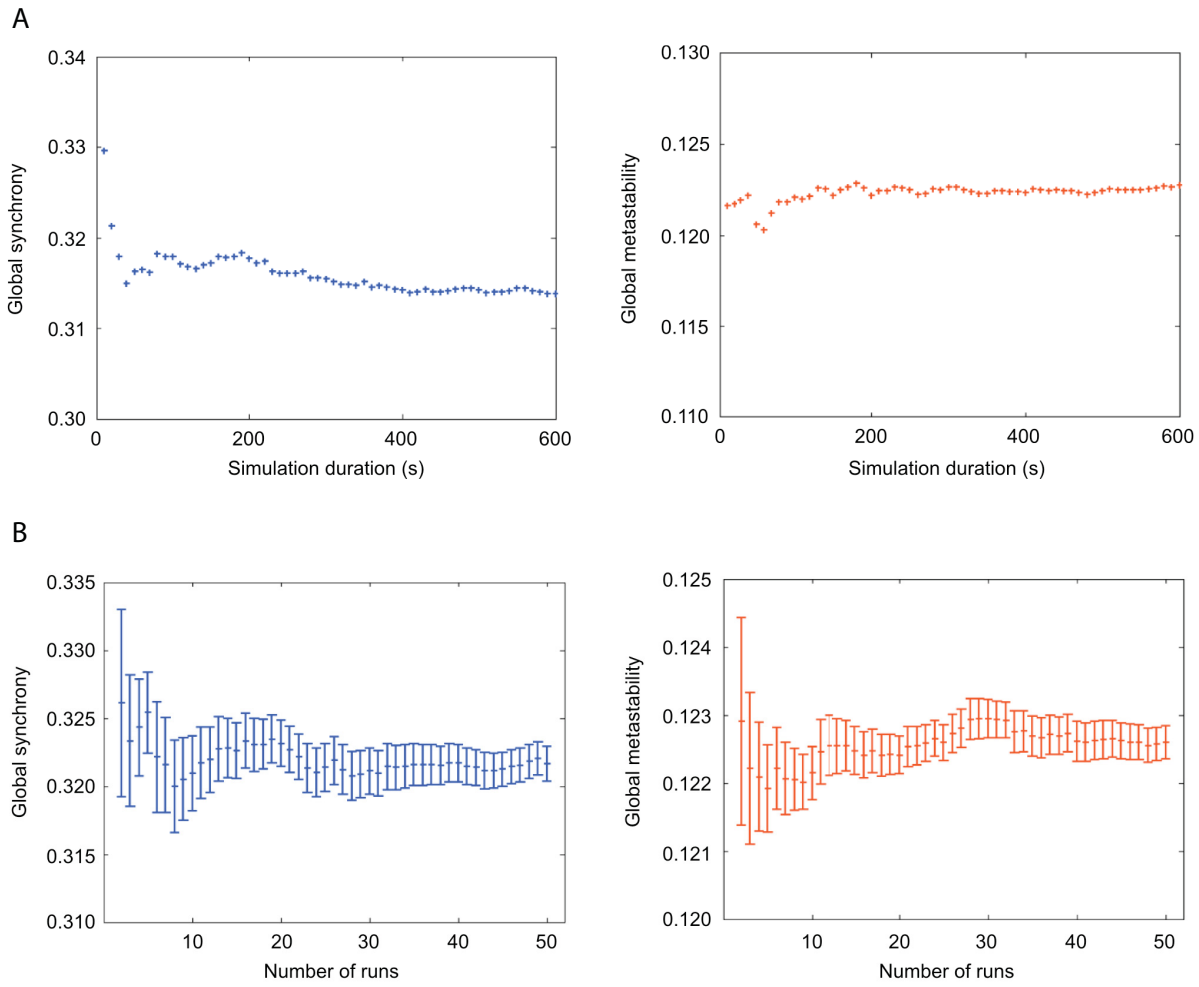

Figure 4.4 | Computational models converge on measures of Multistability and synchrony over short timescales. To estimate the length of simulation required in order to obtain a consistent measure of network dynamics, we iteratively increased the length and number of arbitrary runs of the computational model. The effect of overall length of neural dynamics simulated, and the number of repeated measurements with randomised starting parameters, is shown for global Multistability (Left) and global synchrony (Right).

within the model so as to maximize both global synchrony and Multistability, where <A>(t) is a unit matrix (i.e., a matrix with all elements equal to one). Recent work (e.g., (Cabral, Hugues, et al. 2011, Haimovici 2013)) suggests that biologically-realistic functional connectivity patterns emerge from dynamical computational simulations when they maximize equivalent measures as Multistability.

Measures of global and local network dynamics [Figure 4.3B]

To quantify measures of network dynamics within the computational model, we evaluated the phase history of the computational model either across all oscillators, or for pre-specified clusters of oscillators defined to belong to different intrinsic connectivity networks, using the order parameters R(t) and Φ(t), jointly defined by:

$$R(t)e^{i\Phi(t)} = \frac{1}{N}\sum_{n=1}^{N} e^{i\Theta_n(t)}$$

Where N is the total number of oscillators within the whole brain or a specific cluster. The level of synchrony between simulated timeseries from different oscillators is described by R(t), in terms of how coherently phase changes over time (Cabral, Hugues, et al. 2011, Shanahan 2010b). During fully synchronous behavior, R(t) = 1 and 0 where phase across all phase timeseries is fully asynchronous. The global phase of the entire population of phase timeseries is described by Φ(t). I measure global dynamics in terms of mean global synchrony across the entire simulated timeseries ($\bar{R}$), and global Multistability as the variance σ_R of global network synchrony across the same period (Cabral, Hugues, et al. 2011, Shanahan 2010b).

Two options are available to ensure robust estimation of the synchrony and Multistability measures. The first, which we applied during model validation, is to simulate sufficiently long time-courses. The convergence of global synchrony and global Multistability as a function of time taken into account is visualised in [Figure 4.4A]. The second option, which we applied during the lesion study, is to simulate substantially shorter time-courses but average over a set of simulations with different

initial conditions. The convergence of global synchrony and global Multistability as a function of the number of runs with different initial conditions taken into account is visualised in [Figure 4.4B].

Empirical validation methods [Figure 4.5]

In order to evaluate the model and tune it into an optimal dynamical regime to predict empirical resting-state dynamics, we evaluated the dynamics and functional connectivity of the model across a wide range of different coupling and delay scaling parameters (see above). The range of parameter values studied was guided by previous findings of Cabral et al. (2011), with values of mean delay (τ) located in the physiologically realistic range (1 ms < τ < 15 ms at a resolution of 1 ms), and for 0.5 < k < 25 at a resolution of 0.5 – altogether 800 parameter space values. In addition,

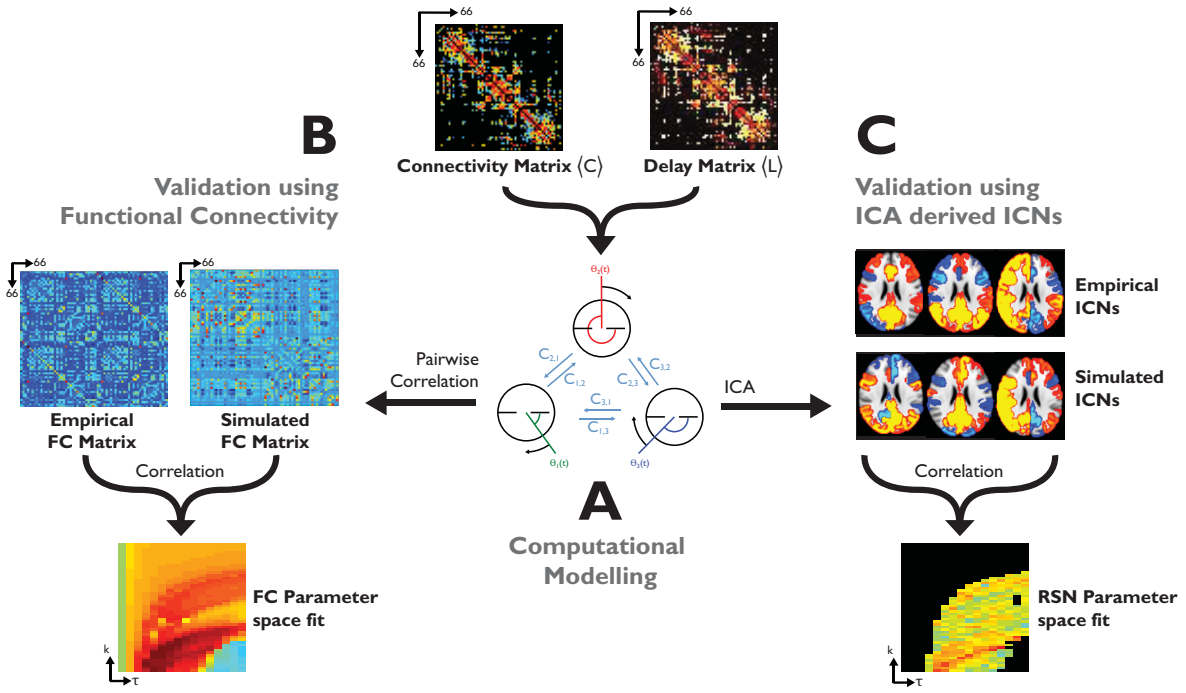

Figure 4.5 | Overview of experimental design. Here, a Kuramoto model, is built using prior information derived from white matter tractography. A). I consider two methodologies for comparing the dynamics of this model with empricial neuroimaging data. B) Using pairwise measures of functional connectivity, correlated with similar empirical measurements; and C) using spatial ICA to estimate networks of intrinsic connectivity (ICNs) in the simulated data, and compare to empirically derived functional connectivity networks.

the natural frequency of each node within the model was constrained to within the gamma range. In setting these parameters, we are implicitly selecting a timescale for the computational model within the sub second timescale. Effectively, defining the units of the D matrix though τ defines the definition of time within the model. When comparing the model to empirical data, this is accounted for by either application of an appropriate filter (such as the canonical haemodynamic model), or an apropriate downsampling regime (as is used here). This allows us to explore using the model, the effect of key and biologically meaningful characteristics, such the scale of neal delays at the level and timescale of neural circuits, whist allowing empirical evaluation of the model using an empirical dataset with an appropriate spatial scale.

To preserve control over the behaviour of the model, we used the same initial conditions for each point when exploring the parameter space. For each position in parameter space, the simulation was run for 660 "seconds". To eliminate dependence of results on initial transient periods, we discarded the initial 60 "seconds" of the model output. Post-processing of phases, such as filtering or use of the Balloon-Windkessel model was avoided to prevent alteration of the results by such steps. It has been shown that the predictive power of a number of models, including the Kuramoto model, is largely insensitive to the presence of the hemodynamic model (Messe et al. 2014). Rather, we evaluated the model output without any additional filtering, but still capturing dynamic interactions between nodes.

Validation using functional connectivity (FC)

The first model validation method compared time-averaged pair-wise FC within the model to empirical FC data from fMRI. Model FC was evaluated using pair-wise correlation (Pearson's rho) between node time-courses, leading to a 66x66 region correlation matrix for the model. I compared the upper triangular of this simulated correlation matrix with pre-published empirical measures of functional connectivity (also measured using pairwise correlation) measured in the same five subjects as the

structural connectivity data (Honey, Thivierge, and Sporns 2010).

Validation using intrinsic connectivity networks

The correlation of individual nodes within the brain likely changes dynamically over time (Hutchison, Womelsdorf, Allen, et al. 2013, Allen et al. 2014, Handwerker et al. 2012, Zalesky et al. 2014, Smith et al. 2012). Methods such as independent component analysis can be used to better characterise patterns of functional connectivity over time, allowing for regions to be involved in multiple networks. Therefore, we also explored a second approach to model validation using an ICA based approach. Briefly,

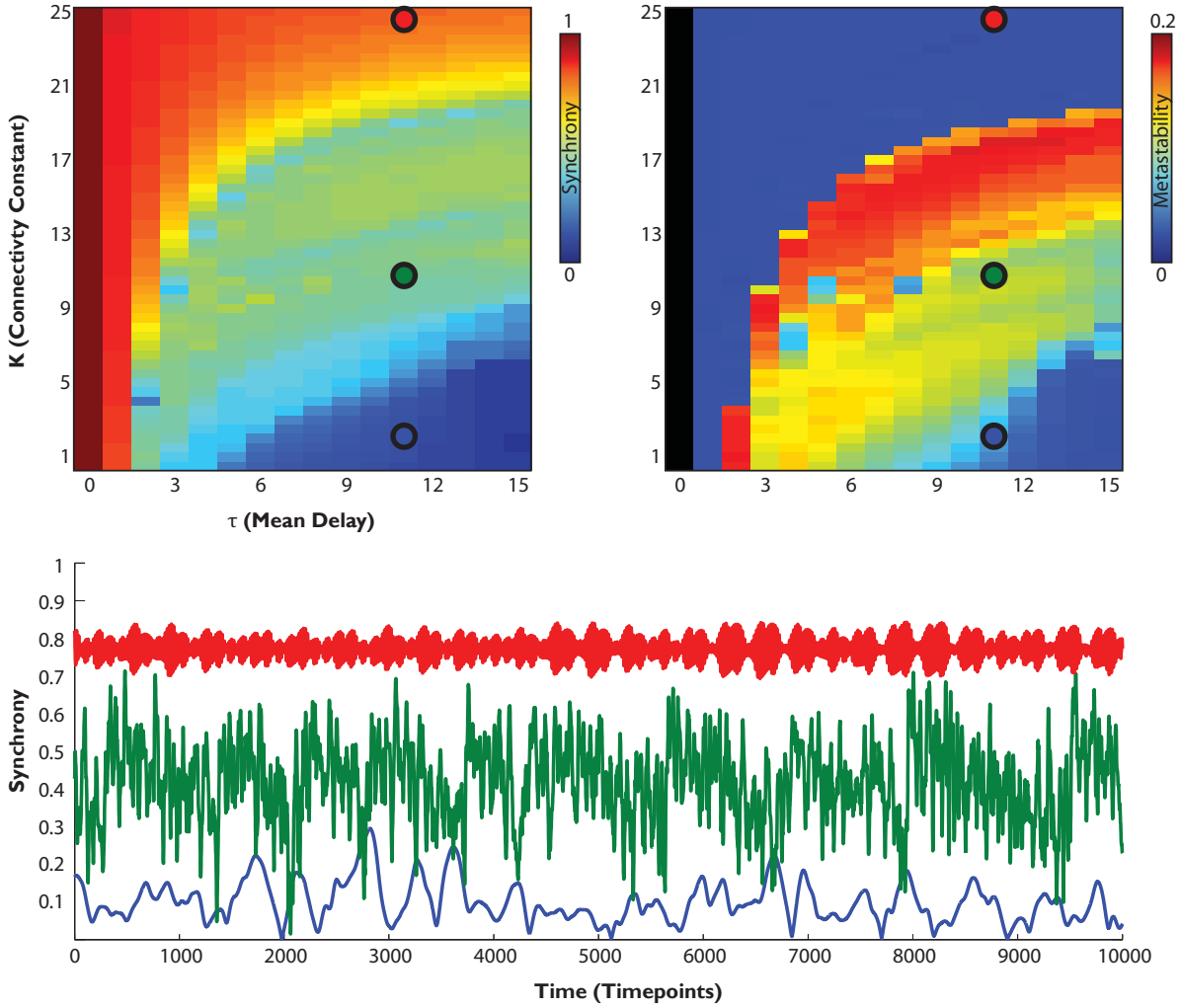

Figure 4.6 | an evaluation of the dynamical properties of the Kuramoto model across the parameter space of connectivity strength (K) and mean conduction delay (τ). Top) Global Synchrony and Multistability. Bottom) exemplar time-courses of the magnitude of the order parameter (Synchrony) for three runs of the model in a high (red), low (blue), medium (green) synchronous regime.

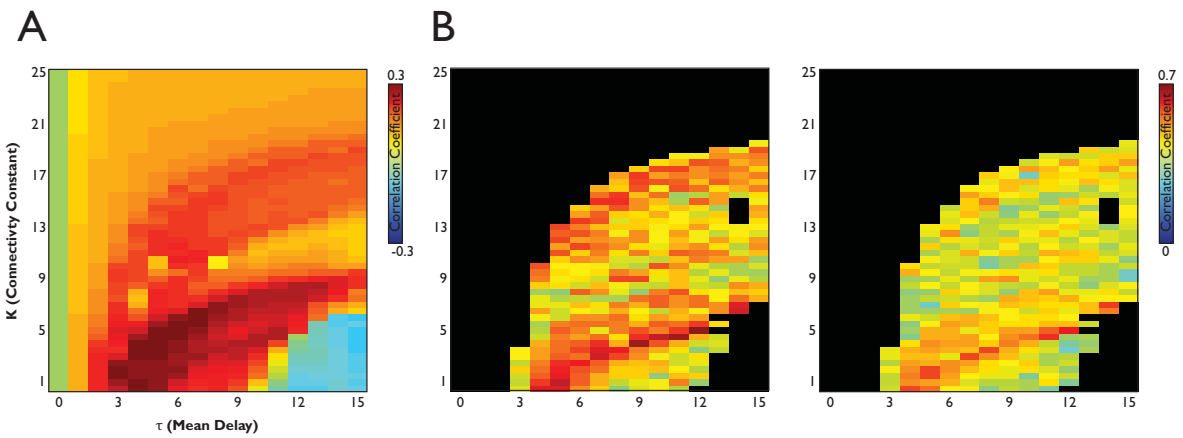

Figure 4.7 | Empirical functional connectivity is best predicted by the model in a region of the model at the start of the phase transition between highly ordered dynamics and disorder. A) Correlation coefficient between measures of pairwise simulated functional connectivity and empirical functional connectivity from fMRI. B) Mean correlation of simulated ICNs with ICNs derived from empirical fMRI. n=10 components (Left), n=5 components (Right)

we estimated how intrinsic connectivity networks defined previously, see (Smith et al. 2009b), overlapped with the 66 cortical ROIs of our model. Modelled timecourses were then extracted in the 66 ROIs, and an ICA performed, resulting in 10 components. For a subset of models from the parameter space, the ICA algorithm failed to converge, either because there was no consistent correlation structure within the dataset over time, or because all regions of the model were fully correlated. Thus, we limited the ICN validation method to parameter space coordinates where dynamics exhibited sufficient variability for the MELODIC algorithm to converge (global Multistability of 0.05 or above). To reduce computational complexity, we temporally down-sampled time-courses to 0.2-second resolution, resulting in a collection of spatial ICN maps for the model to compare against the empirical data using Pearson's correlation. Since the order of components extracted by MELODIC varies, we determined maximal correspondence between empirical and model components by calculating the pair-wise correlation between them and reordering the resulting correlation matrix so as to maximize entries along the diagonal, and defined a cost function of the mean diagonal correlation coefficient. To limit dependence of results on the number of components taken into account, we produced two versions of the cost functions,

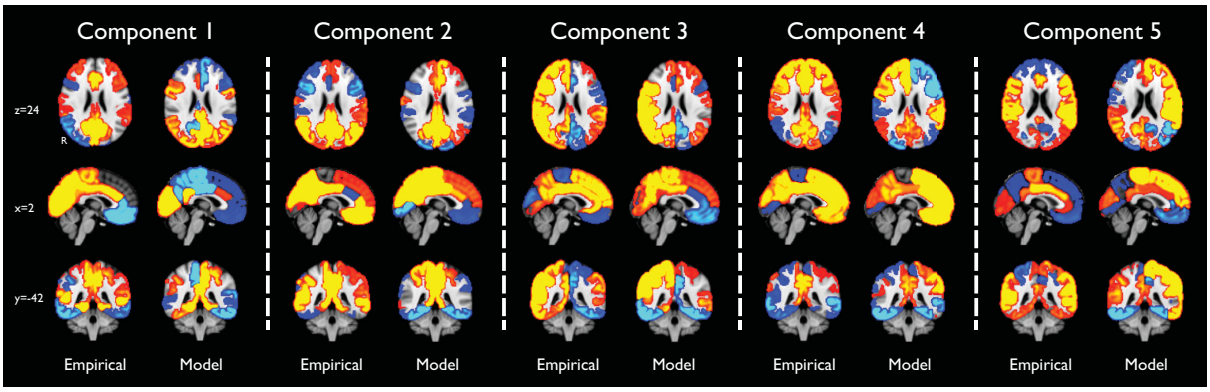

Figure 4.8 | Empirical and Simulated ICNS. Example components from one run of the computational model in comparison with their empirical counterparts. Components are reconstructed into MNI-152 space, and smoothed with a FWHM Gaussian kernel of 5mm for display.

including either the best-matching 3 or 5 components between the modelled and empirical data.

Results

Dynamical properties of the Kuramoto model.

I started by building simulations exploring a two-dimensional parameter space by altering the two key free parameters of the model: the mean velocity (τ) of the delay between nodes, and the overall strength of connectivity (K). For each position within the $<k,\tau>$ plane, we calculated global measures of both synchrony and Multistability using the order parameter described above [Figure 4.6]. Consistent with previous work using this approach (Cabral, Hughes, et al. 2011), we demonstrated that for small coupling strengths the resulting dynamics show low values of synchrony, and that this low synchrony persists over time: i.e. have low Multistability [Figure 4.6, Blue]. As K increases, the model passes into a region of instability indicative of a 'phase transition' during which time the model exhibits Multistable dynamics [Figure 4.6, Green]. As K increases further, there is a region of stable highly synchronous dynamics [Figure 4.6, Red], with lower Multistability. Increasing the length of delays has expands the range of values for K that lead to this zone of instability. Theoretical accounts of networks of Kuramoto oscillators (Cabral, Hugues, et al. 2011, Acebrón et al. 2005) support the observation of a 'phase transition' in the activity of the Kuramoto model with intermediate values connectivity and velocity constants. In network models with an order of magnitude more oscillating nodes, the connectivity constant exhibits a 'critical value', here overlain by the zone of instability, for which the network jumps between incoherent chaotic behaviour, and synchrony. Explorations of smaller scale models demonstrate a more constrained set of dynamical behaviours, with a smooth transition between order and chaos characterised by the zone of instability (Cabral, Hughes, et al. 2011).

Multistable dynamics predicts functional connectivity

In order to explore the dynamical properties of the model which best replicate

empirical patterns of resting state activity in the brain, we compared the model output with measures of functional connectivity estimated by: a) pairwise correlation coefficients; and, b) networks of regions defined by independent component analysis [Figure 4.7]. The correlation between empirical and modelled measures of pairwise functional connectivity (see materials and methods) demonstrated that the fit of functional connectivity from simulated with empirical connectivity is maximised in the region of instability, where Multistable dynamics are greatest [Figure 4.7A]. If functional connectivity is assessed using independent component analysis [Figure 4.8B], the correlation of the top 10 and top 5 components detected in the model with a set of canonical resting state networks (Smith et al. 2009a), provide complimentary evidence that the Multistable dynamics constrained by the structural connectivity of the brain, are important for the emergence of healthy resting state functional connectivity [Figure 4.8].

Discussion

A range of different studies have demonstrated that the large-scale functional connectivity of the brain is predicted by the underlying structural connectivity (Honey et al. 2009). However, structural connectivity only partially explains the functional connectivity of the brain. Firstly, strong correlations exist between regions that have no direct anatomical connectivity, (Honey et al. 2009, Honey, Thivierge, and Sporns 2010); also, whilst structural connectivity is relatively static, functional interactions measured using fMRI change dynamically with cognitive context (Smith et al. 2009a), and dynamically over short timescales (Hutchison, Womelsdorf, Allen, et al. 2013, Hutchison, Womelsdorf, Gati, et al. 2013, Allen et al. 2014, Handwerker et al. 2012, Zalesky et al. 2014, Smith et al. 2012). This suggests that not only is the structure of the brain important in shaping functional connectivity, but the dynamic relationship between individual regions of the brain - or 'nodes' - shapes how functional interactions occur over time. Therefore, understanding the principles underlying spontaneous functional activity in the brain requires an understanding of these dynamics.

In this chapter, we first described an abstract computational model – the Kuramoto model of coupled phase oscillators (Cabral, Hughes, et al. 2011, Acebrón et al. 2005, Breakspear, Heitmann, and Daffertshofer 2010, Kuramoto 1984). I defined a model of 66 phase oscillators modeling activity across the cortex at a macroscopic scale, connected using empirical connectivity defined using diffusion tractography, with realistic conduction delays based on the distance between individual regions of the brain (Hagmann et al. 2008). The dynamics of this type of simulation is dependent mainly on two key parameters: the connection strength and delay (Acebrón et al. 2005). Through numerical exploration of the parameter space of the model, we demonstrate that the coupling strength of the underlying connectivity matrix, shifts the model from a chaotic regime characterised by asynchronous behaviour, through a 'zone of stability', exhibiting strong Multistable behaviours, before moving into a highly synchronous regime. As has been previously reported in explorations of this model

(Cabral, Hughes, et al. 2011), this shift in the dynamics of the model is reminiscent of a second order phase transition within the model dynamics. In many computational models, the point of this phase transition is known as the 'critical' point, balanced between ordered and chaotic dynamics.

Whilst the demonstration that the model is capable of producing a diverse range of dynamical states, an important question is to understand which of these dynamical regimes interacts with the underlying structural connectivity to produce activity reminiscent of empirical resting state activity. Interestingly, the region of the model that produces best fit to measures of empirical functional connectivity is the 'zone of instability' that is associated with this 'critical' phase transition. This is consistent with previous work, such as the study of Cabral et al. (2011), who have explored the connectivity of the default-mode network within their model in a seed-based manner. Our exploration using ICA, extends this work, demonstrating that many higher-order resting state networks emerge within this Multistable regime, rather than just the default mode network. The idea that the critical mode of a computational model best represents empirical connectivity, is also suggested by (Haimovici et al. 2013). They showed with a computational model of brain dynamics that the patterns most strongly resembling empirical resting state networks appear when the system is in a critical state: a dynamical regime situated between order and disorder, which exhibits both correlations between activity of distant areas and high levels of variability sufficient communication to occur over distance (Beggs 2008). Interestingly, the network-like patterns of connectivity were lost for sub- or super-critical dynamics, indicating that criticality might be an important property of healthy brain dynamics. These results align with the present findings, in that our chosen working points exhibit high synchrony and Multistability within the critical transition space, as well as correlation patterns resembling empirical ICNs.

Both validation methods provided similar results, identifying similar regions of the parameter space where the simulated data match with empirical data. The functional

connectivity method is simpler to use; however, the advantage of the ICA method is that it is multivariate and extracts the main components of co-activation from the simulated data while correcting for other non-neural sources of noise. It also allows a ROI to be involved in different resting state networks, possibly reflecting some non-stationary network dynamics. This might be the reason why the ICA validation method identifies a narrower portion of parameter space as exhibiting highest correlations with empirical data.

One potential limitation of the validation framework presented here, is that the timescale over which each source of information is significantly different - i.e. the computational model produces fast timescale interactions (in the range of miliseconds) between regions of the model, where the temporal order of the fMRI data it is compared with is in the multi-second range. This is handled in this case by downsampling the modeled dynamics to the slow (0.2 Hz) range of the fMRI data before calculaing functional connecivity or perfoming an ICA. An alternative approach would be to use faster neuroimaging approaches such as EEG or MEG to evaluate empirical functional connecvitiy. However, such approaches have an implicit trade off between temporal resolution and spatial signal localisation which make evaluation of spatial patterns of coordinated activity at the macroscopic scale difficult. On the other hand, Empirical evidence for dynamic activity in the brain aligned with 'criticality' has been demonstrated in a range of different organisms and scales (Beggs and Plenz 2003, Beggs and Plenz 2004, Kitzbichler et al. 2009, Chialvo 2010, Shanahan 2012, Haimovici 2013), the kinds of multistable activity that we demontrate here in the region of the paramter space that best fits the empirical data, is compatable with criticality. Theoretical accounts of criticality and experimental results for neural systems suggest that critical dynamics maximizes information transmission and processing power of networks. Whilst current theory proposes that healthy neural dynamics operate in a Multistable regime that promotes flexible information processing and behaviour (Shanahan 2010a, Friston 1997, Tognoli and Kelso 2014, Kelso 2012, Bressler and

Kelso 2001). Given that such a perspective would explicitly predict a broad-band scale invariance (for which there is some precident in the neuroimaging literature at the macroscopic scale (Kitzbichler et al. 2009), we may expect that high speed dynamics at the macroscopic scale as generated by the kuramoto model, should show self similar behaviour to the slow neuronal dynamics described in the fMRI data. An extention of the current work which would be broadly confirmatory of this hypothesis could be to evaluate similar measures of macroscopic functional connectivity and evaluate against the parameter space of the model using alternative neuroimaging approaches such as MEG or EEG, which have a considerably faster temporal resolution compared to fMRI, albeit at the cost of spatial precision.

Whilst, the computational model described here relates resting-state functional activity to the structural connectivity of the brain and shows how this is maximized during Multistable and critical dynamical regimes, the brain is not always at rest, and is often focused on a specific task. Whilst the resting brain may have Multistable properties, it is unclear how such dynamic measures of neural activity change or is tuned by cognitive state or how such dynamics relate to behaviour. Equally, in the previous chapter, we demonstrated that structural disconnection predicts significant behavioural deficits following TBI. Traumatic brain injury (TBI) results in damage to structural connectivity producing cognitive impairments, including slowed information processing speed and reduced cognitive flexibility, that may be a result of disrupted Multistable dynamics. Here, we suggest that structure and local dynamics – specifically in a Multistable regime, interact to produce dynamic resting state functional connectivity. Therefore, in the following chapters we expand on these findings in two ways using a combination of computational modelling alongside empirical functional imaging data to:

- Demonstrate how activity in functional networks constrains Multistable dynamics dependent on cognitive context.
- Explore how the structure of the brain relates to behaviour through Multistable dynamics.

The control of global brain dynamics: opposing actions of fronto-parietal control and default mode networks on attention.

5

Introduction

Understanding how cognition emerges from neural activity requires a description of the dynamic interactions between brain regions. Intrinsic functional connectivity networks (ICNs) reflecting underlying patterns of structural connectivity have previously been described (Smith et al. 2009, Honey et al. 2009). However, network activity is dependent on behavioral context, dynamically reconfiguring over time (Fox et al. 2005). Therefore, the investigation of brain networks needs to consider not only the structural connections that constrain functional interactions, but also dynamic changes in functional interactions.

One approach is to consider the brain as a complex dynamical system (Shanahan

2012, Chialvo 2010, Beggs and Plenz 2003, Beggs 2008, Kitzbichler et al. 2009). Multistability, which we here define as the tendency to move endogenously between transient attractor-like states, is an important property of such systems (Friston 1997, Tsuda 2001, Kelso 2012, Shanahan 2010b). According to one hypothesis, increased Multistability in the brain allows more flexible dynamic interactions between regions, whereas reductions in Multistability may accompany persistent, more stable states (Shanahan 2010a).

The relationship between brain network Multistability and cognition is unclear. High Multistability may facilitate transitions between a large repertoire of network configurations, allowing an exploratory cognitive state and the efficient response to changing external events (Fritz et al. 2010, Deco, Rolls, and Romo 2009, Irner 2007). In contrast, once a specific behavior is needed, for example in response to a perceived threat, networks supporting a focused response should be stable over time, corresponding to a reduction in the Multistability of the system. This paper explores the idea that changes in whole-brain Multistability go hand-in-hand with shifts between unfocused, exploratory or 'resting' states and focused attentionally demanding states.

These broadly opposed cognitive states (exploratory vs. focused) are associated with functional differences in well-established ICNs. Activity in fronto-parietal control (FPCN) and dorsal attention networks (DAN) is high when attention is directed externally (Corbetta and Shulman 2002, Vincent et al. 2008, Spreng et al. 2010, Fornito et al. 2012), associated with reduction in activity within the default mode network (DMN) (Singh and Fawcett 2008). These networks show anti-correlated activity over time, which may be important for efficient cognitive function (Irner 2007, Kelly et al. 2008, Deco, Jirsa, and McIntosh 2011, Shanahan 2012).

I investigated the relationship between brain activity and global dynamics (particularly a measure of the variability in the spatial deviation over time that we use as a proxy

for Multistability) in two behavioral states: 1) an attentionally demanding task (the choice reaction time task (CRT)) and 2) an unconstrained 'resting' state. [Figure 5.1] presents a high-level schematic of our approach, in which computational simulations complement empirical neuroimaging data. I first recorded functional MRI data during both performance of the CRT and with the subject at 'rest' [Figure 5.1A]. I then simulated the neural dynamics arising in these distinct cognitive states using a computational model of brain function consisting of a network of Kuramoto oscillators (Kuramoto 1984), constrained by the white-matter connectivity of the brain [Figure 5.2A]. Previous work has demonstrated that patterns of fMRI activity measured within the DMN can be simulated by similar computational models (Cabral et al. 2011).

I tested the hypothesis that the CRT would be associated with decreased Multistability, whereas the unconstrained rest state would be associated with the reverse pattern. As expected, we found this change both in the simulated data and empirical data (using proxy measures for network dynamics), providing converging empirical and theoretical evidence for global changes in network dynamics relevant to cognitive control.

Materials and Methods

Empirical functional data

Subjects

Sixteen subjects (eight females, mean age: 28 years) had functional MRI whilst performing: 1) a continuous version of the choice reaction time (CRT); and 2) a 'rest' scan where there was no explicit task. In addition, 24 separate neurologically healthy subjects (eight male; mean age, 35.0 years) took part in a further fMRI study where the CRT was interleaved with rest in a 'blocked' design. Data from this second study was used to functionally localize regions more active during the CRT or during rest. All participants gave written consent, were checked for contraindications to MRI scanning and had no history of significant neurological or psychiatric illness. The Hammersmith, Queen Charlotte's and Chelsea research ethics committee awarded ethical approval for the study.

Image Acquisition protocols

Functional MRI Data was acquired using a Phillips Intera 3.0 Tesla MRI scanner using standard protocols. Earplugs and padded headphones were used to protect participants' hearing during the scanning procedure. Standard T1 weighted structural images were also acquired for co-registration and segmentation of functional data.

Stimulus design

During the CRT task an initial fixation cross was presented for 350 ms. The fixation cross was followed by a left or right response cue arrow to which subjects were instructed to respond as quickly and as accurately as possible with a button press with the right or left index finger. Each trial was presented for 1000ms, with an inter-stimulus interval of 1000ms during which the fixation-cross was displayed on screen. Trials were repeated

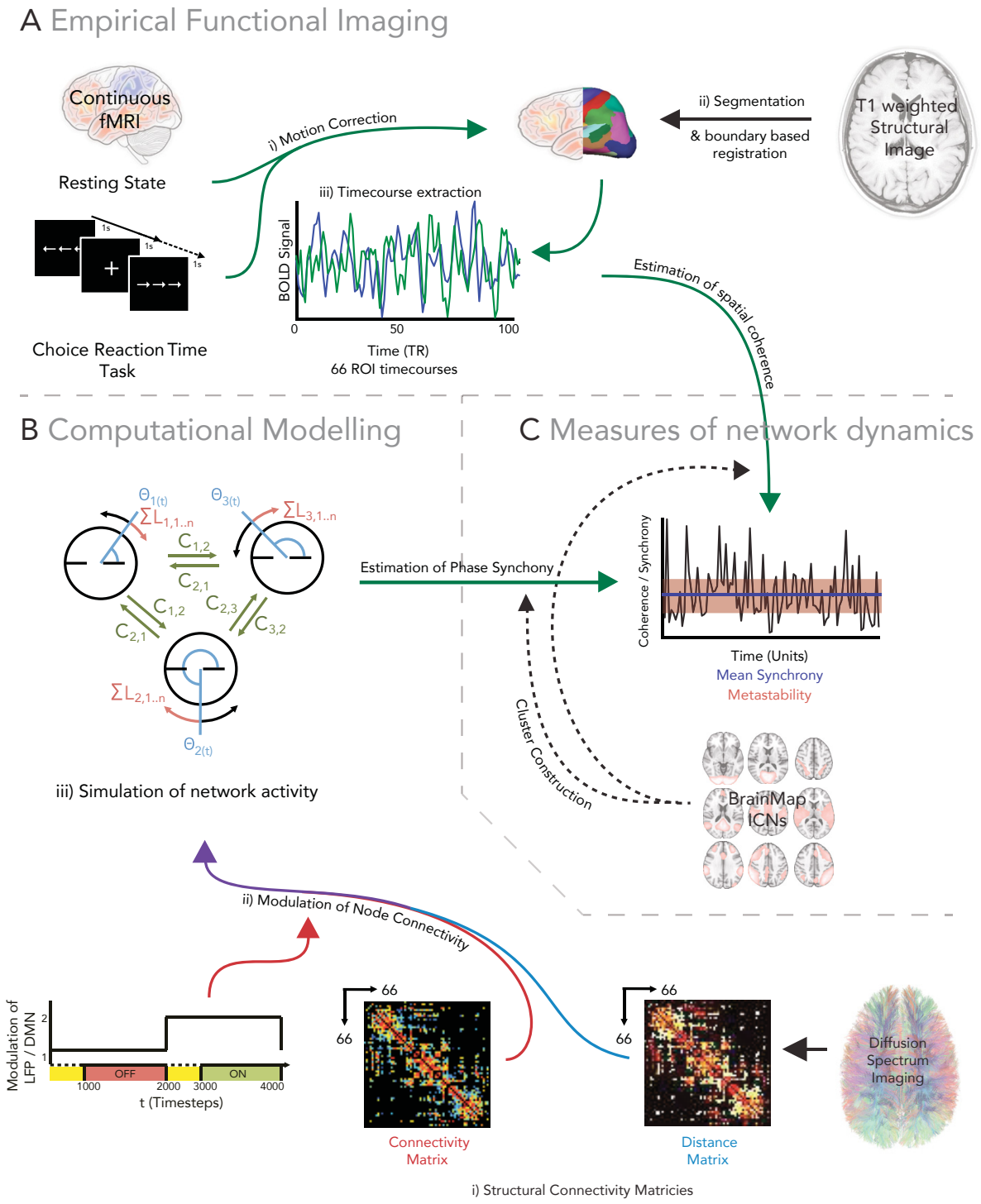

Figure 5.1 | Overview of experimental design. A) fMRI was used to estimate global measures of network dynamics during task or rest. Example time courses are extracted from the right precentral gyrus (blue) and the left precuneus (green) B) I used a computational model to simulate neural dynamics using dynamical systems framework constrained by structural connectivity. C) I used analysis of the spatial deviation of empirical fMRI data, and the phase output of the computational model to compare the global dynamics of empirical data, and dynamics of a computational model constrained by structural connectivity and activation of specific regions of the brain. The example demonstrates spatial deviation over time of empirical data during the choice reaction time task.

continuously for the duration of the functional acquisition. There was no rest period, jitter in ITI or other baseline task during the continuous run. As such, dynamics during this task were not due to alternating between rest and task or different task demands. During the 5 minute resting state run, participants were asked to lie still in the scanner with their eyes closed, and were not asked to perform any task in particular.

Analysis of functional imaging data [Figure 5.1A]

Preprocessing of functional data involved realignment of EPI images to remove the coarse effects of motion between scans using FMRIB's Motion correction tool MCFLIRT (Smith et al. 2004, Jenkinson et al. 2002). T1 images for each subject were segmented into 66 regions homologous with those characterized in the Hagmann human cortical connectivity datasets using the Desikan-Kilaney Freesurfer atlas (Hagmann et al. 2008, Dale 1999, Desikan et al. 2006), [Appendix 5.1]. The segmented T1 images were registered to the motion corrected data using boundary-based registration (Greve and Fischl 2009). Mean BOLD timeseries for each cortical region were extracted for both the continuous CRT and resting state scans. I band-pass filtered the data between (0.01 and 0.15) and then regressed out six direction motion parameter model estimated by MCFLIRT (Smith et al. 2004, Jenkinson et al. 2002), and timeseries sampled from regions of white-matter and cerebrospinal fluid in order to reduce physiological and movement confounds.

Analyses were either calculated on all regions simultaneously (global) or within specific predefined intrinsic connectivity networks (local). The ICNs were estimated by projecting the resting-state independent components corresponding to putative brain networks (rather than non-neural noise) from (Smith et al. 2009) onto the 66 regions of interest. A region was classified as part of a specific ICN if the mean value from the ICA within was $z>1.64$ (nominal $p>0.05$). The ICNs were labeled (following (Smith et al. 2009)): primary and secondary visual, dorsal attention, default mode,

motor, auditory, salience and right and left lateralized fronto-parietal networks.

Given the relatively few timepoints in the fMRI timeseries, analysis methods within the phase space are significantly limited by implicit edge effects of both the required filtering regime, and transformation fo the analytical signal, such as wavelet coherence, or hilbert transofmration of the data (Kitzbichler et al. 2009, Chang and Glover 2010. Note in future chapters, fMRI is collected for a significantly longer period of time, making such approaches more appropriate) significantly reducing the power of any statistical observations within the data presented. Therefore, instead of attempting to calculate equivalent measures of multistaibility to the computational model within phase space, we define a compromise measure of spatial deviation, which captures the extent to which regions of the brain are coherent across space (i.e. across the entire brain, or within a cluster of regions, we then track how this measure of spatial activity deviates across time, resulting in a measure which captures similar properties to the computational multistability measure. Our proxy measure of Multistability, is defined as the variability in spatial deviation of the signal globally or locally (within a network) over time according to the following equation:

$$V(t) = \frac{1}{N}\sum_{i=1}^{N} | S_i(t) - \bar{S}(t)|$$

Where V is the spatial deviation of a group of N regions at each timepoint (either of all 66 for global measures or a specific subset for local coherence within an ICN), is the signal for an individual region of the brain (see above) and is the mean of all considered timecourses. I define our proxy measure of Multistability as the standard deviation of V across time and our proxy measure of synchrony as the reciprocal of mean spatial variance across time,

Functional localizer

Given the absence of a baseline condition for the continuous functional CRT and rest datasets described above, we were not able to use these to demonstrate the neural systems activated in the different states. Therefore a blocked design MRI dataset interleaving CRT and rest was used in order to functionally localize the networks within the brain that are activated during CRT > rest, and rest > CRT. This data and analysis of the CRT data was the same as the healthy control CRT dataset described in (Bonnelle et al. 2011).

Computational Modeling [Figure 5.1B]

Simulation of cognitive states

Neural dynamics were modeled computationally, using the Kuramoto oscillator model described in Chapter 4. Structural connectivity used as a prior within the computational model was estimated using Diffusion Spectrum Imaging (Hagmann 2009) [Figure 5.2]. To simulate activation of a particular network of brain regions implicated in a particular cognitive state (for example the DAN/FPCN), the efferent connection strengths from the networks nodes to other nodes was increased (although qualitatively similar results were achieved when bilateral – afferent and efferent – connections were modulated), see [Appendix 5.1] This simple manipulation was sufficient to change the global dynamics and produce qualitatively similar changes to those observed with the empirical timeseries.

In the simple Kuramoto oscillator model (presented in detail in chapter 4), simulating different cognitive states involves modulating the effective connectivity between oscillators. If a given brain region is more active, this is assumed to result in increased influence over connected regions. In the model this is determined by the activity matrix, The simulations presented here run for 4000 time steps. During the first 2000 time steps, A(t) is a unit matrix [Figure 5.1B, OFF]. During the final 2000 time steps,

we simulated activation of specific cognitive networks (e.g., the DMN) by selecting nodes of the specific network (e.g., PCC, IPL) and increasing by a range of factors between 1.1 and 3 one of the two connecting edges, so as to increase the 'outgoing' connectivity of these regions, according to the undirected connectivity matrix [Figure 5.1B, ON]. In order to allow for starting effects and extraneous effects of sudden manipulation of the model, we discarded the first 1000 time steps of each phase of the simulation. Pilot simulations indicated that similar results were found for a range of modulation values. By including the OFF, baseline state, we can investigate the effect of different states on synchrony and Multistability (i.e., does simulated activation increase or decrease these measures). Here we consider simulated activity within the fronto-parietal control network (FPCN/DAN) by modulating nodes representing the

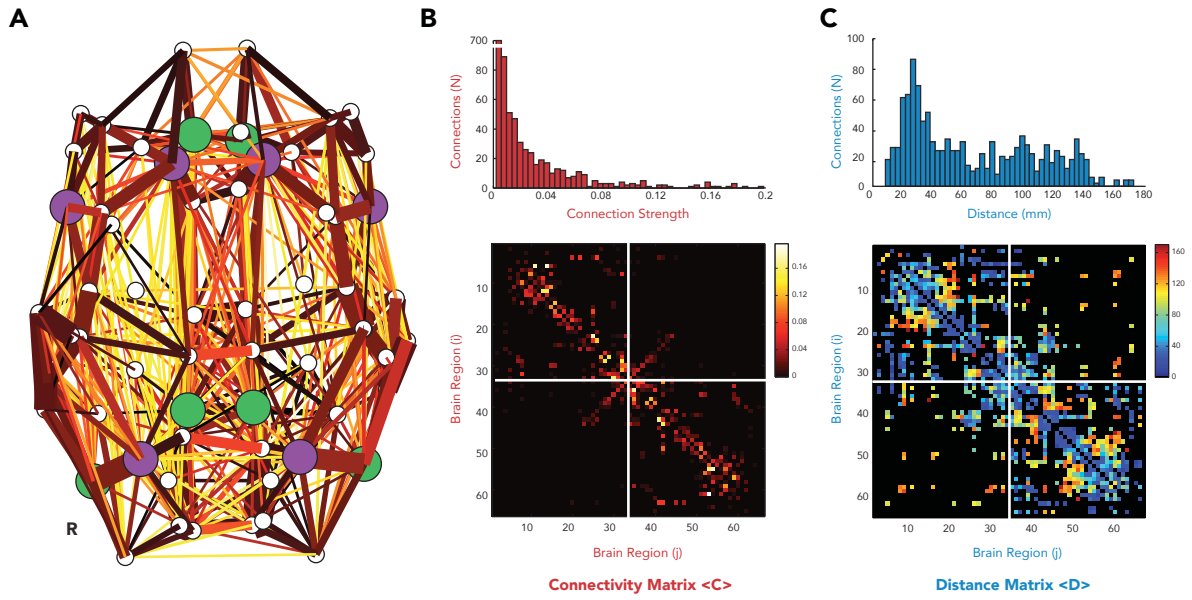

Figure 5.2 | Structural Overview of the computational model. (A) Graphical Overview of the 66 region structural connectivity matrices used in the Kuramoto oscillator system. Thickness of connecting vertices represents the strength of connections according to the Connectivity matrix (B). Hotter colors represent longer connections, according to the distance matrix (C). Regions are sorted according to regions in (Table 1). Nodes comprising the fronto-parietal control network and dorsal attention network (FPCN/DAN) are highlighted in purple. Nodes comprising the default mode network (DMN) are highlighted in green.

bilateral inferior frontal gyrus, superior frontal gyrus and superior parietal lobules [Figure 5.2A Purple]; and the Default mode network (DMN) by modulating nodes representing bilateral inferior parietal, anterior and posterior cingulate [Figure 5.2A, Green].

The first 20 time-steps of both the ON and OFF periods were discarded to allow for evolution of stable network dynamics. Measurements of network synchrony and Multistability (see below) were calculated for both the ON and OFF periods to determine the change from baseline. Measures of Multistability and synchrony in the computational simulations are described in chapter 4.

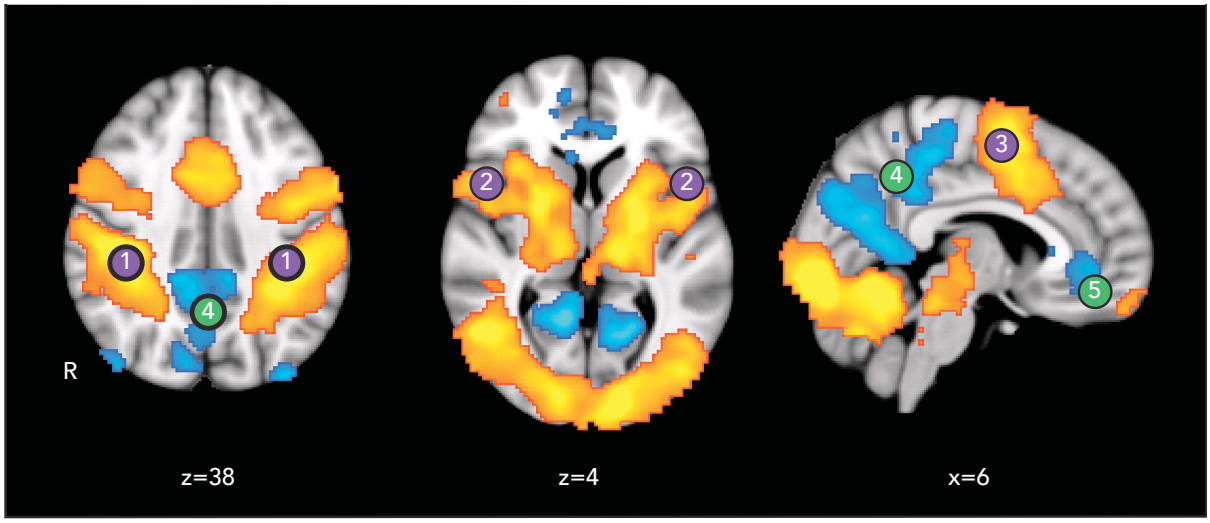

Figure 5.3 | Standard fMRI analysis of CRT task. Regions of the brain active during the choice reaction time task using standardized fMRI subtraction analysis. CRT>Rest (orange-red) Rest>CRT (blue). (1) Superior parietal lobule. (2) inferior frontal gyrus – pars opercularis. (3) posterior portion of the superior frontal gyrus. (4) anterior and (5) posterior cingulate gyrus. Cluster corrected $p<0.01$, $z=2.3$, $n=26$.

Results

The choice reaction time task activates the fronto-parietal control network and deactivates the default mode network

Consistent with the existing literature (Sharp et al. 2011, Bonnelle et al. 2011), performance of the CRT during fMRI was associated with significant activation in visual, somatosensory and motor regions of the brain, as well as bilateral parts of the fronto-parietal control network (FPCN/DAN) and the dorsal attention network (DAN) [Figure 5.3, Purple]. This comprised activation in: (1) bilateral superior parietal lobule; (2) the frontal operculum and pars opercularis; and (3) the posterior superior frontal gyrus. As expected, parts of the DMN were deactivated relative to rest during performance of the CRT. These included: (4) the anterior and (5) posterior portion of the cingulate gyrus.

Global and local dynamics of empirical data in different cognitive states

In order to assess the global dynamics of the brain during the CRT task and rest, we collected fMRI during continuous performance of the CRT task and a separate rest fMRI run. I sampled BOLD timeseries from 66 different regions of the brain, and assessed the Multistability and synchrony across all regions of the brain or within subsets of regions that form intrinsic connectivity networks (See Materials and Methods). [Figure 5.4] shows the group results of global and within network variability across time for both CRT and REST. [Figure 5.5] illustrates the difference between CRT and rest on global and local dynamics in a single subject, with noticeably greater variability in the measure of synchrony over time. Across all the subjects, performance of the CRT was associated with a mean reduction in global Multistability, compared to rest

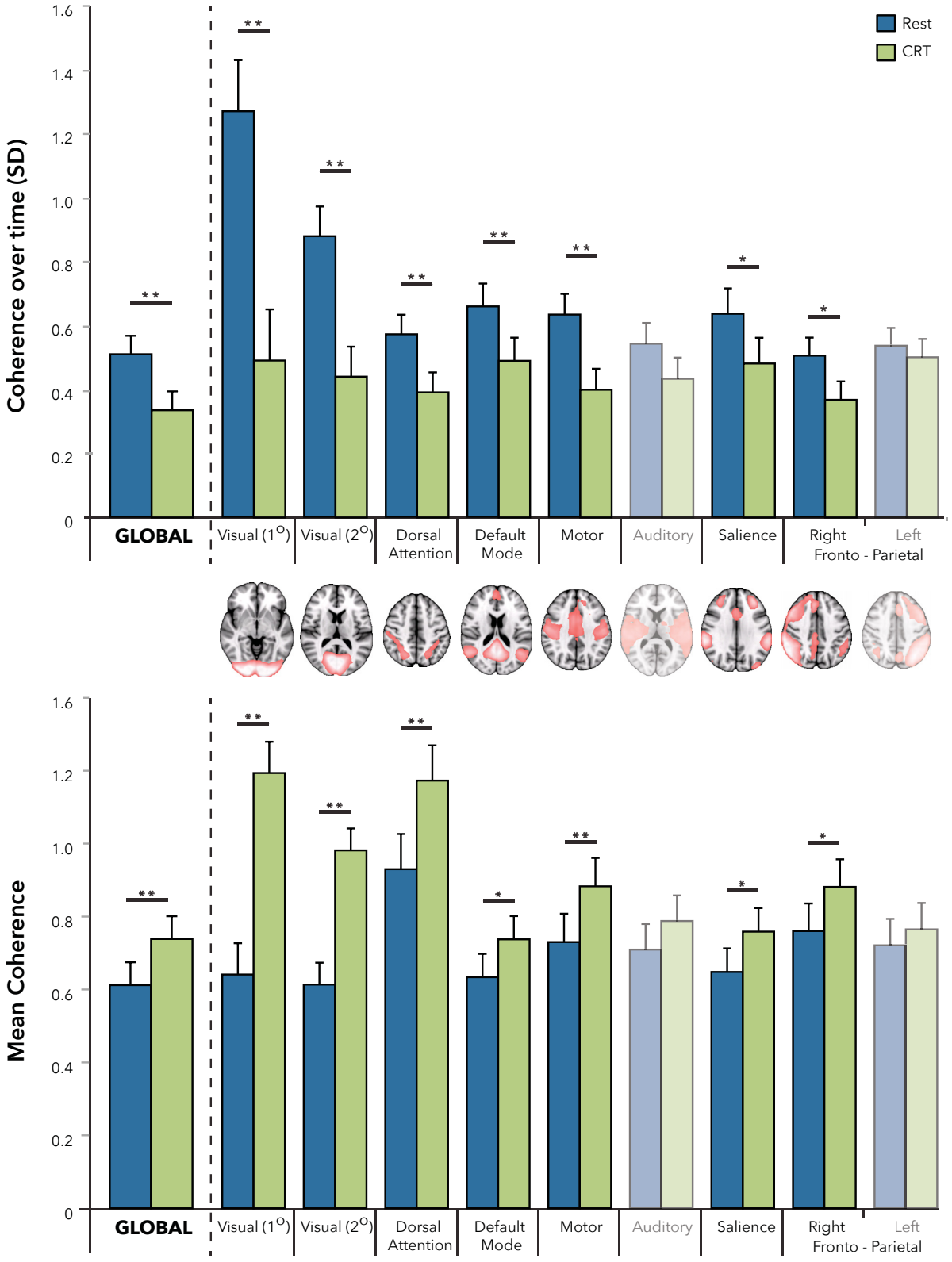

Figure 5.4 | Dynamic activity of the brain during rest and sustainted attention. Measures of variability in coherence over time (top) and mean coherence (bottom) between CRT (in green) and rest (in blue), for continuous BOLD fMRI data. Single asterisks show differences that are statistically significant at $p<0.05$ (2-tailed T-Test), double asterisk is significant at $p<0.01$; n=16. Error bars ± 1 SEM.

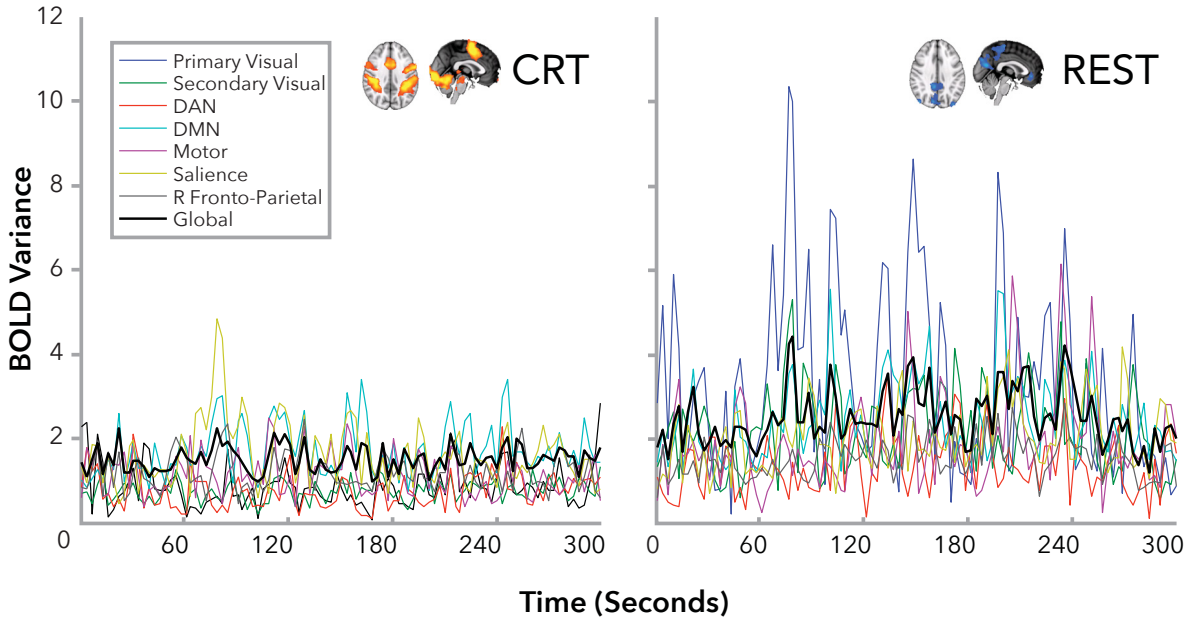

Figure 5.5 | Figure 5.5 Results from a single illustrative subject. The global (i.e., all 66 regions) and local (i.e., specific ICNs) timeseries of synchrony during the CRT (on the left) or at rest (on the right) Greater variability in synchrony (i.e. our definition of Multistability) can be seen at rest.

(t_{15}=-3.18 P<0.01) and an increase in global synchrony (t_{15}=3.02 P<0.01).

To explore dynamics within ICNs, we also performed a task x ICN repeated measures ANOVA for Multistability and synchrony using networks defined by independent component analysis [Figure 5.5]. For Multistability, there was a significant main effect of task ($F_{1,15}$=17.65, p<0.01), ICN ($F_{2,30}$=21.16, p<0.001) and an interaction between task and ICN ($F_{2,27}$=20.327, p<0.001). For synchrony, there was a significant main effect of task ($F_{1,15}$=17.43, p<0.01), ICN ($F_{3,49}$=26.2, p<0.001) and an interaction between task and ICN ($F_{3,39}$=26.94, p<0.001). Post hoc t-tests demonstrated significant decreases in Multistability within specific ICNs, corresponding to primary visual (t_{15}=-5.22, p<0.001), secondary visual (t_{15}=-5.87, p<0.001) and motor areas of the brain (t_{15}=-4.09, p<0.001), the Dorsal Attention (t_{15}=-2.98, p<0.01), Default mode (t_{15}=-3.08, p<0.001), Salience (t_{15}=-2.19, p<0.05), and Right Fronto-parietal control networks (t_{15}=-2.73, p<0.05).

In the previous analysis the 66 regional timeseries were not variance normalized prior

to calculating Multistability and synchrony. However, qualitatively similar (although weaker) results were found with variance normalization: Multistability was significantly reduced during CRT compared to rest both globally (t_{15}=2.23, p<0.05) and within the motor network (t_{15}=4.99, p<0.001). Global synchrony was significantly increased during CRT compared to rest (t_{15}=3.02, p<0.01), as was local synchrony within the Dorsal Attention (t_{15}=3.22, p<0.01), Default mode (t_{15}=-2.75, p<0.05), Salience (t_{15}=2.51, p<0.05), and Right Fronto-parietal control networks (t_{15}=2.51, p<0.05).

Performance on the CRT task was highly consistent across subjects, as expected based on previous findings in neurologically healthy participants (Sharp et al. 2011, Bonnelle et al. 2011). Mean accuracy on the task was very high 97.7±0.02% and mean reaction time was fast and consistent across subjects 0.45±0.061s. Given this lack of variability, we did not expect reliable relationships between individual variability and measures of Multistability. However, there was a negative correlation between Multistability during CRT in the DMN and the standard deviation of the reaction time (r_{16}=-0.57 p<0.05), but this does not survive Bonferroni correction.

There was no difference in head movement between the two conditions (mean relative motion per TR was 0.076mm at rest and 0.075mm during the CRT task (t_{15}=0.18, ns). Therefore, the differences in Multistability and synchrony are highly unlikely to be due to artifacts resulting from head motion between the two conditions.

Computational modelling of cognitive network activation

To complement the empirical analysis, the dynamical systems model allowed us to simulate the effects of increased activity in the FPCN/DAN and the DMN on global Multistability and synchrony. The model involved 66 Kuramoto oscillators (one corresponding to each segmented brain region) coupled together according to a human white-matter tractography atlas [Figures 5.1 and 5.2]. Either the baseline state or FPCN/DAN or DMN active states were simulated and measures of dynamics

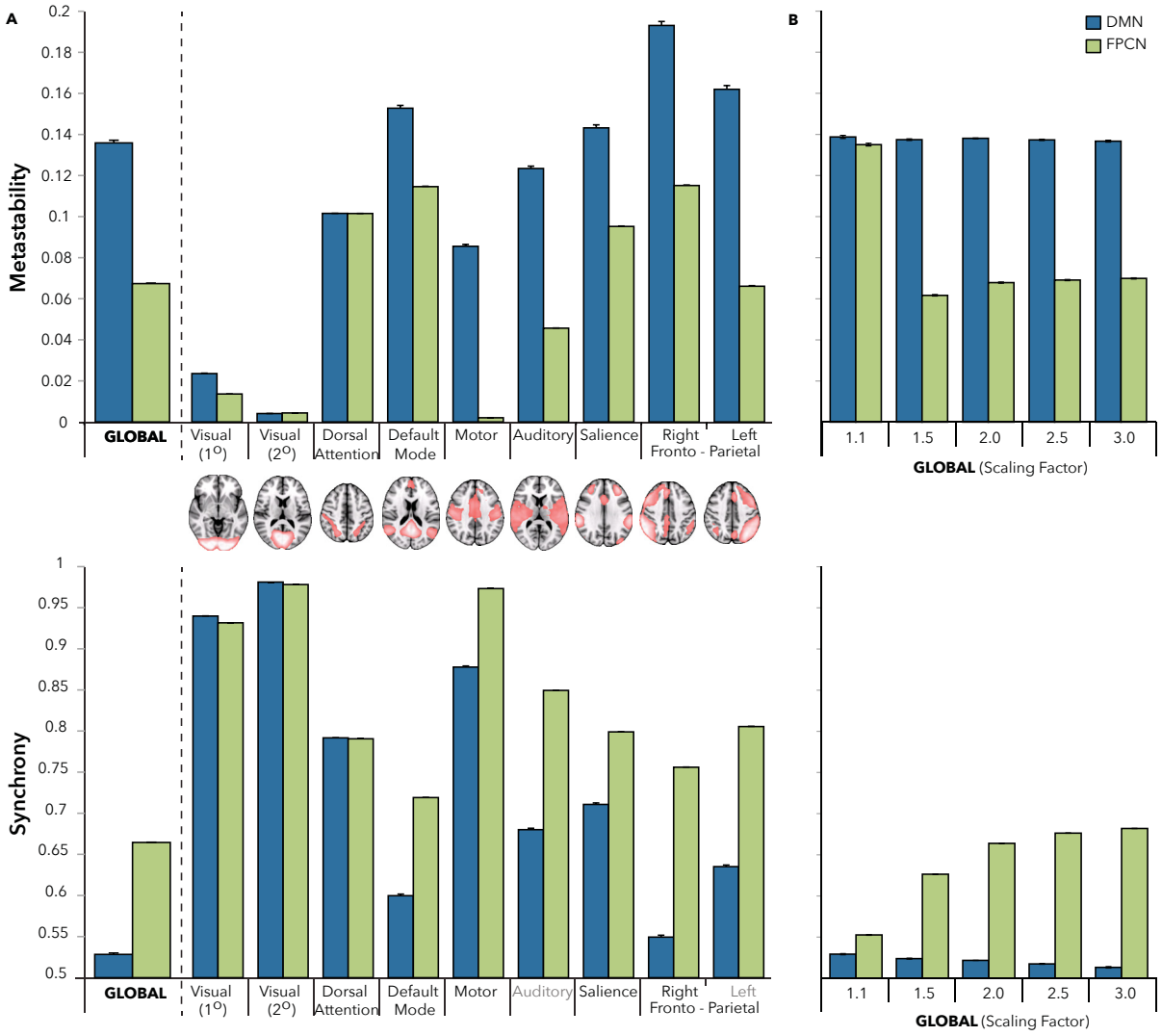

Figure 5.6 | Simulated neural dynamics during activation of the DMN and FPCN. Global and local measures of Multistability (top) and synchrony (bottom) from the simulations of FPCN/DAN (associated with the CRT task – in green) or DMN (associated with the rest state, in blue). Results are averaged across 15 different simulations. (A) Local measures of network dynamics within ICNs during simulation of FPCN/DAN or DMN activation with a scaling factor of 2. (B) Global changes in dynamics for a range of different scaling factors. Error bars ± 1 SEM.

calculated.

Dynamics were explored globally and locally within clusters of nodes of the model, defined by in the same way as the empirical data. I then ran a task x cluster repeated measures ANOVA for Multistability and synchrony [Figure 5.6A], mirroring the empirical data. For Multistability, there was a significant main effect of task ($F_{1,15}$=2022, p<0.001), ICN ($F_{2,16}$=20476, p<0.001) and an interaction between task and ICN ($F_{2,27}$=1946.38, p<0.001). For synchrony, there was a significant main effect of task ($F_{1,15}$=7288.45, p<0.001), ICN ($F_{2,22}$=47446.51, p<0.001) and an interaction between task and ICN ($F_{2,26}$=3864.95, p<0.001).

Post hoc t-tests demonstrated that global Multistability was significantly reduced during CRT compared to rest (t_{15}=-46.16, p<0.001). Significant decreases in Multistability were also seen in clusters of oscillators corresponding to primary visual (t_{15}=-45.82, p<0.001), Default Mode (t_{15}=-26.39, p<0.001), Salience (t_{15}=-32.14, p<0.001), Motor (t_{15}=-92.84, p<0.001), Auditory (t_{15}=-67.75, p<0.001) and Left (t_{15}=-46.16, p<0.001) and Right (t_{15}=-37.39, p<0.001) Fronto-Parietal Networks. In contrast, Multistability increased within clusters of oscillators representing secondary visual areas of the brain (t_{15}=89.70, p<0.001), although this result had a very small magnitude compared to the other clusters of oscillators.

A significant increase in global network synchrony occurred during simulated activation of the FPCN/DAN, compared to similar activation of the DMN (t_{15}=-82.37 P<0.001,). This was associated with decreases in synchrony within the Default Mode (t_{15}=-69.25, p<0.001), Salience (t_{15}=-47.91, p<0.001), Motor (t_{15}=-69.25, p<0.001), Auditory (t_{15}=-101.05, p<0.001) and Left (t_{15}=-82.37, p<0.001) and Right (t_{15}=-87.03, p<0.001) Fronto-Parietal Networks. In contrast, synchrony decreased with task within clusters of oscillators representing the Dorsal Attention Network (t_{15}=4.74, p<0.001), and Primary (t_{15}=34.86, p<0.001) and Secondary (t_{15}=391.88, p<0.001) Visual areas of the brain; although, the magnitude of the effects for all three of these clusters was

very small compared to the other ICNs.

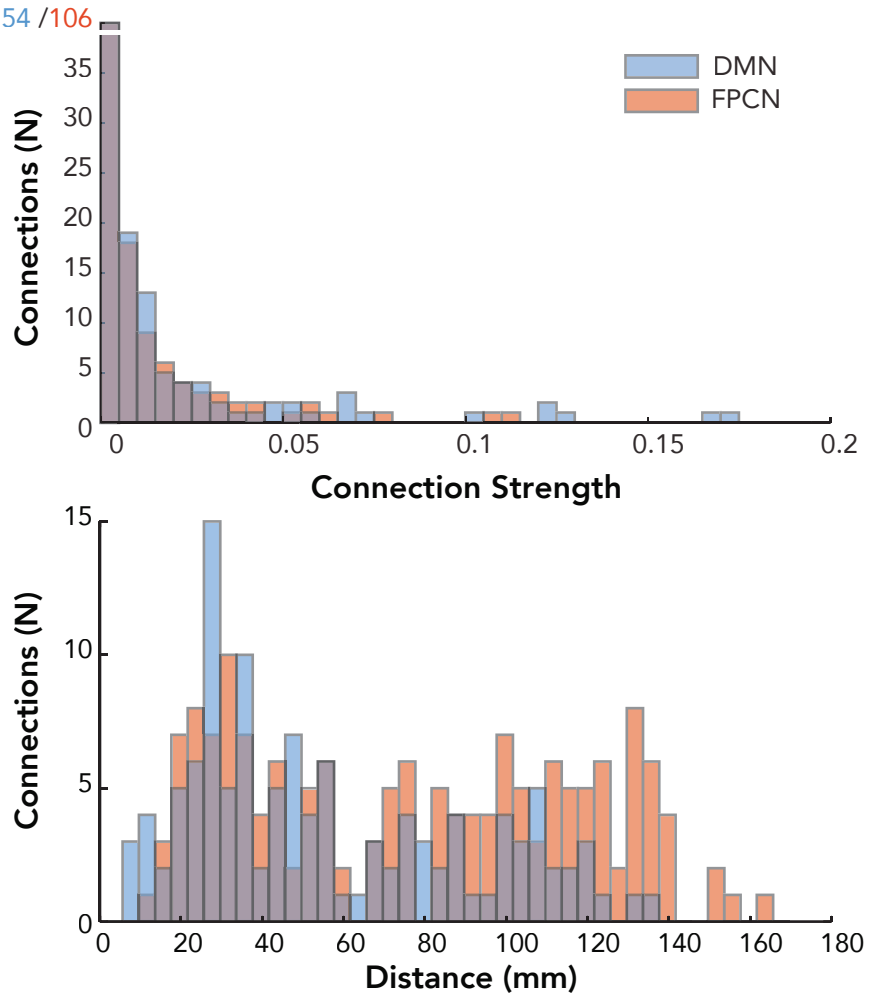

Figure 5.7 | Connectivity of the DMN and FPCN. Overview of connectivity of the connectivity strength (top) and length (bottom) of edges projecting from nodes modulated during simulated activation of either the DMN (Blue) or the FPCN (Red)

The reported effects were found by doubling the coupling of oscillators involved in the DMN or the FPCN/DAN. The effects are consistent using a range of different factors to modulate the couplings between regions. Factors of 1.1, 1.5, 2.5 and 3 demonstrated similar changes in network synchrony and Multistability (although they differed in the magnitude of their effects) [Figure 5.6B].

To better understand why there are differential effects of the DMN or FPCN/DAN on dynamics in the computational model, we studied how the graphs changed. Modulating the FPCN/DAN altered the connectivity of 160 edges of the network (mean connection strength 0.007±0.017, mean distance 77.49±41.51mm). Whereas, modulating nodes representing the DMN altered connectivity along 118 edges of the network (mean connection strength 0.016±0.032, mean distance 56.37±33.79mm). The distributions in both strengths and lengths of connections between the FPCN/DAN and the DMN were significantly different (Kolmogorov-Smirnov test: strengths $p<0.005$ and lengths $p<0.001$) [Figure 5.7].

Discussion

Here we use computational modeling and human neuroimaging to show how measures of whole brain dynamics vary depending on the behavioral state and how this may be a consequence of the effective network organization of the brain. As expected, when subjects performed an attentionally demanding task that requires an external focus of attention, activity in the fronto-parietal control network (FPCN/DAN) increased and activity in the default mode network (DMN) decreased (Sharp et al. 2011, Fox et al. 2009, Spreng et al. 2010). These relative changes in network activity were accompanied by a global increase in spatial deviation over time and a reduction in the variance of spatial deviation over time (our proxy empirical measures of synchrony and Multistability). The same pattern of results was also found across the majority of specific ICNs, suggesting that the effect is global. These findings support the proposal that more stable neural dynamics emerges during periods of consistent and focused behavior. Our computational simulation results show the same qualitative pattern as the empirical results, providing a possible mechanistic explanation of how this global change in brain activity might be controlled. The simulations suggest that increasing activity in the FPCN/DAN produced a reduction of global Multistability and increased synchrony. In contrast, increased activity in the DMN produced increased Multistability and reduced synchrony. Across most ICNs, there was the same pattern of local decreases in Multistability and increased synchrony with the CRT task, mirroring the empirical results (although there was a small subset of ICNs with the opposite pattern, albeit with a very small effect size compared to the other ICNs).

Our converging computational and empirical work suggests that global neural dynamics are 'tuned' by varying levels of activity within the FPCN and DMN, which have the effect of shifting the system into a more or less Multistable state. This is consistent with theoretical and experimental work suggesting the brain exists in a critical state: at a 'tipping point' between order and disorder. The scaling parameters used in the simulations were chosen to simultaneously maximize both Multistability

and synchrony, features that would be consistent with a critical system (Beggs and Plenz 2003, Kitzbichler et al. 2009, Chialvo 2010, Shanahan 2012, Haimovici 2013). Critical systems balance the competing demands of information propagation around a system with the need to maintain stable functional long and short scale connections (Beggs 2008, Beggs and Plenz 2003). Therefore 'tuning' of criticality within the brain by selective activation of functional networks may increase or decrease the information capacity of the system depending on behavioural context. For example, at rest with activated DMN, the information capacity of the system is maximised at the expense of network stability, whilst during active attentional states, FPCN/DAN activation results in increased stability of the network, but reduced information capacity.

The DMN is typically more active during stimulus independent thought, and when maintaining a broad, attentional state (Buckner, Andrews-Hanna, and Schacter 2008, Zhang and Raichle 2010, Sharp et al. 2011, Bonnelle et al. 2011). Common to these types of behavior is the lack of behavioral focus, which could be thought of as 'releasing' neural activity, thereby allowing it to take on multiple different network configurations over time. This variability in network configuration would result in relatively low synchrony and increased Multistability when measured across the whole brain. In contrast, to efficiently perform a task like the CRT, a consistent neural configuration of visual, motor and prefrontal cortical activity needs to be maintained over time. This would allow an individual to maintain their attention on the task, and prevent behavioral interference from internal thoughts or competing sensory stimuli that are irrelevant to task performance. This consistent network activity would result in relatively high synchrony and low Multistability. This mapping between cognitive processes and whole-brain dynamics is in marked contrast to many theories of cognition that propose a discrete coupling between a region or network of brain regions and a specific cognitive ability.

The work here suggests the FPCN/DAN can influence sustained attention through stabilization (reduced Multistability and increased synchrony) of the temporal

dynamics of the whole system. Similarly, the simulation of DMN activation provides a possible mechanistic explanation of the functional role of the DMN, in 'permitting' the system to move into a more unconstrained state. In this state the brain shows higher Multistability and lower synchrony, exhibiting more labile dynamics, spontaneously passing between different states that would facilitate both mind-wandering and maintaining a broad attentional cognitive state.

One of the most striking findings from the computational work is that differential effects on global Multistability and synchrony can emerge from the same type of connection strength increase in the two networks. As the underlying connections and initial strengths in the model are based on white matter tract structure, this provides evidence that the network connections are 'hard-wired' to produce these different actions on network dynamics. This shows how flexible changes in large-scale network dynamics could be produced by increased effective connectivity in two opposing networks, in the absence of any long-distance inhibitory network connections. Therefore, the model provides a putative mechanistic explanation of how network topology (i.e. a functional constraint imposed by structural connectivity) relates to functional global dynamics. Although the simulated DMN and the simulated FPCN/DAN conditions both involved modulating the connectivity from equal numbers of nodes (three bilateral pairs of cortical regions), the distributions of the affected connections are different. Specifically, the connections from the DMN are predominantly strong, short-range connections, whereas the FPCN/DAN [Figure 5.7] are more, longer and weaker connections. These results suggest that increasing long-range, weaker connections may enhance the overall stability of the network, whereas increasing the effect of shorter, stronger connections has a much smaller effect and may reduce network stability. Future computational and empirical work is needed to explore precisely how these graph-theoretic measures can explain the contrasting effects of different networks on global brain dynamics.

There are a number of limitations to the work. The computational model we have

used is obviously a simplification of real brain function. For example, the simulation is built on a relatively (compared to the brain) low-dimensional connectivity matrix of 66 regions. The constraints inherent in streamline tractography using diffusion MR mean that the matrix is not directed, but instead all connections are bidirectional. In addition, long distance connections in the connectivity matrix (for example inter-hemispheric pathways) may be difficult to resolve accurately as uncertainty in streamline location introduced by factors such as crossing fibers, increases with the length of the streamline (Jones 2010a, b). At the level of individual nodes, we also assume all nodes to be equivalent, and differences in known cyto-architecture are not modeled. These limitations mean that precise, quantitative comparisons between the simulations and the brain were not expected. Equally these limitations may reduce the power of graph-theoretical interpretation the modeling results (see above). Difficulties with the measurement of BOLD fMRI signal such as partial volume effects, regional differences in vascular reactivity or susceptibility artifacts also make precise quantitative comparisons challenging. The effects of these limitations are likely to be most pronounced on dynamics within small clusters of regions, where inaccuracies with empirical measurement of tracts and BOLD signal will have a larger effect.

However, despite these limitations, the simulation provides important insights into the relationship between the structure of the brain, patterns of functional activity and cognition. It is striking that qualitatively similar relationships between network activity and global brain dynamics can be observed, even though the model contains no constraints about the functional roles of the regions involved (e.g., the model does not 'know' that DMN regions are more active at rest). The work demonstrates how such a simple model can, at least at the level of global network dynamics, replicate the broad task-evoked changes in BOLD seen with fMRI, even though the model is based on nothing more than the network topology (i.e. the structural connections within the brain).

Taken together the work shows how changes in the balance of activity between

key brain networks could shift attentional state between an unfocused/exploratory mode characterised by high Multistability, and a focused/constrained mode with low Multistability. I propose that the balance of activity between the FPCN and the DMN acts to 'tune' global brain Multistability, which influences how consistent brain network activity is over time.

The human connectome confers cognitive flexibility through Multistable neural dynamics

6

Introduction

To understand the brain in health and disease requires an account of how neural ensembles act in concert to generate behaviour (Deco et al. 2008, Chialvo 2010, Uhlhaas and Singer 2006, Tognoli and Kelso 2014). One approach is to consider the brain as a complex system (Chialvo 2010, Friston 1997). In this framework, current theory suggests an essential property of neural activity is Multistability, a dynamical regime in which neural ensembles are able to coordinate rapidly, flexibly engaging and disengaging without becoming locked into fixed interactions (Tognoli and Kelso 2014, Friston 1997, Shanahan 2010b). Moreover, Multistability is thought to confer optimal information processing capabilities, flexible behaviour and memory (Irner

2007, Deco, Jirsa, McIntosh, Sporns, and Kotter 2009, Shanahan 2010b)

Theoretical studies demonstrate that the emergence of multistable dynamics is contingent on the coupling between modules of a dynamical system (Friston 1997, Shanahan 2010b, Cabral, Hughes, et al. 2011, Strogatz 2001). In particular, Multistability emerges when coupling has "small-world" topology with short average path lengths and high clustering (Watts and Strogatz 1998, Wildie and Shanahan 2012, Bassett and Bullmore 2006) of computational-units. Recently, networks of anatomical connections have been incorporated within computational simulations of large-scale neural dynamics, suggesting multistable dynamics provide a link between structural and functional connectivity (Deco, Jirsa, McIntosh, Sporns, and Kotter 2009, Cabral, Hughes, et al. 2011, Honey et al. 2009, Hellyer et al. 2014).

The disruption of neural dynamics is thought to be important in brain disorders (Uhlhaas and Singer 2006), likely caused by abnormal structural connectivity (Boly et al. 2009, Sharp, Scott, and Leech 2014, Friston 2002, Cabral et al. 2012). Traumatic brain injury (TBI) – a leading cause of disability in young adults – frequently results in diffuse axonal injury (DAI), which disrupts long-distance white matter tracts connecting brain regions (Kinnunen et al. 2011, Johnson et al. 2013). Damage to these connections alters the spatiotemporal properties of functional brain networks (Bonnelle et al. 2012, Sharp et al. 2011), resulting in long-term cognitive problems, including impairments in cognitive (Hellyer et al., 2013) flexibility, memory and information processing speed (Kinnunen et al. 2011, Bonnelle et al. 2011, Jilka et al. 2014). Cognitive inflexibility after TBI may be observed as poor performance on tests of task switching (Kinnunen et al. 2011, Hellyer et al. 2013, Jilka et al. 2014, Caeyenberghs, Leemans, Heitger, et al. 2012). Extreme inflexibility may appear as perseveration, the repetition of a particular response, such as a phrase or gesture, despite the cessation of a stimulus. Therefore, TBI provides an ideal paradigm to examine how altered dynamics relate to

structural connectivity and behavior.

Here, using empirical and computational approaches, we investigate how Multistability arises from the structural connectome and relates to behaviour [Figure 6.1]. I test whether: (i) structural disconnection following TBI (measured using diffusion tensor imaging) is associated with reduced Multistability (measured using resting-state fMRI); (ii) Multistability is associated with behavioral measures of cognitive flexibility, memory and information processing. Furthermore, we use computational simulations to investigate the consequences of structural disconnection on large-scale neural dynamics, to demonstrate how disconnection following TBI results in altered Multistability.

Materials and Methods

Participants

63 traumatic brain injury (TBI) patients (mean age ±SD: 37.4±12.37 years) and 26 healthy control subjects (mean age ±SD: 35.96±17.61 years) were scanned using standard functional and structural imaging protocols (see below). All participants gave written consent, were checked for contraindications to MRI scanning and had no history of significant neurological or psychiatric illness prior to TBI. The Hammersmith, Queen Charlotte's and Chelsea research ethics committee awarded ethical approval for the study.

Image acquisition

Standard protocols were used to acquire functional, structural and diffusion tensor MRI data using a Phillips Intera 3.0 Tesla MRI scanner, using an 8-array head coil, and sensitivity encoding (SENSE) with an under sampling factor of 2. For each participant, diffusion-weighted volumes with gradients applied in 64 non-collinear directions were collected. The following parameters were used: 73 contiguous slices, slice thickness=2mm, field of view 224mm, matrix 128×128 (voxel size=1.75×1.75×2mm), b value=1000 and four images with no diffusion weighting (b=0s/mm^2). Earplugs and padded headphones were used to protect participants' hearing during the scanning procedure. I additionally, we collected a standard high-resolution T1 image for segmentation and image co-registration. Resting state Functional MRI images were obtained using a T2*-weighted gradient-echo echoplanar imaging sequence with whole-brain coverage (repetition time/echo time, 2,000/30 ms; 31 ascending slices with thickness 3.25 mm, gap 0.75 mm, voxel size 2.5×2.5×5mm, flip angle 90°, field of view 280×220×123 mm, matrix 112×87). Quadratic shim gradients were used to correct for magnetic field inhomogeneities within the brain.

Neuropsychological assessment

A subset of patients (62, mean age ±SD: 37.53±12.45 years) performed a paper and pencil, neuropsychological test battery and 49 performed a computer-based choice reaction time task. Our analysis focused on three cognitive measures shown previously to be sensitive to impairments following TBI: Associative memory (AM), using the immediate recall and retention measure of the People Test from the Doors and People Test; and Executive function (EF), using the Trail Making Test alternating switch-cost index. Of this subset of patients, 49 also completed the Choice Reaction Time task that assesses speed of processing.

Analysis of functional imaging data [Figure 6.1A]

Pre-processing of functional data was performed according to standard analysis approaches: briefly, this included realignment of EPI images to remove the coarse effects of motion between scans using FMRIB's Motion correction tool MCFLIRT (Smith et al. 2004). T1 images for each subject were segmented into 164 cortical and subcortical regions using the Destreux Freesurfer atlas (Fischl et al. 2004). The segmented T1 images were registered to the motion corrected data using boundary-based registration (Greve and Fischl 2009). Subsequently, mean BOLD time series for each cortical region were extracted for the resting state scans. I band-pass filtered the data between 0.01 and 0.2 Hz to remove sources of non-neural noise and focus on slow modulations in BOLD, that have previously been associated with intrinsic connectivity networks (Niazy et al. 2011). To correct for additional effect of scanner and motion and physiological artefact we next regressed out from each time course for each of the 164 regions of interest, the six motion parameter time courses estimated by MCFLIRT (Smith et al. 2004) as well as time series sampled from regions of white-matter and cerebrospinal fluid. (I note that additional motion correction was also performed across participants in higher-level analyses comparing dynamic

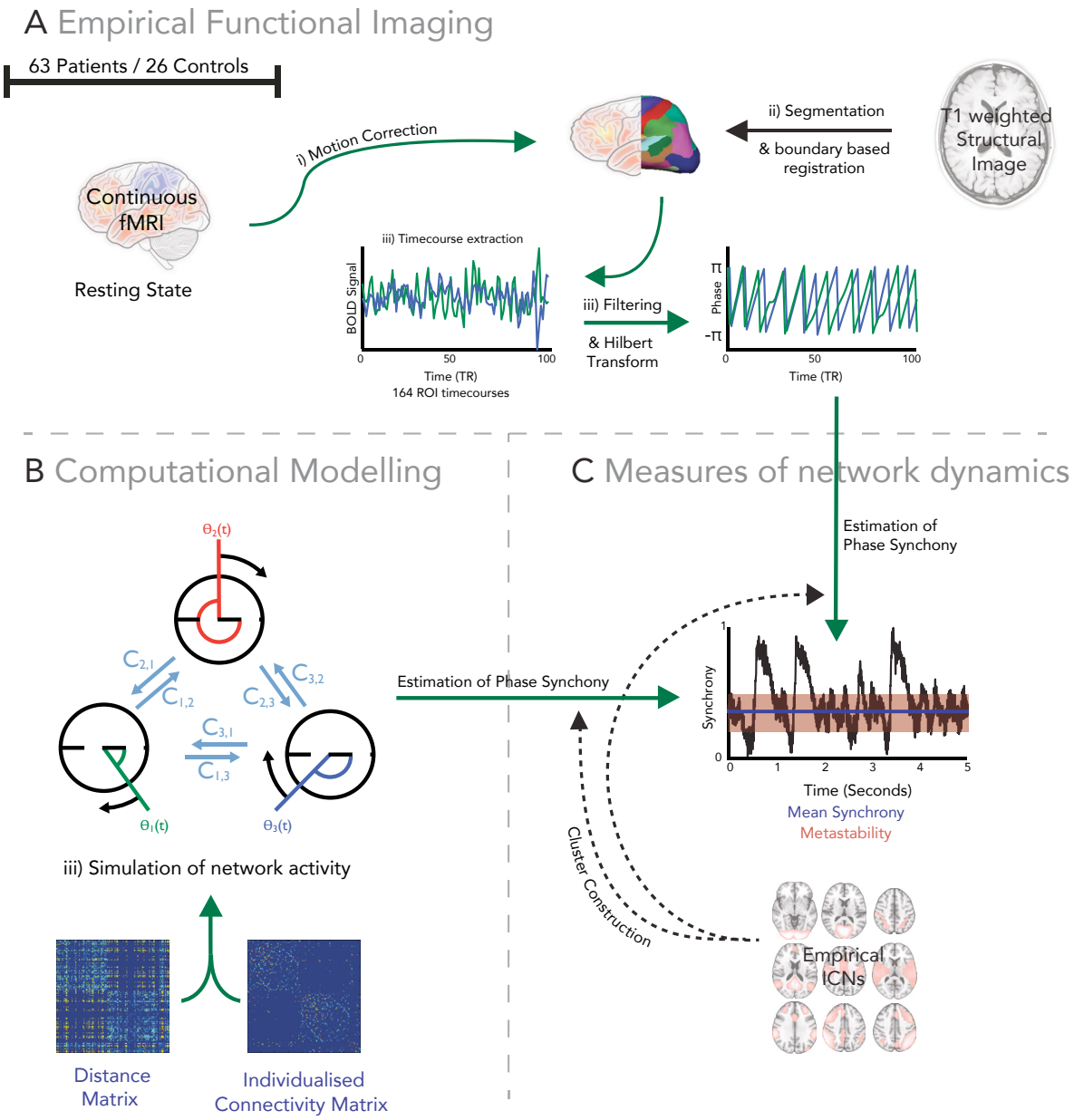

Figure 6.1 | Overview of experimental design. A, fMRI was used to estimate global measures of network dynamics during rest in 63 Patients and 26 Controls. B, I used a computational model to simulate neural dynamics using dynamic systems framework constrained by structural connectivity. C I used a Hilbert transformation of the fMRI data and the phase output of the computational model to compare the global dynamics of empirical data and the dynamics of a computational model constrained by white matter structural connectivity.

measurements between groups, see below).

To facilitate comparison between the computational model and empirical data, we performed Hilbert transforms on each of the 164 region-of-interests' time series from the empirical data, resulting in 164 phase time series. Measures of network dynamics were either calculated on all regions simultaneously (global) or within specific predefined intrinsic connectivity networks (local) (see Measures of global and local network dynamics, below).

In order to provide a set of canonical intrinsic connectivity networks, both to assess network dynamics and to optimize the computational model, we performed independent component analysis on the 164 region timeseries datasets in a group of 10 independent healthy control subjects using FSL MELODIC (Beckmann et al. 2005). For network-level analyses, clusters were generated from resulting spatial maps in 164 region space, where a region was included in each of 15 independent clusters, if $z>2.3$.

Analysis of structural connectivity data

Estimation of healthy structural connectivity network [Figure 6.2A]

The mean location and probability of structural connections was estimated in a group of 10 independent healthy control subjects [Figure 6.2A]. Structural T1 images were segmented into white matter and the same 164 cortical and subcortical grey matter regions as used to sample the FMRI data, using Freesurfer (Greve & Fischl, 2009) and the Destreux Freesurfer atlas (Fischl et al. 2004) This produced a mask for each region in each participant's T1 native space. Diffusion imaging data was reconstructed using the FSL diffusion toolkit using standard protocols (Behrens, Johansen-Berg, et al. 2003). I further modelled the probability distribution of fibre direction within each voxel in order to account for crossing fibres (Behrens, Woolrich, et al. 2003). Non-linear registration was used to calculate a warp-field between conformed Freesurfer

space and the DTI b0 image, using the FSL non-linear Image registration tool (Andersson, Jenkinson, and Smith 2007). The warp-field was then applied to masks for white matter and each of the 164 cortical and subcortical grey matter regions using nearest-neighbour interpolation. Individual grey matter masks were dilated by a single voxel and multiplied by the white matter mask, in order to generate regions of interest (ROIs) to be used as seeds and targets for tractography at the boundary between white and grey matter surfaces (Gong et al. 2009).

Probabilistic tractography, using 5000 random streamline samples per voxel was used to estimate the connectivity matrix <C> between each of the 164 other regions alongside a spatial distribution of connective fibres between each region. The probability of connections between two regions $C_{i,j}$ was defined as the proportion of all fibres sent from region i which successfully reached region j. As probabilistic tractography cannot determine directionality of connections between cortical regions and the size of seed and target ROIs may differ for each connection, we define $C_{i,j}$ as the mean of the forward and reverse connections between regions, i.e. $C_{(i,j)} = 1/2(C_{(ij)}+C_{(ji)})$. To minimise the number of false positive connections, a thresholding approach was used to generate a binary matrix which by only retaining connections which had a consistent probability across all subjects from the tractography group (Gong et al. 2009). The relationship between the number of streamlines and the underlying information propagating properties of the tracts is unclear and this is likely to be a particular problem for long-distance connections (Gigandet et al. 2008, Jones 2010a, b). For this reason, we binarized our reference connectivity dataset. The length matrix (i.e., the length of tracts between pairs of regions) was estimated using the Euclidean distance between the centres of gravity of each individual ROI in standard MNI152 space. Euclidean distance is inexact, since tracts are not likely to follow the shortest distance between regions, but it is a good first approximation of the distances and has been used extensively in a range of similar computational modelling approaches (Deco, Jirsa, McIntosh, Sporns, and Kotter 2009, Cabral, Hughes, et al. 2011, Deco

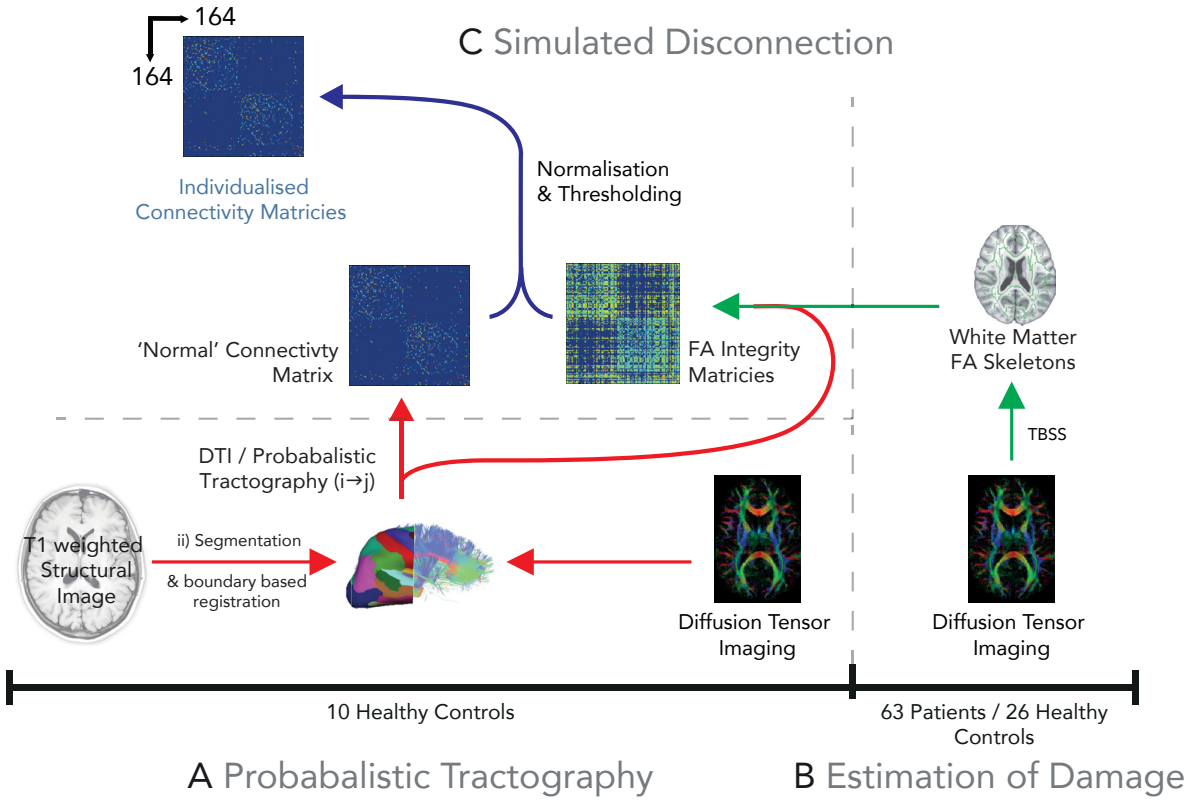

Figure 6.2 | Estimation of structural disconnection in TBI patients vs controls. A, To define a standardised connectivity matrix to perform computational simulation, probabilistic tractography was performed in 10 independent age matched healthy control subjects, resulting in a binary connectivity graph and spatial estimates of probable tract location for each connected edge (see materials and methods). B, Measures of tract integrity (FA) were estimated in each of the 63 Patients and 26 healthy controls by generating a 'skeleton' for each subject using the pre-processing steps of TBSS. C, For each edge of the reference connectivity matrix, each subject's FA skeleton was projected though the spatial mask for each edge, resulting in a 164 region 'white matter integrity' matrix for each subject. C, For each subject, the reference binary connectivity map was weighted according to relative reduction in tract integrity in each individual subject (see materials and methods), resulting in a individual weighted connectivity matrix for each of the 63 TBI patients and 26 Healthy controls.

et al. 2008)

Estimation of individual structural connectivity [Figure 6.2B]

Global and focal reductions of Fractional Anisotropy (FA) in TBI patients have been shown to bias tractography estimation in TBI patients (Squarcina et al. 2012) potentially resulting in spurious differences such as potentially false increases in structural connections following injury. Therefore we did not perform tractography on patients and controls. Instead, we use an unbiased approach as follows: first of all

we used Tract-Based Spatial Statistics (Smith et al., 2006) for each patient and control, resulting in an a skeletonised FA map for each subject. In order to demonstrate that there were significant reductions in FA in patients compared to controls, we fitted a general linear model using FSL Randomise (Nichols and Holmes 2002, Winkler et al. 2014).

In order to estimate integrity for individual tracts for each patient and control, FA values for all voxels lying within each tract region of interest (as defined using tractography on independent controls, see the previous section) were averaged together. This resulted in a 'tract integrity' FA matrix for each patient and control [Figure 6.2C]. Subsequently, we calculated the standard deviation and mean of the mean FA of each tract from the independent group of healthy controls (who had been used to define the tractography). Then, for each patient and control, we subtracted the mean and divided by standard deviation, resulting in a scaled structural connectivity value for each tract in the matrix. To simulate damage to the connectivity matrix <C>, if any edge from the scaled FA matrix for an individual fell below a certain threshold it was 'lesioned'. Rather than removing the tract (which is overly destructive given the nature of the traumatic axonal injury where the tract remains but is damaged) we instead reduce connectivity by a fixed amount [Figure 6.2C]. Results reported are for a reduction of 50%, but the results are robust to a range of different damage values.

Graph theoretic metrics for structural connectivity

In order to assess how connectivity relates to change in complex dynamics, we assessed broad metrics of large scale connectivity using measures from graph theory assessed using the Brain Connectivity Toolbox (Rubinov and Sporns 2010):

Degree (D).

$$D_i = \sum_{j=1}^{N} C_{i,j}$$

The degree of each node within a weighted graph is defined as the sum of all directly connected edges to the node within the network. The mean Degree defines how strongly interconnected all nodes within the network are (Freeman 1987).

Characteristic path length (L).

$$L = \frac{\sum_{i,j \in V(C)} C_{i,j}}{\sum_{i,j \in V(C)} 1}$$

characteristic path length, defines the common length of paths ($V_{(C)}$) between each pair of nodesinnodes in a binary network <C>, weighted by the inverse of the weight of connectivity matrix (D) i.e. higher weight connections are interpreted as a shorter connection length. The mean of all path lengths forms the characteristic path length

Clustering coefficient (K).

$$K_i = \frac{2e_i}{k_i(k_i - 1)}$$

The weighted clustering coefficient of a node (K_i) is the average connection intensity of all "triangles" i.e. all neighbours (e_i) of a specific node which are also directly connect to each other as pairs (k_i) around a specific node. The average across each node (K_i) is used as a measure of network clustering (Watts and Strogatz 1998).

Small-Worldness (σ)

$$\sigma = \frac{K.\hat{K}^{-1}}{L.\hat{L}^{-1}}$$

Small-world networks have low characteristic path length and high clustering coefficient. An often-applied metric of 'small-worldness' - small world index (σ - SWI)

(Sporns 2006; Humphries 2008). Small worldness compares the path length (L) and clustering coefficient (K) to an equivalent measures of a suitable Erdös-Rényi random network (Humpries 2008) (ḱ and Ĺ repectively). If $\sigma > 1$, a network is considered small-world.

Computational simulation of neural dynamics [Figure 6.1B]

The activity of each of the 164 brain regions (which we define here as a node) is represented in our model as the phase of a single-phase oscillator over time. Phase at each node over time, is described by the Kuramoto equation presented in chapter 4 (Kuramoto 1984, Acebrón et al. 2005). For the work presented in this chapter, we fix the natural frequency to match known oscillations within the gamma frequency (w = 60Hz). The connectivity matrix <C> is a binary connectivity matrix determined by the empirical strength of white matter connections or lesioned using individual tract integrity data (see above). The distance matrix <D>, determined by the empirical length of connections between regions, imposes time delay on phase interactions between nodes. This is analogous to the simulation of a delay caused by neural conduction between regions of the brain. I introduce two control parameters to the coupling and delay of the network; the global coupling parameter (k), and mean global velocity <v> such that <C> = k<C> and <D>=<D>/v. The behavior of the Kuramoto model with respect to global Multistability and synchrony, by modulation of these parameters, has been explored previously (Cabral, Hughes, et al. 2011, Shanahan 2010b). The presence of multiple local maxima of both Multistability and synchrony within the <k,v> plane makes it hard to maximise though a simple gradient-decent optimisation approach. Therefore, we randomly selected 6000 pairs of model parameters within the <k,v> plane and tested the model for each repeat. I then used nearest neighbor interpolation to create the parameter space presented in [Figure 6.6].

Validation of computational simulation

To validate the computational model against empirical functional connectivity of the BOLD signal we followed the approach to simulating BOLD activity previously demonstrated in the literature (e.g.,(Cabral, Hughes, et al. 2011)), using the sine of the high-frequency activity of the Kuramoto Model as the neural input to the Balloon-Windkessel Haemodynamic model (Friston et al. 2000), low-pass filtered the resulting time courses at <0.25 Hz, and downsampled to 2 seconds. Unlike previous approaches that have assumed that the resultant spatio-temporal organisation of correlations within empirical BOLD time courses are univariate, we used an ICA approach to compare empirical BOLD activity with the output of our computational models. First, empirical BOLD time-courses were decomposed into 15 spatially independent-components using FMRIB Melodic (Smith et al. 2004, Beckmann et al. 2005). These components were then compared to the simulated BOLD components for each point in the parameter search (see above). Similarly, simulated BOLD time courses from the computational models were decomposed into 15 spatially independent time-courses. Spatial components from the empirical and modelled ICAs were then 'matched' using spatial correlation of their maps. Since the order of components extracted by MELODIC varies, we determined maximal correspondence between empirical and model components by calculating the pair-wise spatial correlation between functional connectivity maps for all pairs of components and reordering the resulting correlation matrix so as to maximize entries along the diagonal. An evaluation function was defined as the mean correlation between the empirical spatial maps and the modeled spatial maps for the top n (here n=5) matched components in the computational model compared to the empirical data, providing an objective measure by which the fit of individual regions of the global parameter space to empirical data may be compared against one another [Figure 6.6]. I present the results for ICA using 15 components in both empirical and modelled data, and n = 5; however, varying each of these parameters produces qualitatively similar results.

Measures of global and local network dynamics [Figure 6.1C]

To evaluate measures of network dynamics for both the empirical data and the computational model, we evaluated the phase history of the time courses for the 10 intrinsic connectivity networks (ICNs). The ICNs were estimated using MELODIC applied to the 164 region time courses extracted from an independent group of control subjects, as described earlier. For the purpose of estimating synchrony and Multistability within an ICN, a region was classified as part of an ICN if the value from the independent component was $z > 1.64$ (nominal $p > 0.05$).

Dynamics of phase timecourses for both the computational model and empirical fMRI data were evaluated, using the order parameters desribed in Chapter 4.

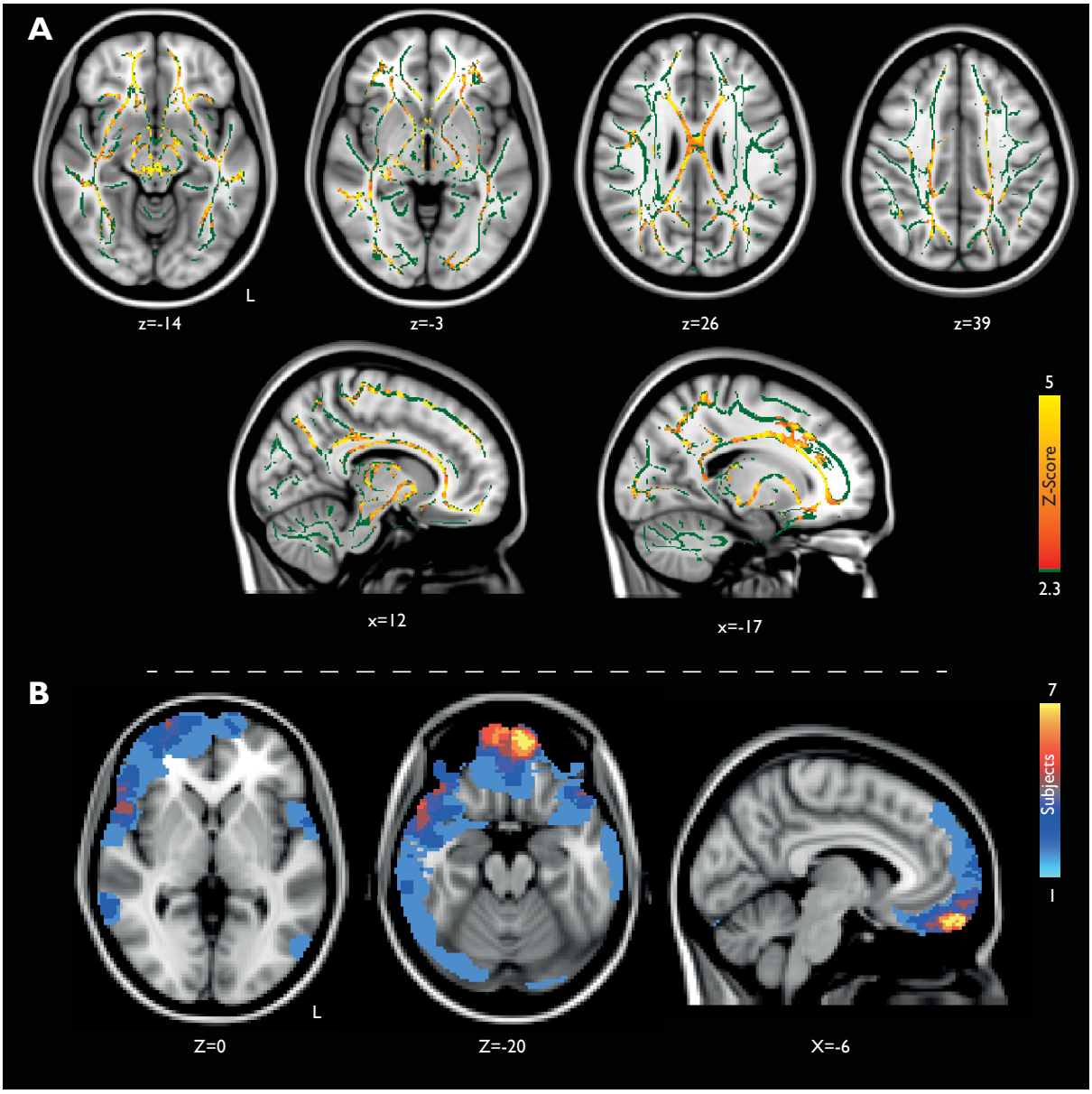

Figure 6.3 | Structural brain damage following traumatic brain injury. A) Widespread white matter disruption following traumatic brain injury measured by TBSS of Fractional anisotropy (FA). Contrasts between traumatic brain injury < healthy control subjects (Red-Yellow). Contrasts overlaid on a standard Montréal Neurological Institute 152 T1 1 mm brain and the mean fractional anisotropy skeleton (in green). Results are thresholded at $P \leq 0.05$, corrected for multiple comparisons using Threshold Free Cluster Enhancement (TFCE) (Smith et al., 2006). B) Lesion probability maps of cortical contusions across 63 TBI patients. Estimated by a neuroradiologist on the T1 structural images. The colour bar indicates the number of patients who had lesions at each site, overlaid on a standard Montréal Neurological Institute 152 T1 2 mm brain.

Results

Widespread disruption to the structural connectome after traumatic brain injury

To demonstrate that white matter connectivity is disrupted following TBI in the group of patients studied, we performed a standard tract-based spatial statistics (TBSS) analysis of 63 TBI patients and 26 aged-matched controls in order to compare integrity of major white matter tracts, measured by Fractional Anisotropy (FA). As both age and total grey matter volume likely influence white matter integrity, age and total grey matter volume were used as covariates of no interest. In the between-group contrast of Patients < Controls, there was widespread reduction in FA across the entire of the white matter skeleton [Figure 6.3A]. FA disruption was particularly pronounced in long-range inter-hemispheric fibres of the corpus callosum (where damage was widespread, but most extensive in the body and genu), and interhemispheric association fibres of the superior longitudinal fasiculus. Reduced FA was also pronounced within projection fibres of the corticospinal tract, and the anterior and posterior limbs of the internal capsule. Additionally, a strong reduction of FA was observed within the fornix and corona radiata. This distribution of widespread changes to white matter integrity is typical of injury following TBI and is consistent with our previous TBSS based findings (Kinnunen et al. 2011).

To explore how network level measures of structural connectivity are changed following TBI, we tested for associations between large-scale structural connectivity measures (from Graph Theory) in TBI patients and aged-matched controls. To define structural connectivity in TBI patients and age-matched controls, we started by defining the probable location of each of the connecting white matter fibres in an independent group of 10 age-matched healthy control subjects. This resulted in a binary reference connectivity matrix. I then projected thresholded versions of these maps for each edge in the reference connectivity matrix through the TBSS skeleton of the patient

and control group to generate a 164 region tract integrity matrix for each patient and control. The tract integrity matrix was then used to 'damage' the reference matrix leading to a single weighted connectivity matrix for each subject, we then calculated various graph theoretic measures in all subjects. There was a significant reduction (in patients compared to controls) in small-worldness measured by small world index in (t_{87}=-3.70, p<0.01), clustering coefficient (t_{87}=-2.84, p<0.01) and mean degree (t_{87}=-3.42, p<0.001). In addition, patients had a significantly higher characteristic path length compared to healthy controls (t_{87}=2.84, p<0.01).

Multistability of large-scale neural dynamics is reduced following traumatic brain injury

I assessed the Multistability of large-scale neural dynamics following traumatic brain injury (TBI), measured using resting-state fMRI data in both patients and controls

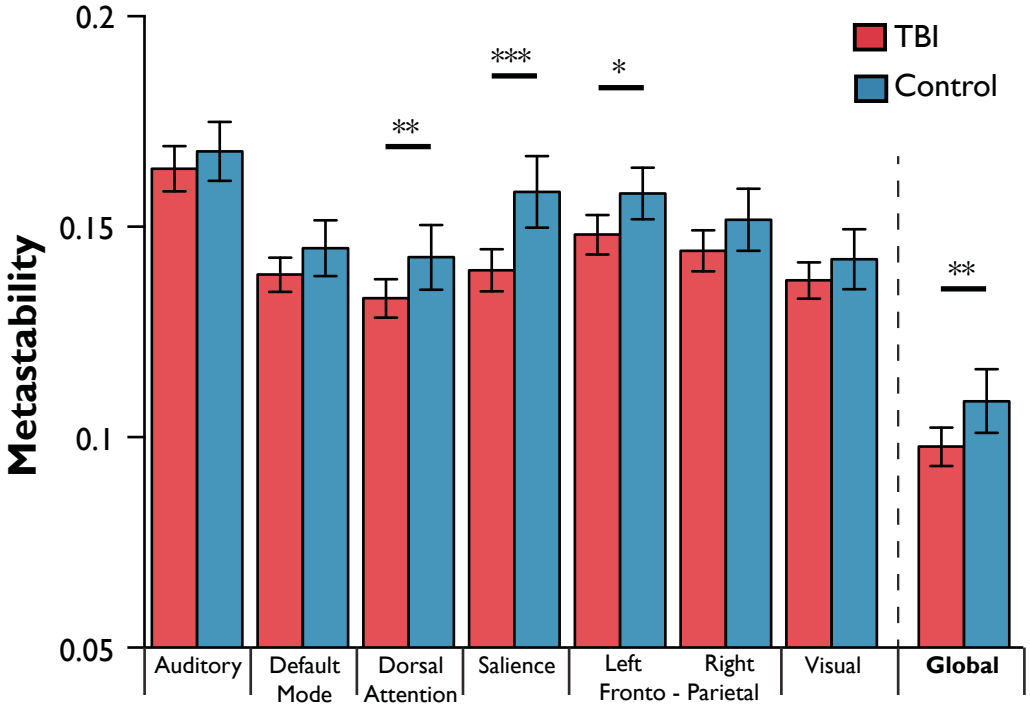

Figure 6.4 | Empirical Multistability at rest is significantly reduced in Patients compared to controls. Mean measures of Multistability (±1SEM) estimated using phase transformed functional time-course extracted from 63 Patients and 26 Control subjects suggest that global measures of Multistability are reduced following TBI.

[Figure 6.1A]. I sampled the fMRI blood-oxygen-level dependent (BOLD) timecourses from 164 cortical and subcortical anatomical regions. Within each subject, the BOLD timecourses were band-passed to 0.01-0.2Hz and the Hilbert transform used to identify the phase of the signal. I then calculated Multistability across all phase timecourses (i.e. global Multistability). In addition to the global measures, we explored Multistability within intrinsic connectivity networks, by restricting analysis to subsets of nodes belonging to intrinsic connectivity networks defined by an Independent component analysis (ICA) of functional time-courses extracted from an independent group of healthy control subjects. Next we fitted the general linear model to measures of global and network level dynamics with age and total grey matter volume and average framewise displacement estimated from the fMRI data as covariates of no interest.

Global Multistability was significantly reduced in TBI patients compared to controls (t_{84}=-2.63, $p<0.05$ 1-tailed), [Figure 6.4]. Patients also showed lower Multistability in the salience network (t_{84} = -3.68 $p<0.001$), a left fronto-parietal network (t_{84} = -2.41, $p<0.02$) and dorsal attention network (t_{84} = -2.27, $p<0.05$); these survive multiple comparison correction by FDR ($q<0.1$). A potential confound for measuring widespread neural dynamics in the TBI patient population is the presence of cortical contusions. Thirty-two patients in the TBI group were found to have focal gray matter lesions, suggestive of cortical contusions, on T1-weighted structural imaging. It is possible that these lesions affected the BOLD time courses extracted and the resulting Multistability calculations. I therefore repeated the calculation of global Multistability after removing brain regions whose anatomical segmentation overlapped with focal lesions in any patients [Figure 6.3B] (i.e., time courses from affected regions were not analysed in any patients or controls). Changes to global Multistability in TBI patients compared to controls following this adjustment were similar to the full brain analysis (t_{84}=-2.63 $p<0.01$).

Multistability after traumatic brain injury predicts cognitive performance

To investigate whether measures of global Multistability relate to the cognitive impairments seen in the TBI population, we regressed measures of Multistability against measures of cognitive flexibility, associative memory, and information processing speed, including age and mean absolute movement during the fMRI run as covariates of no interest [Figure 6.5]. Cognitive flexibility was measured using the Trail Making Test switch cost index (SCI), a measure of task-switching, previously demonstrated to be impaired following TBI (Jilka et al. 2014). Associative memory was assessed using the immediate recall and retention measures of the People and Doors Test (see Materials and Methods). Information processing speed was assessed in 49 of the 62 patients with neuropsychological assessments using the Choice Reaction Task, median reaction time. In patients, there was a significant negative relationship between global Multistability and SCI (t_{58}=-2.21, $p<0.05$, [Figure 6.5, Top]) and median reaction time (t_{44}=-3.46, $p<0.01$, [Figure 6.5, Middle]). Global Multistability was positively related to immediate recall, i.e. improved performance (t_{58}=2.49, $p<0.05$, [Figure 6.5, Bottom]), and retention (t_{58}=2.780, $p<0.01$, [Figure 6.5 , Bottom]). These results were from a multiple regression model containing age, motion and total grey matter volume as covariates of no interest. The reported results survive multiple comparison correction FDR, $q<0.1$

A computational simulation of large-scale neural dynamics resembles empirically-defined intrinsic connectivity networks

In order to build a computational model to explore how multistable neural dynamics responds to structural disconnection (e.g. TBI), we started by defining a large-scale computational model of the healthy brain at rest, based on the structural connectivity between 164 regions of the brain defined using white matter tractography, which we

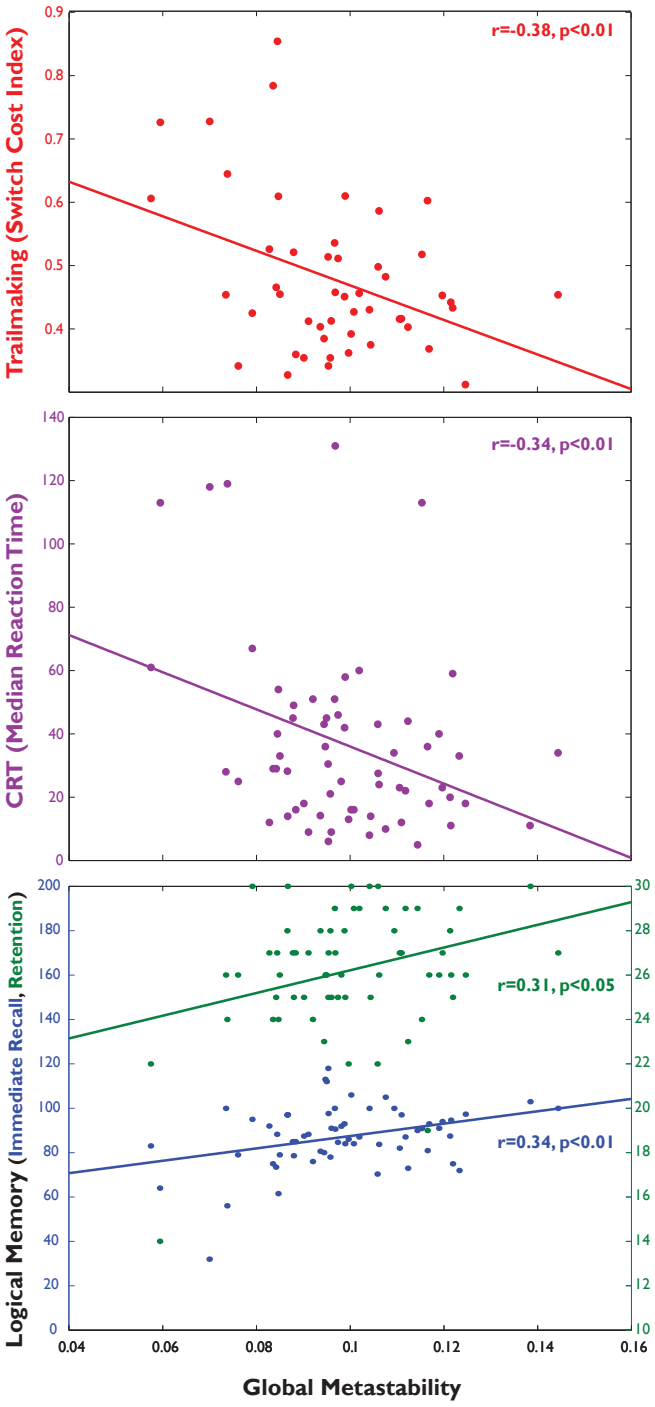

Figure 6.5 | Global Multistability predicts behavioural outcome. Measures of global Multistability during rest significantly correlate with scores of task-switching (Top, Red n=62), Information Processing speed (Middle, Purple, n=49), and Logical Memory (Bottom, Blue and Green, n=62).

validated using resting-state functional connectivity.

The model we used was the Kuramoto model, a coupled oscillator system (Acebrón et al. 2005) shown to be able to simulate large-scale neural dynamics related to underlying structural connectivity (Cabral, Hughes, et al. 2011, Hellyer et al. 2014, Shanahan 2010b, Messe, Benali, and Marrelec 2014). I defined our 164-region model such that each node corresponds to activity at one of the 164 anatomical regions used in the empirical analysis. Coupling between nodes was defined by the structure of the white matter connectivity of the brain. Previous work has explored the dynamics of the Kuramoto model in relation to the strength and structure of coupling between nodes (Cabral, Hughes, et al. 2011, Cabral et al. 2012, Shanahan 2010b, Wildie and Shanahan 2012). This work suggests that the model behaviour is highly sensitive to two constants, the global coupling parameter (K) and mean global velocity , which is determined by a distance matrix . In order to understand the effects of these constants on our 164 node model, we performed a parameter space search using 6000 randomly generated pairs of parameters , within the plane and . In the parameter search, we used the binary reference connectivity matrix defined from a group of independent healthy controls. The behaviour of Multistability as well as global synchrony of the system as a function of K are shown in [Figure 6.6]. I observed that for increasing values of K, the system tends towards maximum global synchrony, after passing through an intermediate phase where Multistability is maximal. To reduce the complexity of further computations, we selected a point in the dimension based on plausible physiology, such that =11ms-1, following (Cabral, Hughes, et al. 2011) .

For the model output for each pair, we used independent component analysis (ICA) to decompose the 164 node timecourses into a set of independent clusters of nodes. This set of clusters was then correlated with a set of resting-state networks derived from the empirical BOLD fMRI resting state data in the same 10 independent healthy control subjects used in the tractography step (see materials and methods). I found that the correlation between the simulated and empirically defined clusters was

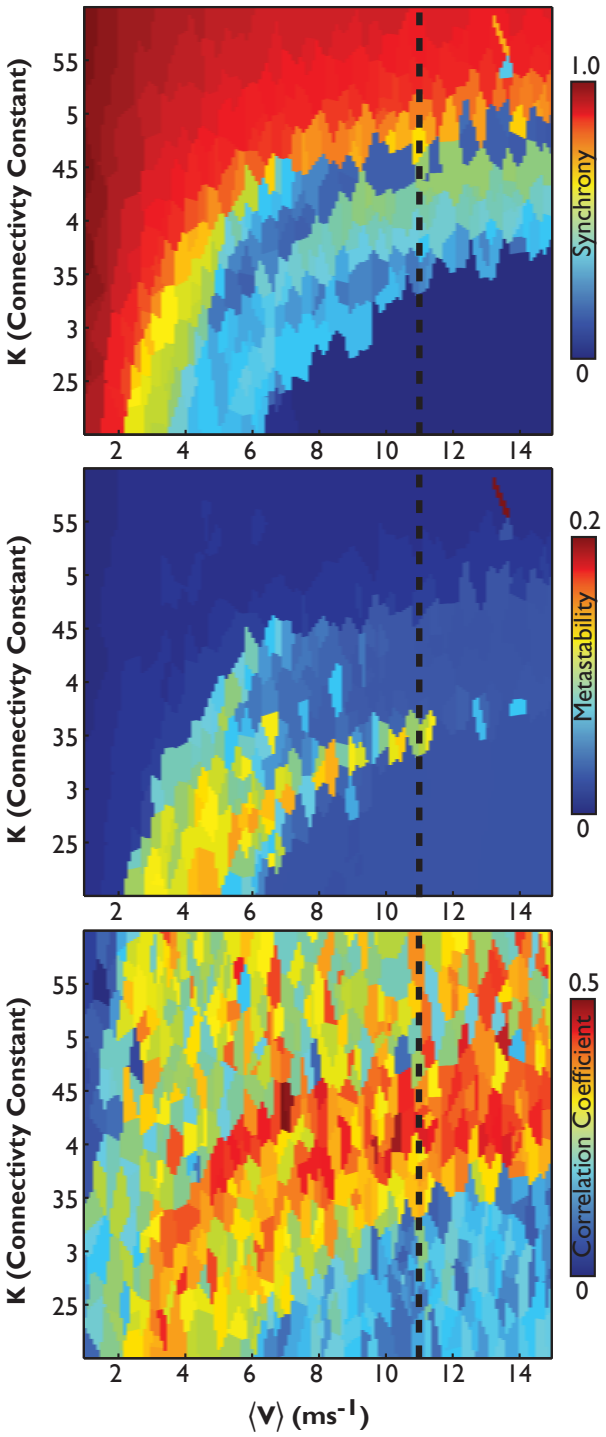

Figure 6.6 | A large-scale neural network model predicts functional connectivity where Multistability is maximised. Plots of a parameter space exploration of the Kuramoto Model the using 6000 randomly generated pairs of the coupling and delay parameters <k,v>, within the plane $k_{(1...6)}$ and $V_{(1...16)}$, here expressed as mean velocity (ms-1). Global Syncrony (Top). Global Multistability (Middle), and Correlations of the 5 best-matching simulated and empirical ICNs (Bottom). For ease of further computation we set velocity at a biologically plausible value (Cabral et al., 2011a), which equates to ~ 11ms-1 (dashed line)

maximal near the point of maximal Multistability [Figure 6.6].

Empirically-defined large-scale structural disconnection leads to reduced Multistability in a simulation of large-scale neural dynamics

To examine the effect of large-scale structural disconnection following TBI on simulated neural dynamics, we used individualised structural connectivity matrices in patients and controls (see Materials and Methods, [Figure 6.2C]) to define coupling within the Kuramoto model [Figure 6.1B]. Global Multistability was calculated for simulations of the model executed separately for each subject's connectivity matrix. Runs were repeated for a range of values of the coupling constant, K [Figure 6.7, Left]. The region of maximum Multistability in healthy controls was identified within the parameter search (K=3.5, see above). In this region, global Multistability was significantly reduced in patients compared to controls (t_{84}=-4.90, p<0.0001) [Figure 6.7, Right]. To further explore the effect of structural disconnection on simulated dynamics, we applied the same analysis to compute Multistability within subsets of regions involved in canonical ICNs. Simulations using structural connectivity from individual TBI patients

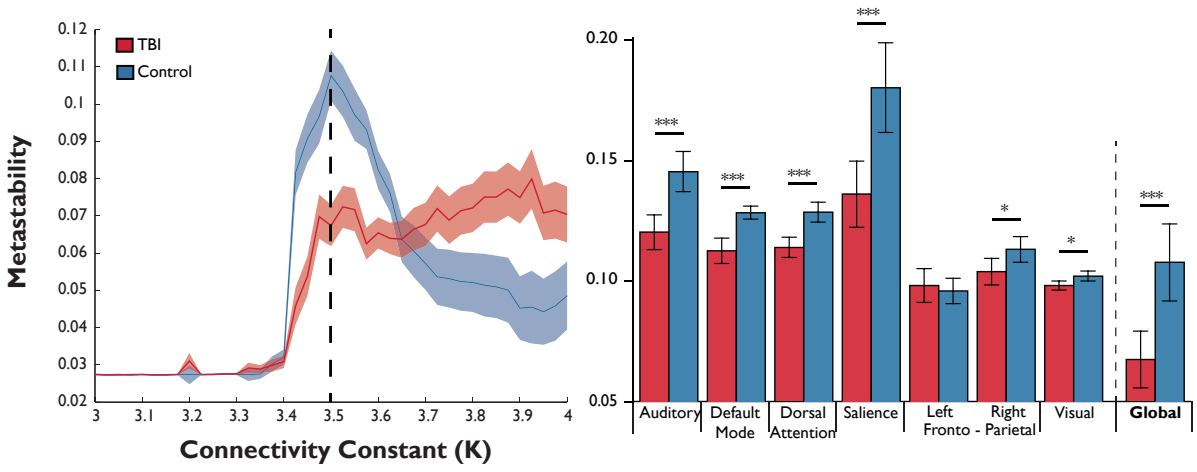

Figure 6.7 | Global Multistability is decreased in TBI patients compared to controls A, Mean Multistability (±1SEM) for in patients (n=63) and controls (n=26) in the computational model for a range of different coupling strengths (K). v = 11ms -1. B, Mean measures of Multistability estimated within the model (±1SEM) for 63 patients and 26 healthy control subjects suggest that global measures of Multistability simulated from structural connectivity in TBI patients are reduced compared to healthy controls.

had significantly lower Multistability within the dorsal attention network (t_{84}=4.15, p<0.001), a right fronto-parietal network (t_{84}=-1.99, p<0.05), default mode network (t_{84}=-3.75, p<0.001), salience network (t_{84}=-3.62, p<0.001), primary auditory (t_{84}=-4.06, p<0.001) and low-level visual networks (t_{84}=-2.45, p<0.02). Simulated results are obtained from multiple regression using age and total grey matter volume as covariates of no interest and are corrected for multiple comparisons; FDR, q<0.1

To evaluate the extent to which global Multistability in the simulation is determined by changes to large-scale structural connectivity, we used linear regression with graph theoretical measures and subject group as a covariate, to reveal associations between empirically derived graph theoretical metrics and simulated Multistability. Small world index (t_{84}=5.62, p<0.001), clustering coefficient (t_{84}=7.75, p<0.001) and mean degree (t_{84}=7.77, p<0.001), were significant positive predictors of simulated global Multistability. An increase in characteristic path length is associated with reduced Multistability (t_{84}=-4.162, p<0.001).

Discussion

I considered two interrelated questions that are fundamental to understanding the brain: how does high-level behaviour arise from the structural connectivity of the brain; and how does disruption of network structure alter behaviour? Multistability has been suggested as a fundamental property for understanding complex neural dynamics, and serves as an important conceptual bridge between brain structure and behaviour (Tognoli and Kelso 2014). Here, we used traumatic brain injury (TBI) as a model with which to interrogate the relationship between multistable dynamics, structural connectivity and behaviour. I found that following TBI, Multistability measured using fMRI is reduced compared to age-matched healthy control subjects. Furthermore, the level of Multistability relates to behavioral impairment on a range of cognitive tasks. Importantly, using a combined empirical and computational modelling approach, we demonstrate that the reduction in Multistability following TBI is associated with the disruptive effects of disconnection of structural network topology, providing a clear demonstration of how emergent multistable dynamics relate to behaviour through structural connectivity.

Diffuse axonal injury (DAI) is a common pathology documented in all severities of TBI (Adams et al. 1989), thought to account for much of the morbidity and mortality after injury (Adams et al. 1989, Geddes et al. 1997). DAI preferentially damages the long-distance white matter tracts that connect brain regions, and produces a reduction in small-world topology (Caeyenberghs et al. 2014, Caeyenberghs, Leemans, Leunissen, et al. 2012, Caeyenberghs, Leemans, De Decker, et al. 2012, Pandit et al. 2013). I demonstrate a significant reduction in the 'small-worldness' of the structural connectivity in TBI patients compared to controls, alongside a reduction in Multistability. Previously, the relationship between network topology and Multistability has been shown in computational simulations (Shanahan 2010a, Wildie and Shanahan 2012). Our computational findings, backed up by empirical observation provide further support for a relationship between small-world topology and multistable dynamics in

the brain. This structure-function link is intuitive, given that small-worldness facilitates both segregation (nodes of the brain showing a modular architecture) and integration (short path lengths between nodes) (Bassett and Bullmore 2006, Watts and Strogatz 1998).

Our modelling results provide support for the empirical findings by demonstrating that alterations in structural topology consistent with disconnection caused by TBI effect reduced levels of simulated Multistability. This provides a mechanistic link between reduction in small-worldness and neural dynamics. The results of the simulations are consistent with other computational models based on abstract network architectures (Shanahan 2010a, Friston 1997) as well as those defined by anatomical connectivity (Cabral, Hugues, et al. 2011, Deco, Jirsa, McIntosh, Sporns, and Kötter 2009). This previous work has shown how network topology is fundamental to emerging Multistability, and has implicated sparseness (Friston 1997) and small-worldness (Wildie and Shanahan 2012, Shanahan 2010a, Cabral, Hugues, et al. 2011, Cabral et al. 2012, Messe, Benali, and Marrelec 2014). More recently, neural dynamics consistent with Multistability have been shown to emerge when the network structure has a "rich-club" organization (Senden et al. 2014). Future work could explore in more detail whether other graph theory properties better explain the alterations in Multistability that we observed, leading to a more refined explanation of how complex neural dynamics emerge from the network topology of the brain.

Our empirical results are based on functional imaging acquired during rest. The resting state, with the absence of any explicit behavioural requirements, is one where Multistability is likely to be best suited to efficient cognitive flexibility, e.g. to retain information and flexibly react to the environment. Rest, which must be distinguished from low arousal states such as sleep or sedation, can be thought of as a "jack-of-all-trades" state in which the brain is in a broad exploratory regime. The dynamical regime of the resting state may constitute an upper limit for flexibility of the neural dynamics of the brain. I have previously shown, with both empirical and computational

approaches, that Multistability at rest is higher than during a focused cognitive task (Hellyer et al. 2014). During a task, high Multistability is less desirable, since a specific configuration of brain systems is recruited (e.g., in coordinating specific visual and motor systems to perform a visually cued motor task). However, the dynamical regime during this task will still reflect the level of Multistability at rest, both in terms of how the system can transition from rest to a task state efficiently and reliably. With low Multistability at rest (e.g following TBI), the system is likely to take longer to and be less reliable at transitioning between cognitive states, and show a reduced repertoire of brain configurations required to effectively facilitate sustained task performance.

I found reduction in Multistability related to cognitive impairments on three tasks assessed: cognitive flexibility, speed of information processing and associative memory. The switch cost index of the Trail Making Test, which involves rapidly and accurately switching between competing task demands, assesses cognitive flexibility and intuitively maps onto reduced Multistability (which reflects reduced dynamical flexibility). This relationship offers a potential mechanism for perseverance following TBI: structural damage to white matter tracts, limits the Multistability of the brain which, in turn, limits cognitive flexibility. However, the relationship between Multistability and behaviour was not specific to cognitive flexibility, but was also present for the other two measures tested. Notably, all three tasks involve the integration of information across large-scale brain networks sustained over an extended period of time (e.g., memory (Spreng et al. 2010), CRT (Bonnelle et al. 2011) and cognitive flexibility (Jilka et al. 2014, Sharp et al. 2010, Erika-Florence, Leech, and Hampshire 2014)). All of these tasks, therefore, require coordinated communication between sensory, motor and cognitive control brain regions, and so altered global Multistability might plausibly be expected to affect them all. However, there may be different ways that Multistability can break down, evident as altered dynamics within specific brain networks, resulting in different profiles of impairments. I found some evidence for this in the different patterns of individual network Multistability and how they relate to

neuropsychological score; for example, changes in associative memory were related to Multistability within the DMN. Future work, with a larger group of patients and imaging with higher temporal resolution would enable a better characterization of both across-subject variance in network Multistability and the patterns of behavioural impairment. Ultimately, information about altered neural dynamics could provide a sensitive biomarker to stratify patients and therefore be used to design targeted, individualized treatments, which may involve electrical stimulation, pharmacological intervention or neurofeedback (Sharp, Scott, and Leech 2014).

There are a number of limitations to the work. The constraints inherent in tractography using diffusion MR mean that the structural connectivity matrices and graphs generated were undirected, in so much as feed-forward and feed-back connectivity of individual regions had a uniform effect on node-node functional interaction, which is unlikely to be the case in vivo. In addition, long distance connections, for example inter-hemispheric pathways, may be difficult to resolve accurately since uncertainty in streamline location increases with the length of the tract (Jones 2010a, b). The computational model we have used is obviously a dramatic simplification of brain function. For example, the simulation is built on a relatively (compared to the brain) low-dimensional connectivity matrix comprised of 164 regions. However, despite these limitations, the simulation provides important insights into the relationship between brain structure and function and is consistent with the empirical findings. Such models, at least at the level of global network dynamics, replicate the broad changes in BOLD seen with fMRI, even though the model is based on nothing more than the network topology (Cabral et al. 2012, Cabral, Hugues, et al. 2011, Deco, Jirsa, McIntosh, Sporns, and Kotter 2009, Deco et al. 2008, Messe, Benali, and Marrelec 2014), with no modelling of the functional specialisation of individual nodes (i.e., all nodes are functionally equivalent). These limitations mean that precise, quantitative comparisons between the simulations and the brain were not expected. Difficulties with the measurement of BOLD fMRI signal, such as partial volume effects,

regional differences in vascular reactivity or susceptibility artefacts would also make quantitative comparisons challenging.

In summary, we found that large-scale structural disconnection in the brain is associated with reduced Multistability, linked to impaired cognitive flexibility and other behavioural impairments. The link between damage to the structural connectivity following TBI and reduced Multistability (demonstrated both in empirical and simulated data) provides evidence that Multistability is contingent on the integrity of the underlying structural network topology. This suggests a mechanistic link between structure, neural dynamics and behaviour. The results indicate a compelling link between brain structure and function, and suggest the framework of multistable dynamics offers an account for understanding the brain in health and disease.

"Rabbit's clever," said Pooh thoughtfully.
"Yes," said Piglet, "Rabbit's clever."
"And he has Brain."
"Yes," said Piglet, "Rabbit has Brain."
There was a long silence.
"I suppose," said Pooh, "that that's why he never understands anything."

-- A.A. Milne,

Summary and concluding remarks

7

The research in this thesis investigated how normal cognitive functioning in the human brain depends on underlying white matter structure. By examining this network structure in the normal brain, and its disruption after TBI, I explored complex measures of neural activity, such as Multistability, emerging out of white matter structural connectivity in the brain, and their modulation by cognition and pathology. The key aims of the thesis were to explore:

- the effect of structural disconnection on cognitive function;
- the modulation of complex neural dynamics by cognitive state;
- how structural connectivity of the brain confers cognitive flexibility through multistable dynamics;
- how damage to connections feeds through into altered dynamics, and

how this may relate to cognitive state.

In Chapter 3 I demonstrated that white matter structural connectivity, as defined by diffusion tensor imaging, is an important diagnostic marker and predictor of prognosis following TBI. Machine learning approaches applied to DTI data were used to diagnose white matter damage and to predict neuropsychological outcome in individual patients. Pattern classifiers were used to predict the presence of white matter damage in 25 patients following TBI, each with evidence of microbleeds indicating TAI, compared to neurologically healthy age-matched controls. These classifiers were then applied to 35 additional patients with no conventional imaging evidence (the presence of microbleeds) of TAI. Finally, regression analyses were used to predict indices of neuropsychological outcome for information processing speed (IPS), executive function (EF) and associative memory in a group of 70 patients forming a heterogeneous group in terms of the severity of the initial trauma and the abnormalities evident on diagnostic imaging. The classifiers discriminated between patients with microbleeds and age-matched controls with a high-degree of accuracy, and outperformed other methods. When the trained classifiers were applied to patients without microbleeds, patients with probable axonal injury showed evidence of greater cognitive impairment in information processing speed and executive function. The classifiers were also able to predict the extent of impairments in information processing speed and executive function. Therefore, this work provided proof-of-principle evidence that multivariate techniques can be used with DTI to provide diagnostic information about clinically significant TAI. This work extends previous group-wise demonstrations of white matter damage measured using DTI (Sharp et al. 2014), and provides a new approach to detrmining white matter damage in individual patients. Importantly, it was demonstrated that white matter damage (structural disconnection) is associated with poor cognitive outcome in the domains of information processing and cognitive flexibility. Understanding how disconnection following TBI interacted with functional activity within the brain to affect such cognitive change was the main

focus of the following chapters. To determine this involved developing simulations of neural dynamics, to relate brain structure with brain function and so explore the effects of post-traumatic white matter damage.

In Chapter 4, I introduced a computational model of the brain, based on a network of coupled Kuramoto oscillators was simulated. This simulation modelled the communication between pairs of individual brain regions, using the strength of the known structural connectivity of the brain estimated from published data on diffusion spectrum imaging (DSI). Each of the connections was subject to a time delay, based on the traversal distance of the white matter tractography. These models have previously been used to model whole brain functional connectivity (Cabral et al. 2011 , Cabral et al. 2012). Importantly, by tuning key parameters of the model, the dynamics were shown to take on a range of different properties, from fully synchronous to chaotic dynamics. Tuning these parameters provided the opportunity to observe a second order phase transition within the dynamics of the model, such that the neural dynamics are poised simultaneously between order and chaos. In such a position, the model exhibits high Multistability. Within this region of multistable activity, the functional interactions imposed on neural dynamics by structural connectivity produced connectivity strongly resembling empirical resting state connectivity. This work demonstrated that simple simulations can capture important aspects of both dynamics and empirical functional connectivity, forming the starting point for exploring simulated cognitive and pathological states.

In chapter 5, the computational framework demonstrated in the previous chapter was used to examine complex dynamical activity within the brain, and how this may relate to cognitive state. The relationships between brain network activity, Multistability and cognitive state in humans, were investigated, testing the hypothesis that global Multistability is 'tuned' by network interactions. Two conditions were studied: 1) an attentionally demanding choice reaction time task (CRT); and 2) an unconstrained 'rest' state. Functional MRI demonstrated that increased synchrony and decreased

Multistability were associated with increased activity within the Fronto-Parietal Control/ Dorsal Attention Network (FPCN/DAN) activity and decreased DMN activity during the CRT compared to 'rest'. Activation of the FPCN/DAN increased global synchrony and decreases Multistability. DMN activation had the opposite effects. These results suggest that the balance of activity in the FPCN/DAN and DMN might control global Multistability, providing a mechanistic explanation of how attentional state is shifted between an unfocused/exploratory mode characterized by high Multistability, and a focused/constrained mode with low Multistability. This provided a novel insight into how cognitive flexibility may emerge from the structural connections of the brain through multistable dynamics.

In chapter 6, these different strands of research were drawn together, by relating structural damage, neural dynamics and cognition to explore how cognitive flexibility is shaped by the underlying human connectome. Complementary empirical and computational approaches investigated how Multistability is affected by structural disconnection following TBI, and how this may affect cognitive impairment. There was reduced Multistability in large-scale neural dynamics following TBI, as assessed with resting-state fMRI. This reduction in Multistability was associated with damage to the connectome, evident from the DTI data. Furthermore, decreased Multistability was associated with reduced cognitive flexibility and information processing speed. The computational simulation demonstrated how behaviourally relevant changes in neural dynamics result from structural disconnection. The findings indicate that multistable dynamics are important for normal brain function and are contingent on the structure of the human connectome. Understanding this relationship will prove useful in understanding how the pathology of TBI leads to behavioural and cognitive impairment

In chapters 4 through 6, I briefly discuss how the results presented relate to a growing literature that attempts to descibe the brain as a 'critical' system. It is important to note several difficuties with this approach to exploring neural dynamics. Whilst evidence

for critical dynamics in the brain is ever expanding (Beggs and Plenz 2003, Beggs and Plenz 2004, Kitzbichler et al. 2009, Chialvo 2010, Haimovici 2013), and undoubtedly, provides a rich framework that provides a range of theoretical advatages to a neural system (Shew 2012) which are compatable with the brain as a multistable system (Shanahan 2010a, Friston 1997, Tognoli and Kelso 2014, Kelso 2012, Bressler and Kelso 2001), it is important to note that multi-stable activity may occur in the absence of a 'critical' regime. For example, properties such as scale invariance characteristic of the critical regime, are not necessary or indeed sufficient for metastable activity. Thus the interpretation that multistable operations are an underpinning mechanism which relates criticality to behaviour, should be taken with some degree of caution. Indeed whilst criticality may provide an interesting theoretical framework which describes some aspects of the organisation of neural dynamics (particually in the resting state), understanding how critical dynamics relates to not only to the structure of the brain but also behaviour is important indeed our recent work (Fagerholm 2015), in tandem with the work presented in this thesis, provides evidence across multiple different spatial and tempioral scales, that focussed attention is able to modulate signatures of criticality and multi-stability driving the brain into a 'subcritical' state, dependant on cognitive state, this suggests the possibiity that the behaving brain is not 'critical' at all. Future work, synthesising these observations in a range of behavioural states is needed to draw this exciting field of research away from the epiphenominal observation of self-organised critical activity in the resting brain to understanding how, if and why organisation of the brain as a critical system is useful to behavioural activity in the brain.

Future Directions

There are two broad areas to explore in research arising from the work presented in the thesis. One is to develop the computational approaches to provide more comprehensive descriptions of the brain. The Kuramoto simulations are only one way of exploring the interaction between brain regions. In the present model, all connections are essentially excitatory, whereas in reality the function of individual connections are also defined by many receptor types present at the synapse (Palomero-Gallagher et al. 2009). The important neuromodulatory effects of dopamine, serotonin, etc. were not modeled. Equally, whilst the Kuramoto model that was employed operated only at one fast timescale, constrained by the range of natural frequencies selected for each node, the effects demonstrated by the network simulations need to be developed reflect multiple different timescales present in empirical data acquired with different techniques; for example, fast gamma-band measured with EEG and the slow components of the fMRI BOLD signal. Therefore, future work should examine dynamics revealed by simulations applied to a range of empirical neuroimaging data at a range of spatial and temporal scales, using models capable of simulating a wider range of neural and cognitive data. They may incorporate a variety of biological constraints, including both region-specific neural organization, such as the presence or absence of cortical columns, the distribution of particular neurotransmitter pathways, and local receptor densities (Amunts et al. 2000, Palomero-Gallagher et al. 2009).

The other broad area for future research is to explore how computational models could help in clinical applications, to assess the distribution and severity of pathology and how this may impact on rehabilitation. It is increasingly recognised that neuroscientists, neurologists and psychiatrists need to not only acquire more empirical data about neurological and psychiatric disorders, but also to integrate this data into detailed computational theories that can inform treatment (Stephan and Mathys 2014, Montague et al. 2011). In this context, the work presented in this thesis offered an example of applying computational simulations to capture the interactions between

pathology, neural patterns and dynamics following TBI and their impact on behaviour. More sophisticated mechanistic explanations linking structure, neural dynamics and impaired cognition will be important in delivering: (1) detailed predictions about the clinical consequences of TBI and other brain disorders; (2) providing practical biomarkers for patient stratification in treatment trials; (3) and developing novel hypotheses about novel behavioural, pharmacological and electrophysiological interventions (Sharp, Scott, and Leech 2014). As an example, validated computational simulations will provide a method for efficiently exploring and testing many different possible intervention strategies (Stephan and Mathys 2014) in order to select the most effective treatment. This may extend to determining the optimal treatment for individual patients; for example, transcranial direct current stimulation has the potential for improving rehabilitation, but understanding the frequency and the site of its application to achieve the best result presents a major challenge. This may prove impossible to determine by classic trial methodology, leading to rejection of a potentially useful intervention, but are questions that may be answerable by computational simulations based on observational studies on brain structure and function.

"Any man who reads too much and uses his own brain too little falls into lazy habits of thinking."

-- Albert Einstein

Bibliography

Acebrón J, Bonilla L, Pérez Vicente C, Ritort F, Spigler R (2005) The Kuramoto model: A simple paradigm for synchronization phenomena. Reviews of Modern Physics 77:137-185.

Achard S, Salvador R, Whitcher B, Suckling J, Bullmore E (2006) A resilient, low-frequency, small-world human brain functional network with highly connected association cortical hubs. The Journal of neuroscience : the official journal of the Society for Neuroscience 26:63-72.

Adams JH (1982) Diffuse axonal injury in non-missile head injury. Injury 13:444-445.

Adams JH, Doyle D, Ford I, Gennarelli TA, Graham DI, McLellan DR (1989) Diffuse axonal injury in head injury: definition, diagnosis and grading. Histopathology 15:49-59.

Alexander DC (2005) Maximum entropy spherical deconvolution for diffusion MRI. Inf Process Med Imaging 19:76-87.

Allen EA, Damaraju E, Plis SM, Erhardt EB, Eichele T, Calhoun VD (2014) Tracking whole-brain connectivity dynamics in the resting state. Cerebral cortex 24:663-676.

Amunts K, Malikovic A, Mohlberg H, Schormann T, Zilles K (2000) Brodmann's Areas 17 and 18 Brought into Stereotaxic Space---Where and How Variable? NeuroImage 11:66--84.

Ances BM, Sisti D, Vaida F, Liang CL, Leontiev O, Perthen JE, Buxton RB, Benson D, Smith DM, Little SJ, Richman DD, Moore DJ, Ellis RJ (2009) Resting cerebral blood flow: a potential biomarker of the effects of HIV in the brain. Neurology 73:702-708.

Andersson J, Jenkinson M, Smith SM (2007) Non-linear registration, aka spatial normalization: FMRIB technical report TR07JA2. FMRIB Analysis Group ….

Arfanakis K, Haughton VM, Carew JD, Rogers BP, Dempsey RJ, Meyerand ME (2002) Diffusion tensor MR imaging in diffuse axonal injury. AJNR 23:794-802.

Assaf Y, Pasternak O (2008) Diffusion tensor imaging (DTI)-based white matter mapping in brain research: a review. J Mol Neurosci 34:51-61.

Azouvi P, Couillet J, Leclercq M, Martin Y, Asloun S, Rousseaux M (2004) Divided attention and mental effort after severe traumatic brain injury. Neuropsychologia 42:1260-1268.

Baddeley AD, Emslie H, Nimmo-Smith I (1994) Doors and People Test: A Test of Visual and Verbal Recall and Recognition. Bury-St-Edmunds: Thames Valley Test Company.

Basser PJ, Pierpaoli C (1996) Microstructural and physiological features of tissues elucidated by quantitative-diffusion-tensor MRI. Journal of magnetic resonance Series B 111:209-219.

Basser PJ, Pierpaoli C (1998) A simplified method to measure the diffusion tensor from seven MR images. Magnetic Resonance in Medicine 39:928-934.

Basser PJ, Mattiello J, LeBihan D (1994) MR diffusion tensor spectroscopy and imaging. Biophysical journal 66:259-267.

Basser PJ, Pajevic S, Pierpaoli C, Duda J, Aldroubi A (2000) In vivo fiber tractography using DT-MRI data. Magnetic Resonance in Medicine 44:625-632.

Bassett DS, Bullmore E (2006) Small-world brain networks. Neuroscientist 12:512-523.

Bassett DS, Bullmore ET, Meyer-Lindenberg A, Apud JA, Weinberger DR, Coppola R (2009) Cognitive fitness of cost-efficient brain functional networks. Proc Natl Acad Sci U S A 106:11747-11752.

Beauchamp MH, Ditchfield M, Babl FE, Kean M, Catroppa C, Yeates KO, Anderson V (2011) Detecting traumatic brain lesions in children: CT versus MRI versus susceptibility weighted imaging (SWI). Journal of neurotrauma 28:915-927.

Beaulieu C (2002) The basis of anisotropic water diffusion in the nervous system - a technical review. NMR Biomed 15:435-455.

Beckmann C, Mackay C, Filippini N, Smith S (2009) Group comparison of resting-state fMRI data using multi-subject ICA and dual regression. In: 15th Annual Meeting of Organization for Human Brain Mapping, pp poster 441 SU-AM.

Beckmann CF, Jenkinson M, Smith SM (2003) General multilevel linear modeling for group analysis in FMRI. Neuroimage 20:1052-1063.

Beckmann CF, DeLuca M, Devlin JT, Smith SM (2005) Investigations into resting-

state connectivity using independent component analysis. Philos Trans R Soc Lond B Biol Sci 360:1001-1013.

Beggs JM (2008) The criticality hypothesis: how local cortical networks might optimize information processing. Philosophical transactions Series A, Mathematical, physical, and engineering sciences 366:329--343.

Beggs JM, Plenz D (2003) Neuronal avalanches in neocortical circuits. J Neurosci 23:11167-11177.

Beggs JM, Plenz D (2004) Neuronal avalanches are diverse and precise activity patterns that are stable for many hours in cortical slice cultures. Journal of Neuroscience 24:5216-5229.

Behrens TE, Woolrich MW, Jenkinson M, Johansen-Berg H, Nunes RG, Clare S, Matthews PM, Brady JM, Smith SM (2003a) Characterization and propagation of uncertainty in diffusion-weighted MR imaging. Magnetic resonance in medicine : official journal of the Society of Magnetic Resonance in Medicine / Society of Magnetic Resonance in Medicine 50:1077-1088.

Behrens TE, Johansen-Berg H, Woolrich MW, Smith SM, Wheeler-Kingshott CA, Boulby PA, Barker GJ, Sillery EL, Sheehan K, Ciccarelli O, Thompson AJ, Brady JM, Matthews PM (2003b) Non-invasive mapping of connections between human thalamus and cortex using diffusion imaging. Nat Neurosci 6:750-757.

Behrens TEJ, Woolrich MW, Jenkinson M, Johansen-Berg H, Nunes RG, Clare S, Matthews PM, Brady JM, Smith SM (2003c) Characterization and propagation of uncertainty in diffusion-weighted MR imaging. Magnetic Resonance in Medicine 50:1077-1088.

Bigler ED (2001) Neuropsychological testing defines the neurobehavioral significance of neuroimaging-identified abnormalities. Arch Clin Neuropsychol 16:227-236.

Bluhm RL, Miller J, Lanius RA, Osuch EA, Boksman K, Neufeld RW, Theberge J, Schaefer B, Williamson P (2007) Spontaneous low-frequency fluctuations in the BOLD signal in schizophrenic patients: anomalies in the default network. Schizophr Bull 33:1004-1012.

Boly M, Tshibanda L, Vanhaudenhuyse A, Noirhomme Q, Schnakers C, Ledoux D, Boveroux P, Garweg C, Lambermont B, Phillips C, Luxen A, Moonen G, Bassetti C, Maquet P, Laureys S (2009) Functional connectivity in the default

network during resting state is preserved in a vegetative but not in a brain dead patient. Hum Brain Mapp 30:2393-2400.

Bonnelle V, Ham TE, Leech R, Kinnunen KM, Mehta MA, Greenwood RJ, Sharp DJ (2012) Salience network integrity predicts default mode network function after traumatic brain injury. Proceedings of the National Academy of Sciences of the United States of America 109:4690-4695.

Bonnelle V, Leech R, Kinnunen KM, Ham TE, Beckmann CF, De Boissezon X, Greenwood RJ, Sharp DJ (2011) Default Mode Network Connectivity Predicts Sustained Attention Deficits after Traumatic Brain Injury. The Journal of neuroscience : the official journal of the Society for Neuroscience 31:13442-13451.

Breakspear M, Heitmann S, Daffertshofer A (2010) Generative models of cortical oscillations: neurobiological implications of the kuramoto model. Frontiers in human neuroscience 4:190}.

Brefel-Courbon C, Payoux P, Ory F, Sommet A, Slaoui T, Raboyeau G, Lemesle B, Puel M, Montastruc JL, Demonet JF, Cardebat D (2007) Clinical and imaging evidence of zolpidem effect in hypoxic encephalopathy. Annals of neurology 62:102-105.

Bressler SL, Kelso JA (2001) Cortical coordination dynamics and cognition. Trends in cognitive sciences 5:26-36.

Bruns J, Jr., Hauser WA (2003) The epidemiology of traumatic brain injury: a review. Epilepsia 44 Suppl 10:2-10.

Buckner RL, Andrews-Hanna JR, Schacter DL (2008) The brain's default network: anatomy, function, and relevance to disease. Annals of the New York Academy of Sciences 1124:1--38.

Bullmore E, Sporns O (2009) Complex brain networks: graph theoretical analysis of structural and functional systems. Nature Reviews Neuroscience 10:186-198.

Cabral J, Kringelbach ML, Deco G (2014) Exploring the network dynamics underlying brain activity during rest. Prog Neurobiol 114:102-131.

Cabral J, Hughes E, Sporns O, Deca G (2011a) Role of local network oscillations in resting-state functional connectivity. NeuroImage 57:130 - 139.

Cabral J, Hugues E, Kringelbach ML, Deco G (2012) Modeling the outcome of

structural disconnection on resting-state functional connectivity. NeuroImage 62:1342-1353.

Cabral J, Fernandes HM, Van Hartevelt TJ, James AC, Kringelbach ML, Deco G (2013) Structural connectivity in schizophrenia and its impact on the dynamics of spontaneous functional networks. Chaos 23:046111.

Caeyenberghs K, Leemans A, Leunissen I, Gooijers J, Michiels K, Sunaert S, Swinnen SP (2012a) Altered structural networks and executive deficits in traumatic brain injury patients. Brain structure & function.

Caeyenberghs K, Leemans A, Leunissen I, Gooijers J, Michiels K, Sunaert S, Swinnen SP (2014) Altered structural networks and executive deficits in traumatic brain injury patients. Brain structure & function 219:193-209.

Caeyenberghs K, Leemans A, De Decker C, Heitger M, Drijkoningen D, Linden CV, Sunaert S, Swinnen SP (2012b) Brain connectivity and postural control in young traumatic brain injury patients: A diffusion MRI based network analysis. NeuroImage: Clinical 1:106-115.

Caeyenberghs K, Leemans A, Heitger MH, Leunissen I, Dhollander T, Sunaert S, Dupont P, Swinnen SP (2012c) Graph analysis of functional brain networks for cognitive control of action in traumatic brain injury. Brain 135:1293-1307.

Cammoun L, Gigandet X, Meskaldji D, Thiran JP, Sporns O, Do KQ, Maeder P, Meuli R, Hagmann P (2011) Mapping the human connectome at multiple scales with diffusion spectrum MRI. Journal of neuroscience methods.

Carroll LJ, Cassidy JD, Holm L, Kraus J, Coronado VG (2004) Methodological issues and research recommendations for mild traumatic brain injury: the WHO Collaborating Centre Task Force on Mild Traumatic Brain Injury. J Rehabil Med:113-125.

Catani M, Ffytche DH (2005) The rises and falls of disconnection syndromes. Brain 128:2224-2239.

Chang C, Glover GH (2010a) Time--frequency dynamics of resting-state brain connectivity measured with fMRI. NeuroImage 50:81--98.

Chang C-C, Lin C-J (2011) LIBSVM: a library for support vector machines. TIST 2:27.

Chastain CA, Oyoyo UE, Zipperman M, Joo E, Ashwal S, Shutter LA, Tong KA (2009) Predicting outcomes of traumatic brain injury by imaging modality and injury

distribution. Journal of neurotrauma 26:1183-1196.

Chialvo D (2004) Critical brain networks. Physica A: Statistical Mechanics and its Applications 340:756-765.

Chialvo DR (2010) Emergent complex neural dynamics. Nature Physics.

Cocchi L, Zalesky A, Fontenelle LF (2012) How can connectomics advance our knowledge of psychiatric disorders? Revista brasileira de psiquiatria 34:131-132.

Comerford VE, Geffen GM, May C, Medland SE, Geffen LB (2002) A rapid screen of the severity of mild traumatic brain injury. J Clin Exp Neuropsychol 24:409-419.

Corbetta M, Shulman GL (2002) Control of goal-directed and stimulus-driven attention in the brain. Nature Reviews Neuroscience 3:215--229.

Cortes C (1995) Support-vector networks. Machine learning.

Cumin D, Unsworth CP (2007) Generalising the Kuramoto model for the study of neuronal synchronisation in the brain. Physica D: Nonlinear Phenomena 226:181--196.

Dale AM (1999) Cortical Surface-Based Analysis I. Segmentation and Surface Reconstruction. NeuroImage 9:179--194.

Deco G, Corbetta M (2011) The dynamical balance of the brain at rest. Neuroscientist 17:107-123.

Deco G, Rolls ET, Romo R (2009a) Stochastic dynamics as a principle of brain function. Progress in Neurobiology 88:1--16.

Deco G, Jirsa VK, McIntosh AR (2011) Emerging concepts for the dynamical organization of resting-state activity in the brain. Nature Reviews Neuroscience 12:43--56.

Deco G, Senden M, Jirsa V (2012) How anatomy shapes dynamics: a semi-analytical study of the brain at rest by a simple spin model. Frontiers in computational neuroscience 6:68.

Deco G, Jirsa VK, McIntosh AR (2013a) Resting brains never rest: computational insights into potential cognitive architectures. Trends Neurosci 36:268-274.

Deco G, Jirsa VK, Robinson PA, Breakspear M, Friston K (2008) The Dynamic Brain: From Spiking Neurons to Neural Masses and Cortical Fields. PLoS Comput Biol 4:e1000092.

Deco G, Jirsa V, McIntosh AR, Sporns O, Kötter R (2009b) Key role of coupling, delay, and noise in resting brain fluctuations. Proceedings of the National Academy of Sciences of the United States of America 106:10302-10307.

Deco G, Jirsa V, McIntosh AR, Sporns O, Kotter R (2009c) Key role of coupling, delay, and noise in resting brain fluctuations. PNAS 106:10302-10307.

Deco G, Ponce-Alvarez A, Mantini D, Romani GL, Hagmann P, Corbetta M (2013b) Resting-state functional connectivity emerges from structurally and dynamically shaped slow linear fluctuations. J Neurosci 33:11239-11252.

Deco G, Ponce-Alvarez A, Hagmann P, Romani GL, Mantini D, Corbetta M (2014) How local excitation-inhibition ratio impacts the whole brain dynamics. J Neurosci 34:7886-7898.

Desikan RS, Sègonne F, Fischl B, Quinn BT, Dickerson BC, Blacker D, Buckner RL, Dale AM, Maguire RP, Hyman BT, Albert MS, Killiany RJ (2006a) An automated labeling system for subdividing the human cerebral cortex on MRI scans into gyral based regions of interest. NeuroImage 31:968--980.

Desikan RS, Segonne F, Fischl B, Quinn BT, Dickerson BC, Blacker D, Buckner RL, Dale AM, Maguire RP, Hyman BT, Albert MS, Killiany RJ (2006b) An automated labeling system for subdividing the human cerebral cortex on MRI scans into gyral based regions of interest. Neuroimage 31:968-980.

Dockree PM, Kelly SP, Roche RA, Hogan MJ, Reilly RB, Robertson IH (2004) Behavioural and physiological impairments of sustained attention after traumatic brain injury. Brain Res Cogn Brain Res 20:403-414.

Draper K, Ponsford J (2008) Cognitive functioning ten years following traumatic brain injury and rehabilitation. Neuropsychology 22:618-625.

Ecker C, Rocha-Rego V, Johnston P, Mourao-Miranda J, Marquand A, Daly EM, Brammer MJ, Murphy C, Murphy DG (2010a) Investigating the predictive value of whole-brain structural MR scans in autism: A pattern classification approach. NeuroImage 49:44-56.

Ecker C, Marquand A, Mourao-Miranda J, Johnston P, Daly EM, Brammer MJ, Maltezos S, Murphy CM, Robertson D, Williams SC, Murphy DGM (2010b)

Describing the brain in autism in five dimensions--magnetic resonance imaging-assisted diagnosis of autism spectrum disorder using a multiparameter classification approach. Journal of Neuroscience 30:10612-10623.

Edison P, Archer HA, Gerhard A, Hinz R, Pavese N, Turkheimer FE, Hammers A, Tai YF, Fox N, Kennedy A, Rossor M, Brooks DJ (2008) Microglia, amyloid, and cognition in Alzheimer's disease: An [11C](R)PK11195-PET and [11C]PIB-PET study. Neurobiol Dis 32:412-419.

Efron B (1993) An introduction to the bootstrap. New York: Chapman & Hall.

Ennis DB, Kindlmann G (2005) Orthogonal tensor invariants and the analysis of diffusion tensor magnetic resonance images. Magnetic Resonance in Medicine 55:136-146.

Erika-Florence M, Leech R, Hampshire A (2014) A functional network perspective on response inhibition and attentional control. Nature communications 5:4073.

Fagerholm E, Lorenz R, Scott G, Dinov M, Hellyer PJ, Mizaei N, Leeson L, Carmichael DW, Sharp DK, Shew WL, Leech R (2015) Cascades and Cognitive State: Focused Attention Incurs Subcritical Dynamics. Journal of Neuroscience 35(11): 4626-4634

Fischl B, Dale AM (2000) Measuring the thickness of the human cerebral cortex from magnetic resonance images. Proceedings of the National Academy of Sciences of the United States of America 97:11050-11055.

Fischl B, Tootell RBH, Dale AM (1999) High-resolution intersubject averaging and a coordinate system for the cortical surface. Human Brain Mapping 8:272-284.

Fischl B, Salat DH, van der Kouwe AJW, Makris N, Ségonne F, Quinn BT, Dale AM (2004a) Sequence-independent segmentation of magnetic resonance images. NeuroImage 23:S69-S84.

Fischl B, Salat DH, Busa E, Albert MS, Dieterich M, Haselgrove C, van der Kouwe A, Killiany R, Kennedy D, Klaveness S, Montillo A, Makris N, Rosen B, Dale AM (2002) Whole brain segmentation: automated labeling of neuroanatomical structures in the human brain. Neuron 33:341-355.

Fischl B, van der Kouwe A, Destrieux C, Halgren E, Segonne F, Salat DH, Busa E, Seidman LJ, Goldstein J, Kennedy D, Caviness V, Makris N, Rosen B, Dale AM (2004b) Automatically parcellating the human cerebral cortex. Cerebral cortex 14:11-22.

Fischl B, van der Kouwe A, Destrieux C, Halgren E, Ségonne F, Salat DH, Busa E, Seidman LJ, Goldstein J, Kennedy D, Caviness V, Makris N, Rosen B, Dale AM (2004c) Automatically Parcellating the Human Cerebral Cortex. Cerebral cortex 14:11-22.

Fornito A, Zalesky A, Pantelis C, Bullmore ET (2012a) Schizophrenia, neuroimaging and connectomics. Neuroimage 62:2296-2314.

Fornito A, Harrison BJ, Zalesky A, Simons JS (2012b) Competitive and cooperative dynamics of large-scale brain functional networks supporting recollection. Proceedings of the National Academy of Sciences 109:12788--12793.

Fox MD, Raichle ME (2007) Spontaneous fluctuations in brain activity observed with functional magnetic resonance imaging. Nat Rev Neurosci 8:700-711.

Fox MD, Zhang D, Snyder AZ, Raichle ME (2009) The global signal and observed anticorrelated resting state brain networks. Journal of neurophysiology 101:3270--3283.

Fox MD, Snyder AZ, Vincent JL, Corbetta M, Van Essen DC, Raichle ME (2005) The human brain is intrinsically organized into dynamic, anticorrelated functional networks. Proceedings of the National Academy of Sciences of the United States of America 102:9673--9678.

Friston K (1997a) Analysing brain images: principles and overview. In: Human brain function (Frackowiak R, Friston K, Frith CD, Dolan RJ, Mazziotta JC, eds). San Diego: Academic Press.

Friston KJ (1997b) Transients, metastability, and neuronal dynamics. NeuroImage 5:164-171.

Friston KJ (2002) Dysfunctional connectivity in schizophrenia. World psychiatry : official journal of the World Psychiatric Association (WPA) 1:66-71.

Friston KJ, Frith CD, Liddle PF, Frackowiak RS (1993) Functional connectivity: the principal-component analysis of large (PET) data sets. J Cereb Blood Flow Metab 13:5-14.

Friston KJ, Mechelli A, Turner R, Price CJ (2000) Nonlinear responses in fMRI: the Balloon model, Volterra kernels, and other hemodynamics. Neuroimage 12:466-477.

Fritz JB, David SV, Radtke-Schuller S, Yin P, Shamma SA (2010) Adaptive,

behaviorally gated, persistent encoding of task-relevant auditory information in ferret frontal cortex. Nature neuroscience 13:1011--1019.

Geddes JF, Vowles GH, Beer TW, Ellison DW (1997) The diagnosis of diffuse axonal injury: implications for forensic practice. Neuropathol Appl Neurobiol 23:339-347.

Gentleman SM, Roberts GW, Gennarelli TA, Maxwell WL, Adams JH, Kerr S, Graham DI (1995) Axonal injury: a universal consequence of fatal closed head injury? Acta Neuropathol 89:537-543.

Gigandet X, Hagmann P, Kurant M, Cammoun L, Meuli R, Thiran JP (2008) Estimating the confidence level of white matter connections obtained with MRI tractography. PloS one 3:e4006.

Godefroy O (2003) Frontal syndrome and disorders of executive functions. Journal of neurology 250:1-6.

Gong G, He Y, Concha L, Lebel C, Gross DW, Evans AC, Beaulieu C (2009) Mapping anatomical connectivity patterns of human cerebral cortex using in vivo diffusion tensor imaging tractography. Cerebral cortex 19:524-536.

Good P (2005) Permutation, Parametric and Bootstrap Tests of Hypothesies, 3rd Edition. New York: Springer.

Grabner G, Janke AL, Budge MM, Smith D, Pruessner J, Collins DL (2006) Symmetric atlasing and model based segmentation: an application to the hippocampus in older adults. Med Image Comput Comput Assist Interv 9:58-66.

Graham DI, Raghupathi R, Saatman KE, Meaney D, McIntosh TK (2000) Tissue tears in the white matter after lateral fluid percussion brain injury in the rat: relevance to human brain injury. Acta Neuropathol 99:117-124.

Greicius MD, Srivastava G, Reiss AL, Menon V (2004) Default-mode network activity distinguishes Alzheimer's disease from healthy aging: evidence from functional MRI. Proc Natl Acad Sci U S A 101:4637-4642.

Greicius MD, Supekar K, Menon V, Dougherty RF (2009) Resting-state functional connectivity reflects structural connectivity in the default mode network. Cerebral cortex 19:72-78.

Greve DN, Fischl B (2009) Accurate and robust brain image alignment using

boundary-based registration. NeuroImage 48:63--72.

Hagmann P, Cammoun L, Gigandet X, Meuli R, Honey CJ, Wedeen VJ, Sporns O (2008) Mapping the structural core of human cerebral cortex. PLoS biology 6:e159.

Haimovici A, Tagliazucchi E, Balenzuela P, Chialvo DR (2013) Brain organization into resting state networks emerges at criticality on a model of the human connectome. Physical review letters 110:178101.

Haimovici AT, E; Balenzuela, P; Chialvo, Dante R. (2013) Brain Organizarion into resting state networks emerges at criticality on a model of the human connectome. Physical Review Letters in press.

Ham T, Bonnelle V, Hellyer P, Jilka S, Robertson I, Leech R, Sharp D (2013) The neural basis of impaired self-awareness after traumatic brain injury. Brain : a journal of neurology.

Handwerker DA, Roopchansingh V, Gonzalez-Castillo J, Bandettini PA (2012) Periodic changes in fMRI connectivity. Neuroimage 63:1712-1719.

Haselgrove JC, Moore JR (1996) Correction for distortion of echo-planar images used to calculate the apparent diffusion coefficient. Magnetic resonance in medicine : official journal of the Society of Magnetic Resonance in Medicine / Society of Magnetic Resonance in Medicine 36:960-964.

Hellyer PJ, Leech R, Ham TE, Bonnelle V, Sharp DJ (2013) Individual prediction of white matter injury following traumatic brain injury. Annals of neurology 73:489-499.

Hellyer PJ, Shanahan M, Scott G, Wise RJS, Sharp DJ, Leech R (2014) The control of global brain dynamics: opposing actions of frontoparietal control and default mode networks on attention. Journal of Neuroscience 34:451-461.

Hillary FG, Slocomb J, Hills EC, Fitzpatrick NM, Medaglia JD, Wang J, Good DC, Wylie GR (2011) Changes in resting connectivity during recovery from severe traumatic brain injury. Int J Psychophysiol 82:115-123.

Honey CJ, Thivierge JP, Sporns O (2010) Can structure predict function in the human brain? Neuroimage 52:766-776.

Honey CJ, Sporns O, Cammoun L, Gigandet X, Thiran JP, Meuli R, Hagmann P (2009) Predicting human resting-state functional connectivity from structural

connectivity. Proc Natl Acad Sci U S A 106:2035-2040.

Humphries MD, Gurney K (2008) Network 'Small-World-Ness': A Quantitative Method for Determining Canonical Network Equivalence. PloS one 3.

Hutchison RM, Womelsdorf T, Gati JS, Everling S, Menon RS (2013a) Resting-state networks show dynamic functional connectivity in awake humans and anesthetized macaques. Hum Brain Mapp 34:2154-2177.

Hutchison RM, Womelsdorf T, Allen EA, Bandettini PA, Calhoun VD, Corbetta M, Della Penna S, Duyn JH, Glover GH, Gonzalez-Castillo J, Handwerker DA, Keilholz S, Kiviniemi V, Leopold DA, de Pasquale F, Sporns O, Walter M, Chang C (2013b) Dynamic functional connectivity: promise, issues, and interpretations. Neuroimage 80:360-378.

Jenkinson M, Bannister P, Brady M, Smith S (2002) Improved optimization for the robust and accurate linear registration and motion correction of brain images. NeuroImage 17:825--841.

Jezzard P, Balaban RS (1995) Correction for geometric distortion in echo planar images from B0 field variations. Magnetic resonance in medicine : official journal of the Society of Magnetic Resonance in Medicine / Society of Magnetic Resonance in Medicine 34:65-73.

Jezzard P, Barnett AS, Pierpaoli C (1998) Characterization of and correction for eddy current artifacts in echo planar diffusion imaging. Magnetic resonance in medicine : official journal of the Society of Magnetic Resonance in Medicine / Society of Magnetic Resonance in Medicine 39:801-812.

Jilka S, Scott G, Ham TE, Pickering A, Bonnelle V, Braga R, Leech R, Sharp DJ (2014) Damage to the Salience Network and Interactions with the Default Mode Network. The Journal of Neuroscience 34:10798-10807.

Johnson VE, Stewart JE, Begbie FD, Trojanowski JQ, Smith DH, Stewart W (2013) Inflammation and white matter degeneration persist for years after a single traumatic brain injury. Brain : a journal of neurology 136:28-42.

Jones DK (2010a) Precision and Accuracy in Diffusion Tensor Magnetic Resonance Imaging. Topics in Magnetic Resonance Imaging 21:87-99.

Jones DK (2010b) Challenges and limitations of quantifying brain connectivity in vivo with diffusion MRI. Imaging in Medicine 2:341-355.

Kelly AMC, Uddin LQ, Biswal BB, Castellanos FX, Milham MP (2008) Competition between functional brain networks mediates behavioral variability. NeuroImage 39:527--537.

Kelso JAS (2012) Multistability and metastability: understanding dynamic coordination in the brain. Phil Trans R Soc B 2012:906-918.

Kennedy DP, Courchesne E (2008) The intrinsic functional organization of the brain is altered in autism. Neuroimage 39:1877-1885.

Kennedy MRT, Wozniak JR, Muetzel RL, Mueller BA, Chiou H-H, Pantekoek K, Lim KO (2009) White matter and neurocognitive changes in adults with chronic traumatic brain injury. Journal of the International Neuropsychological Society : JINS 15:130-136.

Kinnunen KM, Greenwood R, Powell JH, Leech R, Hawkins PC, Bonnelle V, Patel MC, Counsell SJ, Sharp DJ (2011) White matter damage and cognitive impairment after traumatic brain injury. Brain 134:449-463.

Kitzbichler MG, Smith ML, Christensen SoR, Bullmore E (2009) Broadband criticality of human brain network synchronization. PLoS Computational Biology 5:e1000314.

Klawiter EC, Schmidt RE, Trinkaus K, Liang H-F, Budde MD, Naismith RT, Song S-K, Cross AH, Benzinger TL (2011) Radial diffusivity predicts demyelination in ex vivo multiple sclerosis spinal cords. NeuroImage 55:1454-1460.

Kraus MF, Susmaras T, Caughlin BP, Walker CJ, Sweeney JA, Little DM (2007) White matter integrity and cognition in chronic traumatic brain injury: a diffusion tensor imaging study. Brain 130:2508-2519.

Kuramoto Y (1984) Chemical oscillations, waves, and turbulence. New York: Springer.

Lee H, Wintermark M, Gean AD, Ghajar J, Manley GT, Mukherjee P (2008) Focal lesions in acute mild traumatic brain injury and neurocognitive outcome: CT versus 3T MRI. Journal of neurotrauma 25:1049-1056.

Leech R, Sharp DJ (2014) The role of the posterior cingulate cortex in cognition and disease. Brain 137:12-32.

Levin HS (1995) Prediction of recovery from traumatic brain injury. Journal of neurotrauma 12:913-922.

Levin HS, Kraus MF (1994) The frontal lobes and traumatic brain injury. J Neuropsychiatry Clin Neurosci 6:443-454.

Levine B, Black SE, Cheung G, Campbell A, O'Toole C, Schwartz ML (2005) Gambling task performance in traumatic brain injury: relationships to injury severity, atrophy, lesion location, and cognitive and psychosocial outcome. Cognitive and behavioral neurology : official journal of the Society for Behavioral and Cognitive Neurology 18:45-54.

Li J, Li X-Y, Feng D-F, Gu L (2011) Quantitative evaluation of microscopic injury with diffusion tensor imaging in a rat model of diffuse axonal injury. Eur J Neurosci 33:933-945.

Liang M, Zhou Y, Jiang T, Liu Z, Tian L, Liu H, Hao Y (2006) Widespread functional disconnectivity in schizophrenia with resting-state functional magnetic resonance imaging. Neuroreport 17:209-213.

MacDonald CL, Dikranian K, Bayly P, Holtzman D, Brody D (2007a) Diffusion tensor imaging reliably detects experimental traumatic axonal injury and indicates approximate time of injury. J Neurosci 27:11869-11876.

MacDonald CL, Dikranian K, Song SK, Bayly PV, Holtzman DM, Brody DL (2007b) Detection of traumatic axonal injury with diffusion tensor imaging in a mouse model of traumatic brain injury. Experimental neurology 205:116-131.

Malec JF, Brown AW, Leibson CL, Flaada JT, Mandrekar JN, Diehl NN, Perkins PK (2007) The mayo classification system for traumatic brain injury severity. J Neurotrauma 24:1417-1424.

Mathias JL, Beall JA, Bigler ED (2004a) Neuropsychological and information processing deficits following mild traumatic brain injury. J Int Neuropsychol Soc 10:286-297.

Mathias JL, Bigler ED, Jones NR, Bowden SC, Barrett-Woodbridge M, Brown GC, Taylor DJ (2004b) Neuropsychological and information processing performance and its relationship to white matter changes following moderate and severe traumatic brain injury: a preliminary study. Applied neuropsychology 11:134-152.

Mayer AR, Mannell MV, Ling J, Gasparovic C, Yeo RA (2011) Functional connectivity in mild traumatic brain injury. Human brain mapping 32:1825-1835.

McKeown MJ, Sejnowski TJ (1998) Independent component analysis of fMRI data:

examining the assumptions. Hum Brain Mapp 6:368-372.

McKeown MJ, Jung TP, Makeig S, Brown G, Kindermann SS, Lee TW, Sejnowski TJ (1998a) Spatially independent activity patterns in functional MRI data during the stroop color-naming task. Proc Natl Acad Sci U S A 95:803-810.

McKeown MJ, Makeig S, Brown GG, Jung TP, Kindermann SS, Bell AJ, Sejnowski TJ (1998b) Analysis of fMRI data by blind separation into independent spatial components. Hum Brain Mapp 6:160-188.

Medana IM, Esiri MM (2003) Axonal damage: a key predictor of outcome in human CNS diseases. Brain : a journal of neurology 126:515-530.

Menon DK, Schwab K, Wright DW, Maas AI, Demographics, Clinical Assessment Working Group of the I, Interagency Initiative toward Common Data Elements for Research on Traumatic Brain I, Psychological H (2010) Position statement: definition of traumatic brain injury. Arch Phys Med Rehabil 91:1637-1640.

Messe A, Benali H, Marrelec G (2014a) Relating structural and functional connectivity in MRI: A simple model for a complex brain. IEEE transactions on medical imaging.

Messe A, Rudrauf D, Benali H, Marrelec G (2014b) Relating structure and function in the human brain: relative contributions of anatomy, stationary dynamics, and non-stationarities. PLoS Comput Biol 10:e1003530.

Messe A, Caplain S, Paradot G, Garrigue D, Mineo JF, Soto Ares G, Ducreux D, Vignaud F, Rozec G, Desal H, Pelegrini-Issac M, Montreuil M, Benali H, Lehericy S (2011) Diffusion tensor imaging and white matter lesions at the subacute stage in mild traumatic brain injury with persistent neurobehavioral impairment. Human brain mapping 32:999-1011.

Mesulam MM (1998) From sensation to cognition. Brain 121 (Pt 6):1013-1052.

Mohammadi S, Nagy Z, Moller HE, Symms MR, Carmichael DW, Josephs O, Weiskopf N (2012) The effect of local perturbation fields on human DTI: characterisation, measurement and correction. Neuroimage 60:562-570.

Montague PR, Dolan RJ, Friston KJ, Dayan P (2011) Computational psychiatry. Trends in cognitive sciences.

Monti RP, Hellyer P, Sharp D, Leech R, Anagnostopoulos C, Montana G (2014) Estimating time-varying brain connectivity networks from functional MRI time

series. Neuroimage.

Mori S, Zhang J (2006) Principles of diffusion tensor imaging and its applications to basic neuroscience research. Neuron 51:527-539.

Mori S, van Zijl P (2007) Human white matter atlas. The American journal of psychiatry 164:1005.

Mourao-Miranda J, Bokde ALW, Born C, Hampel H, Stetter M (2005) Classifying brain states and determining the discriminating activation patterns: Support Vector Machine on functional MRI data. NeuroImage 28:980-995.

Niazy RK, Xie J, Miller K, Beckmann CF, Smith SM (2011) Spectral characteristics of resting state networks. Prog Brain Res 193:259-276.

Nichols TE, Holmes AP (2002) Nonparametric permutation tests for functional neuroimaging: a primer with examples. Hum Brain Mapp 15:1-25.

Niemann H, Ruff RM, Kramer JH (1996) An attempt towards differentiating attentional deficits in traumatic brain injury. Neuropsychology review 6:11-46.

Niogi SN, Mukherjee P, Ghajar J, Johnson CE, Kolster R, Lee H, Suh M, Zimmerman RD, Manley GT, McCandliss BD (2008a) Structural dissociation of attentional control and memory in adults with and without mild traumatic brain injury. Brain : a journal of neurology 131:3209-3221.

Niogi SN, Mukherjee P, Ghajar J, Johnson C, Kolster RA, Sarkar R, Lee H, Meeker M, Zimmerman RD, Manley GT, McCandliss BD (2008b) Extent of microstructural white matter injury in postconcussive syndrome correlates with impaired cognitive reaction time: a 3T diffusion tensor imaging study of mild traumatic brain injury. AJNR American journal of neuroradiology 29:967-973.

O'Keeffe F M, Dockree PM, Moloney P, Carton S, Robertson IH (2007) Characterising error-awareness of attentional lapses and inhibitory control failures in patients with traumatic brain injury. Exp Brain Res.

Palomero-Gallagher N, Vogt BA, Schleicher A, Mayberg HS, Zilles K (2009) Receptor architecture of human cingulate cortex: Evaluation of the four-region neurobiological model. Human Brain Mapping 30:2336--2355.

Pandit AS, Expert P, Lambiotte R, Bonnelle V, Leech R, Turkheimer FE, Sharp DJ (2013) Traumatic brain injury impairs small-world topology. Neurology 80:1826-1833.

Park NW, Moscovitch M, Robertson IH (1999) Divided attention impairments after traumatic brain injury. Neuropsychologia 37:1119-1133.

Platt J (1999) Probabilistic outputs for support vector machines and comparisons to regularized likelihood methods. Advances in large margin classifiers.

Ponsford J, Kinsella G (1992) Attentional deficits following closed-head injury. Journal of clinical and experimental neuropsychology 14:822-838.

Power JD, Schlaggar BL, Petersen SE (2015) Recent progress and outstanding issues in motion correction in resting state fMRI. Neuroimage 105:536-551.

Power JD, Mitra A, Laumann TO, Snyder AZ, Schlaggar BL, Petersen SE (2014) Methods to detect, characterize, and remove motion artifact in resting state fMRI. Neuroimage 84:320-341.

Raichle ME, MacLeod AM, Powers WJ, Gusnard DA, Shulman GL (2001) A default mode of brain function. Proceedings of the National Academy of Sciences of the United States of America 98:676-682.

Ramlackhansingh AF, Brooks DJ, Greenwood RJ, Bose SK, Turkheimer FE, Kinnunen KM, Gentleman S, Heckemann RA, Gunanayagam K, Gelosa G, Sharp DJ (2011) Inflammation after trauma: Microglial activation and traumatic brain injury. Annals of neurology 70:374-383.

Reitan RM (1958) Validity of the Trail Making Test as an indicator of organic brain damage. Percept Mot Skills 8:271-276.

Rubinov M, Sporns O (2010) Complex network measures of brain connectivity: uses and interpretations. Neuroimage 52:1059-1069.

Rueckert D, Sonoda LI, Hayes C, Hill DL, Leach MO, Hawkes DJ (1999) Nonrigid registration using free-form deformations: application to breast MR images. IEEE transactions on medical imaging 18:712-721.

Rugg-Gunn FJ, Symms MR, Barker GJ, Greenwood RJ, Duncan JS (2001) Diffusion imaging shows abnormalities after blunt head trauma when conventional magnetic resonance imaging is normal. Journal of Neurology Neurosurgery and Psychiatry 70:530-533.

Sajda P (2006) Machine Learning for detection and diagnosis of disease. Annual Review of Biomedical Engineering 8:537-565.

Savoy RL (2001) History and future directions of human brain mapping and functional neuroimaging. Acta Psychol (Amst) 107:9-42.

Scheid R, Preul C, Gruber O, Wiggins C, von Cramon DY (2003) Diffuse axonal injury associated with chronic traumatic brain injury: evidence from T2*-weighted gradient-echo imaging at 3 T. AJNR American journal of neuroradiology 24:1049-1056.

Scheid R, Walther K, Guthke T, Preul C, von Cramon DY (2006) Cognitive sequelae of diffuse axonal injury. Arch Neurol 63:418-424.

Seeley WW, Menon V, Schatzberg AF, Keller J, Glover GH, Kenna H, Reiss AL, Greicius MD (2007) Dissociable intrinsic connectivity networks for salience processing and executive control. J Neurosci 27:2349-2356.

Senden M, Goebel R, Deco G (2012) Structural connectivity allows for multi-threading during rest: the structure of the cortex leads to efficient alternation between resting state exploratory behavior and default mode processing. Neuroimage 60:2274-2284.

Senden M, Deco G, de Reus MA, Goebel R, van den Heuvel MP (2014) Rich club organization supports a diverse set of functional network configurations. Neuroimage 96:174-182.

Shanahan M (2010a) Embodiment and the Inner Life.

Shanahan M (2010b) Metastable chimera states in community-structured oscillator networks. Chaos: An Interdisciplinary Journal of Nonlinear Science 20:013108}.

Shanahan M (2010c) Embodiment and the Inner Life: Cognition and Conciousness in the Space of Possible Minds: Oxford University Press.

Shanahan M (2012) The brain's connective core and its role in animal cognition. Philosophical Transactions of the Royal Society B: Biological Sciences 367:2704--2714.

Sharp DJ, Ham TE (2011) Investigating white matter injury after mild traumatic brain injury. Curr Opin Neurol 24:558-563.

Sharp DJ, Scott G, Leech R (2014) Network dysfunction after traumatic brain injury. Nat Rev Neurol 10:156-166.

Sharp DJ, Turkheimer FE, Bose SK, Scott SK, Wise RJ (2010a) Increased

frontoparietal integration after stroke and cognitive recovery. Annals of neurology 68:753-756.

Sharp DJ, Bonnelle V, De Boissezon X, Beckmann CF, James SG, Patel MC, Mehta MA (2010b) Distinct frontal systems for response inhibition, attentional capture, and error processing. Proceedings of the National Academy of Sciences of the United States of America 107:6106-6111.

Sharp DJ, Beckman CF, Kinnunen KM, Bonnelle V, Turkheimer FE, De Boissezon X, Dyson E, Leech R (2009) Altered functional connectivity after traumatic brain injury identified in resting state functional MRI. In: Neuroscience. Chicago.

Sharp DJ, Beckmann CF, Greenwood RJ, Kinnunen KM, Bonnelle V, De Boissezon X, Powell JH, Counsell SJ, Patel MC, Leech R (2011a) Default mode network functional and structural connectivity after traumatic brain injury. Brain : a journal of neurology 134:2233--2247.

Sharp DJ, Beckmann CF, Greenwood R, Kinnunen KM, Bonnelle V, De Boissezon X, Powell JH, Counsell SJ, Patel MC, Leech R (2011b) Default mode network functional and structural connectivity after traumatic brain injury. Brain 134:2233-2247.

Sheline YI, Raichle ME (2013) Resting state functional connectivity in preclinical Alzheimer's disease. Biol Psychiatry 74:340-347.

Shumskaya E, Andriessen TM, Norris DG, Vos PE (2012) Abnormal whole-brain functional networks in homogeneous acute mild traumatic brain injury. Neurology 79:175-182.

Sidaros A, Engberg AW, Sidaros K, Liptrot MG, Herning M, Petersen P, Paulson OB, Jernigan TL, Rostrup E (2008) Diffusion tensor imaging during recovery from severe traumatic brain injury and relation to clinical outcome: a longitudinal study. Brain 131:559-572.

Singh KD, Fawcett IP (2008) Transient and linearly graded deactivation of the human default-mode network by a visual detection task. NeuroImage 41:100--112.

Smith SM (2002) Fast robust automated brain extraction. Hum Brain Mapp 17:143-155.

Smith SM, Jenkinson M, Johansen-Berg H, Rueckert D, Nichols TE, Mackay CE, Watkins KE, Ciccarelli O, Cader MZ, Matthews PM, Behrens TE (2006) Tract-based spatial statistics: voxelwise analysis of multi-subject diffusion data.

Neuroimage 31:1487-1505.

Smith SM, Fox PT, Miller KL, Glahn DC, Fox PT, Mackay CE, Filippini N, Watkins KE, Toro R, Laird AR, Beckmann CF (2009a) Correspondence of the brain's functional architecture during activation and rest. Proceedings of the National Academy of Sciences of the United States of America 106:13040--13045.

Smith SM, Fox PT, Miller KL, Glahn DC, Fox PM, Mackay CE, Filippini N, Watkins KE, Toro R, Laird AR, Beckmann CF (2009b) Correspondence of the brain's functional architecture during activation and rest. Proc Natl Acad Sci U S A 106:13040-13045.

Smith SM, Miller KL, Moeller S, Xu J, Auerbach EJ, Woolrich MW, Beckmann CF, Jenkinson M, Andersson J, Glasser MF, Van Essen DC, Feinberg DA, Yacoub ES, Ugurbil K (2012) Temporally-independent functional modes of spontaneous brain activity. Proceedings of the National Academy of Sciences 109:3131-3136.

Smith SM, Jenkinson M, Woolrich MW, Beckmann CF, Behrens TE, Johansen-Berg H, Bannister PR, De Luca M, Drobnjak I, Flitney DE, Niazy RK, Saunders J, Vickers J, Zhang Y, De Stefano N, Brady JM, Matthews PM (2004a) Advances in functional and structural MR image analysis and implementation as FSL. Neuroimage 23 Suppl 1:S208-219.

Smith SM, Jenkinson M, Woolrich MW, Beckmann CF, Behrens TEJ, Johansen-Berg H, Bannister PR, De Luca M, Drobnjak I, Flitney DE, Niazy RK, Saunders J, Vickers J, Zhang Y, De Stefano N, Brady JM, Matthews PM (2004b) Advances in functional and structural MR image analysis and implementation as FSL. NeuroImage 23 Suppl 1:S208--219}.

Smits M, Houston GC, Dippel DW, Wielopolski PA, Vernooij MW, Koudstaal PJ, Hunink MG, van der Lugt A (2011) Microstructural brain injury in post-concussion syndrome after minor head injury. Neuroradiology 53:553-563.

Song S-K, Sun S-W, Ramsbottom MJ, Chang C, Russell J, Cross AH (2002) Dysmyelination revealed through MRI as increased radial (but unchanged axial) diffusion of water. NeuroImage 17:1429-1436.

Song S-K, Sun S-W, Ju W-K, Lin S-J, Cross AH, Neufeld AH (2003) Diffusion tensor imaging detects and differentiates axon and myelin degeneration in mouse optic nerve after retinal ischemia. NeuroImage 20:1714-1722.

Sponheim SR, McGuire KA, Kang SS, Davenport ND, Aviyente S, Bernat EM, Lim KO (2011) Evidence of disrupted functional connectivity in the brain after combat-related blast injury. NeuroImage 54, Supplement 1:S21-S29.

Sporns O (2003) Graph theory methods for the analysis of neural connectivity patterns. In: Neuroscience Databases, pp 171-185: Springer.

Sporns O (2006) Small-world connectivity, motif composition, and complexity of fractal neuronal connections. Biosystems 85:55-64.

Sporns O (2011) The human connectome: a complex network. Ann N Y Acad Sci 1224:109-125.

Sporns O (2013) Structure and function of complex brain networks. Dialogues Clin Neurosci 15:247-262.

Sporns O, Kotter R (2004) Motifs in brain networks. PLoS Biol 2:e369.

Sporns O, Zwi JD (2004) The small world of the cerebral cortex. Neuroinformatics 2:145-162.

Sporns O, Tononi G, Kotter R (2005) The human connectome: A structural description of the human brain. PLoS Comput Biol 1:e42.

Spreng RN, Grady CL (2010) Patterns of brain activity supporting autobiographical memory, prospection, and theory of mind, and their relationship to the default mode network. J Cogn Neurosci 22:1112-1123.

Spreng RN, Stevens WD, Chamberlain JP, Gilmore AW, Schacter DL (2010) Default network activity, coupled with the frontoparietal control network, supports goal-directed cognition. NeuroImage 53:303--317.

Squarcina L, Bertoldo A, Ham TE, Heckemann R, Sharp DJ (2012) A robust method for investigating thalamic white matter tracts after traumatic brain injury. Neuroimage 63:779-788.

Stephan KE, Mathys C (2014) Computational approaches to psychiatry. Current opinion in neurobiology 25:85-92.

Strogatz SH (2001) Exploring complex networks. Nature 410:268-276.

Sun L, Cao Q, Long X, Sui M, Cao X, Zhu C, Zuo X, An L, Song Y, Zang Y, Wang Y (2012) Abnormal functional connectivity between the anterior cingulate

and the default mode network in drug-naive boys with attention deficit hyperactivity disorder. Psychiatry Res 201:120-127.

Tognoli E, Kelso JAS (2014) The Metastable Brain. Neuron 81:35-48.

Tsuda I (2001) Toward an interpretation of dynamic neural activity in terms of chaotic dynamical systems. Behavioural and Brain Sciences 24:793-847.

Uhlhaas PJ, Singer W (2006) Neural synchrony in brain disorders: relevance for cognitive dysfunctions and pathophysiology. Neuron 52:155-168.

Vaishnavi S, Rao V, Fann JR (2009) Neuropsychiatric problems after traumatic brain injury: unraveling the silent epidemic. Psychosomatics 50:198-205.

Van Den Heuvel C, Thornton E, Vink R (2007) Traumatic brain injury and Alzheimer's disease: a review. Prog Brain Res 161:303-316.

van den Heuvel MP, Sporns O (2011) Rich-club organization of the human connectome. The Journal of neuroscience : the official journal of the Society for Neuroscience 31:15775-15786.

van den Heuvel MP, Sporns O (2013a) Network hubs in the human brain. Trends in cognitive sciences 17:683-696.

van den Heuvel MP, Sporns O (2013b) An anatomical substrate for integration among functional networks in human cortex. J Neurosci 33:14489-14500.

van den Heuvel MP, Fornito A (2014) Brain networks in schizophrenia. Neuropsychology review 24:32-48.

van den Heuvel MP, Kahn RS, Goni J, Sporns O (2012) High-cost, high-capacity backbone for global brain communication. Proc Natl Acad Sci U S A 109:11372-11377.

van den Heuvel MP, Mandl RC, Stam CJ, Kahn RS, Hulshoff Pol HE (2010) Aberrant frontal and temporal complex network structure in schizophrenia: a graph theoretical analysis. J Neurosci 30:15915-15926.

van den Heuvel MP, Sporns O, Collin G, Scheewe T, Mandl RC, Cahn W, Goni J, Hulshoff Pol HE, Kahn RS (2013) Abnormal rich club organization and functional brain dynamics in schizophrenia. JAMA psychiatry 70:783-792.

Vapnik VN (2000) The nature of statistical learning theory: Springer-Verlag New York

Inc.

Vincent JL, Kahn I, Snyder AZ, Raichle ME, Buckner RL (2008) Evidence for a frontoparietal control system revealed by intrinsic functional connectivity. Journal of neurophysiology 100:3328--3342.

Watts DJ, Strogatz SH (1998) Collective dynamics of 'small-world' networks. Nature 393:440-442.

Waxman SG (1980) Determinants of conduction velocity in myelinated nerve fibers. Muscle & Nerve 3:141-150.

Weng SJ, Wiggins JL, Peltier SJ, Carrasco M, Risi S, Lord C, Monk CS (2010) Alterations of resting state functional connectivity in the default network in adolescents with autism spectrum disorders. Brain Res 1313:202-214.

Werner G (2007) Metastability, criticality and phase transitions in brain and its models. Bio Systems 90:496--508.

Whitfield-Gabrieli S, Thermenos HW, Milanovic S, Tsuang MT, Faraone SV, McCarley RW, Shenton ME, Green AI, Nieto-Castanon A, LaViolette P, Wojcik J, Gabrieli JD, Seidman LJ (2009) Hyperactivity and hyperconnectivity of the default network in schizophrenia and in first-degree relatives of persons with schizophrenia. Proc Natl Acad Sci U S A 106:1279-1284.

Whitnall L, McMillan T, Murray G, Teasdale G (2006) Disability in young people and adults after head injury: 5-7 year follow up of a prospective cohort study. Journal of Neurology Neurosurgery and Psychiatry 77:640-645.

Wildie M, Shanahan M (2012) Metastability and chimera states in modular delay and pulse-coupled oscillator networks. Chaos: An Interdisciplinary Journal of Nonlinear Science 22:043131.

Winkler AM, Ridgway GR, Webster MA, Smith SM, Nichols TE (2014) Permutation inference for the general linear model. Neuroimage 92:381-397.

Woolrich MW, Jbabdi S, Patenaude B, Chappell M, Makni S, Behrens T, Beckmann C, Jenkinson M, Smith SM (2009) Bayesian analysis of neuroimaging data in FSL. Neuroimage 45:S173-186.

Worsley KJ, Evans AC, Marrett S, Neelin P (1992) A three-dimensional statistical analysis for CBF activation studies in human brain. J Cereb Blood Flow Metab 12:900-918.

Zalesky A, Cocchi L, Fornito A, Murray M, Bullmore E (2012) Connectivity differences in brain networks. In: NeuroImage.

Zalesky A, Fornito A, Cocchi L, Gollo LL, Breakspear M (2014) Time-resolved resting-state brain networks. Proc Natl Acad Sci U S A 111:10341-10346.

Zalesky A, Fornito A, Seal ML, Cocchi L, Westin CF, Bullmore ET, Egan GF, Pantelis C (2011) Disrupted axonal fiber connectivity in schizophrenia. Biol Psychiatry 69:80-89.

Zhang D, Raichle ME (2010) Disease and the brain's dark energy. Nature reviews Neurology 6:15--28.

Zhang Y, Brady M, Smith S (2001) Segmentation of brain MR images through a hidden Markov random field model and the expectation-maximization algorithm. IEEE transactions on medical imaging 20:45-57.

Zhou Y, Liang M, Jiang T, Tian L, Liu Y, Liu Z, Liu H, Kuang F (2007a) Functional dysconnectivity of the dorsolateral prefrontal cortex in first-episode schizophrenia using resting-state fMRI. Neurosci Lett 417:297-302.

Zhou Y, Liang M, Tian L, Wang K, Hao Y, Liu H, Liu Z, Jiang T (2007b) Functional disintegration in paranoid schizophrenia using resting-state fMRI. Schizophr Res 97:194-205.

Appendicies

Appendix 3.1 | Demographics and clinical data of traumatic brain injury patients. 1 Severity classification based on Malec et al., 2007. J Neurotrauma. Moderate-Severe (Mod/Sev), Mild (Probable). Not Know (NK). Road Traffic Accident (RTA), Glasgow Coma Scale (GCS), Post-traumatic amnesia (PTA), days (d), hours (h), mintues (m). Structural findings on MR imaging: contusions/gliotic change (Cont), temporo-parietal (TP), frontal (F), occipital (O), fronto-parietal (FP), superficial siderosis (SS), right (R), left (L), bilateral (B), microbleed on gradient echo imaging (MB). Medications highlighted in Italics are potentially psychoactive.

Age	Sex	Severity[1]	Cause	Lowest GCS	PTA	Medication at time of scanning	Structural MRI Findings		
							Brief Remarks	Cont	MB
18	M	Mod/ Sev	Fall	NK	7 d	*Carbamazepine* Lorazepam	B F Cont	Y	Y
24	F	Mod/ Sev	Uncert ain	NK	NK		R FT and O Cont	Y	Y
31	M	Mod/ Sev	RTA	14	8 h	Theophyline Seretide	L F, P and T Cont	Y	Y
34	M	Mod/ Sev	Assault	14	> 6 w		L FT Cont and SS	Y	Y
34	M	Mod/ Sev	Fall	4	52 d		B FT Cont	Y	Y
36	M	Mod/ Sev	Fall	NK	8 h	*Keppra* *Phenytoin*	B FT Cont	Y	Y
44	F	Mod/ Sev	RTA	5	6 w		CC Cont	Y	Y
46	M	Mod/ Sev	NK	3	>24h h		FT Cont and SS	Y	Y
48	F	Mod/ Sev	Fall	9	> 2 w	Thiamine Vitamin B Salbutamol inhaler Steroid inhaler *Amitriptyline* Triptan	R F Cont and SS.	Y	Y
52	F	Mod/ Sev	Fall	NK	36 h	Methotrexate Thyroxine Etanercept injections	B F Cont and SS	Y	Y
54	M	Mod/ Sev	RTA	3	< 24 h	Salbutamol inhaler	R T Cont	Y	Y
20	M	Mod/ Sev	RTA	NK	2-3 w	*Gabapentin*, *Amitriptyline*, Omeprazole, Etoricoxib			Y
22	M	Mod/ Sev	Sports Injury	NK	30 m				Y
23	M	Mod/ Sev	Assault	14	4-5 h				Y
23	M	Mod/ Sev	RTA	6	1 m	*Codeine* Zopiclone Omeprazole,			Y
34	M	Mod/ Sev	RTA	NK	10 - 11 d		DAI		Y

35	F	Mod/ Sev	RTA	NK	> 2 w				Y
35	F	Mod/ Sev	RTA	6	1 m		SS		Y
36	M	Mod/ Sev	RTA	6	1 m				Y
40	M	Mod/ Sev	NK	4	3 m		R T, O, L F and TP gliotic changes		Y
42	M	Mod/ Sev	Fall	9	> 24 h		SS		Y
43	M	Mod/ Sev	RTA	NK	NK	*Tramadol* Nortriptyline Fluoxetine Simvastatin	DAI		Y
48	M	Mod/ Sev	Assault	NK	1 m				Y
53	M	Mod/ Sev	Fall	3	NK	BP Medication	SS		Y
59	M	Mod/ Sev	RTA	NK	< 12 h	Atorvastatin *Lamotrigine*			Y
17	M	Mod/ Sev	Fall	6	3 w	Salbutamol inhaler	R FT Cont. SS	Y	
19	M	Mod/ Sev	Assault	NK	NK	*Citalopram* Simvastatin	B F Cont	Y	
21	M	Mod/ Sev	Assault	15	12 e]d		B F Cont, SS	Y	
23	M	Mod/ Sev	Assault	NK	2 d		B F Cont	Y	
24	M	Mod/ Sev	Assault	NK		*Tramadol*	B F Cont, R T Cont	Y	
25	M	Mod/ Sev	Syncop e	15	30 m		B F Cont	Y	
26	F	Mod/ Sev	RTA	14	6 h		R F Cont	Y	
28	M	Mod/ Sev	RTA	NK	48 h		L F and B T Cont	Y	
29	M	Mod/ Sev	RTA	3	6 w		B F Cont	Y	
30	M	Mod/ Sev	RTA	15		Omeprazole *Citalopram* Sildenafil	B F Cont	Y	
32	M	Mod/ Sev	Assault	NK	< 24 h		B F Cont and R T Cont	Y	
33	M	Mod/ Sev	Assault	NK	12 h	Ciprofloxacin	L T and R F Cont	Y	
33	F	Mod/ Sev	RTA	15	< 5 min	Thyroxine Balsalazide	R T Cont	Y	
33	M	Mod/ Sev	Assault	14	< 12 h		L FT Cont	Y	
35	M	Mod/ Sev	NK	NK	3-4 w	Glargine Humalog	B F Cont	Y	
37	F	Mod/ Sev	RTA	NK	> 2 w			Y	
44	M	Mod/ Sev	Assault	NK	4 d		B F and L T Cont	Y	
48	M	Mod/ Sev	Assault	NK	>1 d		B FT Cont	Y	

48	M	Mod/ Sev	RTA	4	6 w	Ramipril Amlodipine	R FT Cont and SS	Y	
60	F	Mod/ Sev	RTA	NK	11 w			Y	
16	M	Mod/ Sev	Fall	15	NK				
20	M	Mod/ Sev	Sports Injury	15	72 h	*Tramadol* Diclofenac			
21	F	Mod/ Sev	RTA	15	8 h	*Tramadol*	SS		
21	M	Mod/ Sev	Sports Injury	NK	30-60 m				
22	M	Mod/ Sev	Assault	15	3-4 d	Salbutamol Pentesa			
24	M	Mod/ Sev	Assault	13	NK				
28	F	Mild	Fall	NK					
28	M	Mod/ Sev	Assault	4	NK		SS		
28	M	Mod/ Sev	RTA	NK	> 72 h				
31	F	Mod/ Sev	Fall	NK	NK		SS		
33	M	Mod/ Sev	RTA	NK	90 m				
35	F	Mod/ Sev	RTA	12	8 - 10 w	*Cocodamol*			
35	F	Mod/ Sev	RTA	NK	< 24 h	Thyroxine			
35	F		Fall	15					
38	M	Mod/ Sev	Assault	NK	2 h				
38	M	Mod/ Sev	RTA	NK	NK				
44	M	Mod/ Sev	Assault	8	1 m				
45	F	Mod/ Sev	RTA	NK	< 5 m				
46	F	Mild	Accide nt	15		Paracetamol			
46	M	Mod/ Sev	RTA	15	< 1 h				
46	M	Mod/ Sev	Assault	NK	NK		SS		
49	M	Mod/ Sev	Fall	NK	48 h	Amlodipine Simvastatin			
50	M	Mod/ Sev	Fall	15					
53	F	Mild	Sports injury	15					
59	M	Mod/ Sev	Accide nt	NK	2-3 m	Mometasone Simvastatin			

Appendix 3.2 | Detecting the presence of TAI following traumatic brain injury. Classifiers were trained to separate contusion free MB+ve Patients and age matched controls using measures of Fractional anisotropy (FA), mode anisotropy (MO), mean diffusivity (DM) and radial diffusivity (DRAD). 14 contusion free MB+ve Patients (12 males, mean age ± SD: 36.6 ± 11.9 years) and 14 age-matched controls. Significance of classifiers is determined by permutation testing.

N=28	**Performance**	**Sensitivity**	**Specificity**	**P**
FA	89.9%	86.7%	92.3%	<0.002
MO	85.7%	85.7%	85.7%	<0.002
D^{M}	78.1%	75.0%	83.3%	<0.002
D^{RAD}	82.1%	76.5%	90.9%	<0.002

Appendix 3.3 | Classification of TAI in MB-ve TBI patients. Classifiers trained to separate contusion free MB+ve TBI patients from age-matched controls were applied to contusion free MB-ve patients. The output of this classifier separates the MB-ve group into two groups of likely or unlikely TAI. Fractional anisotropy (FA), mode anisotropy (MO), mean diffusivity (DM) and radial diffusivity (DRAD)

N=26	**Likely TAI**	**Unlikely TAI**	**Unsure**
FA	38.4%	61.5%	0%
MO	57.7%	38.5%	3.8%
D^{M}	65.4%	33.6%	0%
D^{RAD}	53.8%	42.2%	3.8%

Appendix 3.4 | Correlation of TAI patient probability with neuropsychological outcome. The probability of being a patient with TAI is assessed in contusion free MB-ve patients using classifiers trained to separate A) MB+ve patients B) contusion free MB+ve patients from age matched controls using four different diffusion metrics; fractional anisotropy (FA), mode anisotropy (MO), mean diffusivity (DM) and radial diffusivity (DRAD). (Pearson's product-moment correlation coefficient (1-tailed), ** p<0.01 * p<0.05 3SF)

A)

N=26		**FA**	**MO**	**D^M**	**D^{RAD}**
IPS	**r**	**.352***	0. 231	**.372***	**.415***
	p	**0.05**	0.145	**0.04**	**0.024**
EF		0.04	0.267	**.352***	**.377***
		0.429	0.109	**0.06**	**0.038**
AM		0.212	0.188	-0.029	-0.051
		0.166	0.195	0.447	0.409

B)

N=26		**FA**	**MO**	**D^M**	**D^{RAD}**
IPS	**r**	**.391***	0.25	**.468***	**.492****
	p	**0.032**	0.125	**0.012**	**0.009**
EF		0.066	0.264	**.407***	**.464***
		0.383	0.111	**0.027**	**0.013**
AM		0.163	0.144	-0.022	-0.084
		0.228	0.256	0.46	0.351

Appendix 3.5 | Predicting cognitive function following traumatic brain injury using support vector regression. Support vector regression was used to predict information processing speed (IPS), executive function (EF) and associative memory (AM). Fractional anisotropy (FA), mode anisotropy (MO), mean diffusivity (DM) and radial diffusivity (DRAD) (Pearson's product-moment correlation coefficient (1-tailed), * p<0.01 3SF, ** p<0.001 3SF)

Test n=65	**Diffusion Estimate**	**r**	**p**
IPS - Median CRT Response time	**FA**	0.391**	<0.001
	MO	0.457**	<0.001
	D^{MEAN}	0.530*	<0.01
	D^{RAD}	0. 528**	<0.001
EF - Trail making B	**FA**	0.407*	<0.01
	MO	0.538**	<0.001
	D^{MEAN}	0.447**	<0.001
	D^{RAD}	0.478**	<0.001

Appendix 5.1 | List of network nodes and corresponding Talairach centroids for each region. Nodes comprising the FPCN/DAN are highlighted in purple. Nodes comprising DMN are highlighted in green. * Talairach Coordinates [x, y, z].

Label		Brain region	Centroid*	
Right	Left		Left	Right
1	66	Enthorinal Cortex	[-24.00, -9.00, -24.33]	[26.00, -7.00, -26.50]
2	65	Parahippocampal gyrus.	[-24.33, -32.50, -11.00]	[27.33, -30.50, -12.33]
3	64	Temporal Pole	[-31.25, 10.75, -30.50]	[32.67, 14.33, -29.67]
4	63	Frontal Pole	[-10.00, 62.50, -6.00]	[9.00, 63.00, -8.00]
5	62	Fusiform Gyrus	[-35.32, -45.50, -13.18]	[36.00, -45.82, -13.55]
6	61	Transverse temporal cortex	[-43.25, -22.25, 10.25]	[43.67, -20.33, 9.67]
7	60	Lateral occipital cortex	[-27.09, -88.14, 4.09]	[29.53, -87.42, 5.16]
8	***59***	***Superior parietal cortex***	***[-22.59, -59.00, 45.41]***	***[24.85, -58.37, 46.04]***
9	58	Inferior temporal cortex	[-49.65, -33.59, -17.59]	[50.53, -28.79, -18.74]
10	***57***	***Inferior parietal cortex***	***[-36.72, -65.68, 29.56]***	***[43.93, -60.43, 29.07]***
11	56	Supramarginal Gyrus	[-50.42, -36.53, 31.68]	[51.88, -31.00, 31.44]
12	55	Bank of the superior temporal sulcus	[-51.00, -44.40, 6.80]	[50.71, -38.43, 5.14]
13	54	Middle temporal cortex	[-50.47, -30.32, -5.79]	[56.65, -23.90, -10.60]
14	53	Superior temporal cortex	[-52.83, -15.62, -1.17]	[53.32, -11.18, -2.79]
15	52	Postcentral Gyrus	[-40.93, -22.73, 44.83]	[43.87, -20.39, 43.03]
16	51	Precentral Gyrus	[-38.00, -9.14, 41.19]	[38.67, -7.97, 41.22]
17	50	Caudal middle frontal cortex	[-34.38, 14.23, 40.69]	[35.31, 13.15, 41.92]
18	***49***	***Pars opercularis***	***[-44.36, 15.91, 14.00]***	***[45.60, 16.10, 13.70]***
19	48	Pars triangularis	[-42.57, 32.43, 2.86]	[44.50, 31.88, 4.00]
20	47	Rostral middle frontal gyrus	[-34.05, 40.42, 16.95]	[33.77, 42.50, 15.77]
21	46	Pars orbitalis	[-40.33, 43.67, -8.67]	[39.83, 44.17, -8.50]
22	45	Lateral orbitofrontal gyrus	[-22.50, 33.70, -10.80]	[22.37, 32.26, -13.00]
23	44	Caudal anterior cingulate cortex	[-7.25, 17.50, 29.50]	[6.50, 21.25, 27.50]
24	***43***	***Rostral anterior cingulate cortex***	***[-6.75, 37.50, 2.00]***	***[7.75, 35.75, 3.00]***
25	***42***	***Superior frontal gyrus***	***[-13.26, 28.88, 37.76]***	***[13.78, 30.02, 38.41]***
26	41	Medial orbitofrontal gyrus	[-7.58, 37.50, -13.33]	[7.25, 38.25, -12.50]
27	40	Lingual Gyrus	[-14.44, -65.56, 0.06]	[16.00, -65.47, -0.24]
28	39	Pericalcarine Cortex	[-11.11, -78.89, 10.56]	[13.90, -77.50, 10.10]
29	38	Cuneus	[-7.13, -80.38, 22.50]	[10.40, -78.80, 22.10]
30	37	Paracentral lobule	[-8.36, -28.36, 54.64]	[10.50, -26.83, 53.50]
31	***36***	***Isthmus of the cingulate cortex***	***[-8.63, -44.63, 23.00]***	***[11.00, -43.75, 22.50]***
32	35	Precuneus	[-10.22, -52.48, 37.65]	[13.39, -56.04, 36.30]
33	34	Posterior Cingulate cortex	[-6.71, -16.29, 36.71]	[8.71, -14.57, 36.57]